

EXPERIMENTAL CHARACTERIZATION AND
VISCOELASTIC FINITE ELEMENT MODELING OF A
PORCINE THORACIC SPINAL CORD SUBMITTED TO
AXIAL COMPRESSION

by

Atefeh MASOUMIPOUR

THESIS PRESENTED TO ÉCOLE DE TECHNOLOGIE SUPÉRIEURE
IN PARTIAL FULFILLMENT FOR A MASTER'S DEGREE
WITH THESIS IN MECHANICAL ENGINEERING
M.A.SC.

MONTREAL, APRIL 22, 2021

ÉCOLE DE TECHNOLOGIE SUPÉRIEURE
UNIVERSITÉ DU QUÉBEC



Atefeh Masoumipour, 2021



This Creative Commons license allows readers to download this work and share it with others as long as the author is credited. The content of this work can't be modified in any way or used commercially.

THIS THESIS HAS BEEN EVALUATED
BY THE FOLLOWING BOARD OF EXAMINERS

Mr. Eric Wagnac, Thesis Supervisor
Department of Mechanical Engineering, École de technologie supérieure

Mr. Yvan Petit, Thesis Co-supervisor
Department of Mechanical Engineering, École de technologie supérieure

Mrs. Sophie Lerouge, President of the Board of Examiners
Department of Mechanical Engineering, École de technologie supérieure

Mrs. Morgane Evin, Member of the jury
Researcher, Aix-Marseille Université, France

THIS THESIS WAS PRESENTED AND DEFENDED
IN THE PRESENCE OF A BOARD OF EXAMINERS AND PUBLIC
ON APRIL 15, 2021
AT ÉCOLE DE TECHNOLOGIE SUPÉRIEURE

DEDICATION

*To my lovely parents, wonderful brother and beloved spouse Soroush,
who light up the way of my life.*

ACKNOWLEDGMENT

I wish to express my sincere gratitude to my research supervisor, Professor Eric Wagnac, and my co-supervisor, Professor Yvan Petit, for providing me the opportunity to work at the research center at Sacré-Coeur hospital of Montreal, and providing invaluable support and guidance throughout the research.

Sincere thanks to my colleagues at Sacré-Coeur hospital of Montreal, who help me to be integrated with the new environment. Very special thanks to Elisabeth Laroche and Lucien Diotalevi. I am fortunate having your suggestions and feedbacks on my research. Thank you for training me with experimental tools and equipment of the laboratory and assisting me during my study.

I would like to thank Professor Sophie Lerouge for providing me the opportunity to perform the experiments at the CHUM research center. I must also acknowledge Boris Chayer for assisting me with the experimental equipment at the CHUM research center.

Finally, I would like to express my thanks and dedicate this work to my patient and supportive parents for their encouragement, my brother for his wise counsel and my beloved spouse for his endless love and support that made this endeavor possible.

I would never have walked this journey without you.

CARACTÉRISATION EXPÉRIMENTALE ET MODÉLISATION PAR ÉLÉMENTS FINIS VISCOÉLASTIQUES D'UN MOELLE ÉPINIÈRE THORACIQUE PORCINE EN COMPRESSION AXIALE

Atefeh MASOUMIPOUR

RÉSUMÉ

La compression axiale est un des modes de chargement supporté quotidiennement par la moelle épinière. Appliquée dans la direction transverse, la compression résulte fréquemment en des lésions de la moelle épinière. Afin de faire progresser notre compréhension du comportement physiologique et traumatique de la moelle épinière en compression, il est crucial de caractériser le comportement mécanique des composants de la moelle épinière. De récentes études ont montré l'importance d'identifier séparément le comportement de la matière blanche et de la matière grise composant la moelle épinière. D'autres études ont montré l'importance de déterminer la réponse viscoélastique en relaxation de contraintes de ces tissus et d'améliorer le comportement des modèles par éléments finis de la moelle épinière via l'intégration de propriétés viscoélastiques. À ce jour, ces travaux n'ont pas encore été complétés. L'objectif principal de cette étude est donc de caractériser le comportement mécanique des matières blanche et grise de la moelle épinière en compression axiale non confinée incluant une phase de relaxation de contraintes.

Deux segments de moelle épinière ont été prélevés dans la région thoracique de deux porcs immédiatement après leur sacrifice. Les segments de moelle épinière ont été coupés en échantillons de 2,25 mm d'épaisseur. Ces échantillons ont individuellement été déposés dans une boîte de Pétri, enveloppés dans une gaze vaporisée avec une solution du tampon phosphate salin pour éviter leur déshydratation puis testés en compression axiale non confinée sur une machine de test. Ce protocole a été complété en moins de six heures afin de réduire l'influence du temps post-mortem sur les propriétés mécaniques des tissus de la moelle épinière. Tous les échantillons ont été comprimés jusqu'à 40% de déformation, à un taux de déformation de $0,01 \text{ s}^{-1}$. La compression quasi-statique a ensuite été maintenue pendant 1000 secondes afin de laisser la moelle épinière relaxer.

Un modèle par éléments finis (MEF) d'un échantillon typique a été créé puis utilisé pour obtenir, via une méthode inverse, les propriétés matérielles hyper-viscoélastique de la matière grise, tout en utilisant les propriétés de la matière blanche issue de la littérature. Un modèle hyperélastique d'Ogden du premier ordre accompagné d'une série de prony à 3 termes a permis de reproduire avec précision la réponse en compression de la moelle épinière et son comportement viscoélastique en relaxation de contraintes. Il a été constaté que la matière grise est environ 3,2 fois plus rigide que la matière blanche. Pour le temps de relaxation, il a été déterminé que le tissu de la moelle épinière se relaxe complètement après environ 931 secondes suite à une compression axiale.

Ces résultats soulignent l'importance de distinguer le type de tissu lors de l'utilisation de modèles numériques afin d'améliorer notre compréhension de la biomécanique de la moelle épinière.

Mots clés : compression axiale, matière blanche, matière grise, moelle épinière, modèle par éléments finis, hyperélasticité, viscoélasticité, relaxation de contraintes.

**EXPERIMENTAL CHARACTERIZATION AND VISCOELASTIC FINITE
ELEMENT MODELING OF A PORCINE THORACIC SPINAL CORD
SUBMITTED TO AXIAL COMPRESSION**

Atefeh MASOUMIPOUR

ABSTRACT

Axial compression is one of the main loading sustains daily by the spinal cord, while transverse compression loads, much less frequent, often results in spinal cord injury. To increase our understanding of the spinal cord biomechanics under normal and traumatic conditions, measuring the behavior of the spinal cord components material properties is of utmost importance. Recent studies expressed the importance of identifying the behavior and material properties of the spinal cord white and grey matter separately. In addition, recent studies stated the importance to determine the relaxation response of the spinal cord tissues and to improve the behavior of spinal cord finite element models by using derived viscoelastic properties. This work has not been completely achieved yet. The main objective of this study is to characterize and simulate numerically the mechanical behavior of the spinal cord white and grey matter tissue under unconfined axial compression including a stress relaxation phase.

Two spinal cord were harvested from the thoracic region of two pigs immediately following sacrifice. Each spinal cord was cut in four samples of 2.25 mm thick, for a total of eight samples. Samples were placed in a petri-dish, wrapped in a sprayed gauze with Phosphate-Buffer saline to avoid dehydration and tested under unconfined axial compression using a mechanical testing device. The throughout process was completed in less than six hours to reduce the influence of time post-mortem on the mechanical properties of the spinal cord tissue. All specimens were compressed up to 40% strain at a strain rate of 0.01/sec, and was then allowed to relax for 1000 seconds.

A finite element model (FEM) of a typical sample was created and used to derive, using an inverse method, the hyper-viscoelastic material properties of the grey matter, with white matter material properties derived from literature. A first order Ogden hyperelastic model coupled with a 3-term prony series best captured the compressive response of the spinal cord and its viscoelastic behavior during stress-relaxation. It has been found that grey matter is about 3.2 times stiffer than the white matter. For relaxation time, it has been determined that the spinal cord tissue completely relax after approximately 931 seconds following axial compression.

These results highlight the importance of distinguishing the type of tissue when using computational models to deepen our understanding of the biomechanics of the spinal cord.

Keywords: Axial compression, grey matter, white matter, spinal cord, finite element model, hyperelasticity, viscoelasticity, stress relaxation

TABLE OF CONTENTS

	Page
CHAPTER 1 LITERATURE REVIEW	3
1.1 Anatomy of Human Spine and Spinal Cord.....	3
1.1.1 The spinal Column.....	3
1.1.1.1 Vertebrae.....	4
1.1.1.2 Intervertebral Discs.....	5
1.1.1.3 Ligaments.....	6
1.1.2 Spinal Cord	7
1.1.2.1 Spinal Cord White and Grey Matter	10
1.2 Overview of Spinal Cord Injury.....	14
1.2.1 Pathology of Spinal Cord Injury	14
1.2.2 Epidemiology and Demographics.....	15
1.2.3 Spinal Cord Injury Diagnostic	17
1.3 Experimental Modeling of Spinal Cord Injury.....	18
1.3.1 Animal models.....	18
1.3.2 Spinal Cord Injury Mechanism.....	19
1.3.3 Effect of Depth, Velocity and Duration.....	22
1.4 Finite Element Modeling of the Spinal Cord	23
1.4.1 Finite Element Modeling	23
1.4.2 Constitutive Models.....	23
1.4.3 Finite Element Models of the Spinal Cord	27
1.5 Mechanical Properties of Spinal Cord.....	30
1.5.1 Loading Type.....	31
1.5.2 Mechanical properties of intact spinal cord.....	32
1.5.3 Mechanical Properties of the Spinal Cord White and Grey Matter	35
CHAPTER 2 PROBLEMS AND OBJECTIVES	39
2.1 Problems.....	39
2.2 Objectives.....	40
2.3 Methodological approach	41
CHAPTER 3 METHODOLOGY	43
3.1 Experimental Characterization of the Loading and Stress Relaxation Behavior of Porcine Spinal Cord under Unconfined Axial Compression.....	43
3.1.1 Spinal Cord Preparation.....	44
3.1.2 Spinal cord area.....	45
3.1.3 Unconfined Axial Compression Tests	46
3.1.3.1 Testing device	47
3.1.3.2 Preconditioning.....	48
3.1.4 Unconfined compression test.....	49
3.1.5 Data analysis	49
3.1.6 Finding relaxation time	50

3.2	Finite element model of the spinal cord	53
3.2.1	Spinal cord geometry	53
3.2.2	Meshing of the FEM	54
3.2.3	Interface, loading and boundary conditions.....	56
3.2.4	Material properties	57
3.2.4.1	White matter material properties	59
3.2.4.2	Grey matter material properties	62
CHAPTER 4 RESULTS		65
4.1	Experimental characterization of the loading and stress relaxation behavior of the porcine spinal cord under unconfined axial compression	65
4.2	Mesh Convergence Analysis	68
4.3	Verification of the white matter material properties	71
4.4	Calibration of the grey matter material properties	72
CHAPTER 5 DISCUSSION.....		75
5.1	Stress-relaxation behavior of the spinal cord under unconfined axial compression ..	75
5.2	Finite element modeling of the spinal cord	79
5.3	Limitations.....	80
CONCLUSION		83
BIBLIOGRAPHY.....		85

LIST OF TABLES

	Page
Table 1.1	Combinations of material properties for the spinal cord grey and white matter in finite element simulations used by (Jannesar et al., 2016)28
Table 1.2	Different material properties for the spinal cord grey and white matter in finite element simulations30
Table 1.3	Summary of main experimental parameters that have been used in the literature to investigate mechanical properties of the spinal cord in tensile testing. The empty cells display that the author did not provide the information.....33
Table 1.4	Summary of main experimental parameters that have been used in the literature to investigate mechanical properties of the spinal cord white and grey matter. The empty cells display that the author did not provide the information.....36
Table 3.1	Antero-posterior and lateral axis of the cross-section of porcine spinal cord samples.....46
Table 3.2	Generalized Maxwell parameters and the correlated constants in MATLAB52
Table 3.3	Description of the five meshes compared in the convergence study55
Table 3.4	Material models and selected parameters for the complete spinal cord from the curve fitting process59
Table 3.5	White matter material models and parameters from the curve fitting process61
Table 4.1	Long-term relaxation time (parameter λ_2) obtained by curve fitting a two-terms generalized Maxwell model to the stress-time relaxation curves of each specimen67
Table 4.2	Total simulation time and peak stress values for the 5 different mesh size..70
Table 4.3	Peak and equilibrium stress in the white matter for the FE simulation and the experimental results, and R-square values between their stress-time curves71
Table 4.4	Peak stress of the FEM, and the percentage of differences in peak stress level between the experiment on sample POR06-S02 and 5 of the 13 simulations, as well as the (R2) value.73

Table 4.5	White and grey matter material models and parameters from the curve fitting process.....	74
-----------	--	----

LIST OF FIGURES

		Page
Figure 1.1	The different regions and natural curvature of the spinal column ("Anatomy of the Spine," 2018)	4
Figure 1.2	General bony structure of a typical vertebra ("Spine Anatomy," n.d.).....	5
Figure 1.3	The intervertebral disc schematic representations. (A) Mid-sagittal cross-section and (B) 3D view displaying annulus fibrosus lamellar structure. (Smith et al., 2011).....	6
Figure 1.4	Seven spinal column ligaments ("Spinal Anatomy," n.d.).....	7
Figure 1.5	Spinal cord and its start and endpoint ("Spinal Cord," n.d.).....	8
Figure 1.6	Dermatome pattern, Sensory Innervation of Spinal Nerves. ("Dermatomes and Myotomes: Upper & Lower Limb," n.d.).....	9
Figure 1.7	Spinal Cord three layers (pia matter, arachnoid matter and dura matter), which are known as the meninges, and anterior and posterior spinal arteries ("Spinal Menings," n.d.).....	10
Figure 1.8	The cross-section of a thoracic spinal cord segment demonstrates the white matter anterior, posterior, and lateral columns, as well as the grey matter anterior, posterior, and lateral horns ("The Central Nervous System," n.d.).....	11
Figure 1.9	Human Neuron Anatomy. The direction of electrical impulses traveling is from the left side to the right side. (Biga et al., n.d.)	12
Figure 1.10	Human Spinal Cord Tracts ("Spinal Cord," n.d.)	14
Figure 1.11	Summary of secondary injury processes following TSCI	15
Figure 1.12	Etiology of Adult Spinal Cord Injury (Sekhon & Fehlings, 2001).....	16
Figure 1.13	Level of Injury in Adult Spinal Cord Injury (Sekhon & Fehlings, 2001)....	17
Figure 1.14	Magnetic resonance imaging (MRI) of a Sprague–Dawley rat (a), Yucatan miniature porcine (b), and human (c) at T10 level. A prominent layer of cerebrospinal fluid (CSF) surrounds the porcine spinal cord, as well as the human's one. The porcine spinal cord width is close to the human spinal cord. (Lee et al., 2013).....	19

Figure 1.15	Schematic diagrams of a normal spinal cord and three spinal cord injury mechanisms (Chen et al., 2015).....	21
Figure 1.16	Maximum Principal Strain MPS distribution at non-human primate contusion impact in spinal cord white and grey matter at the injury epicenter. The Columns (A-D) stand for (A) model A, (B) model B, (C) model C, and (D) model D (Jannesar et al., 2016)	29
Figure 1.17	Stress-strain data of several studies on spinal cord mechanical properties in tensile testing	32
Figure 2.1	Methodological approach.....	42
Figure 3.1	Spinal cord preparation. a) 15mm thoracic segment of a porcine spinal cord b) 2.25 mm thick spinal cord sample c) Spinal cord sample wrapped in a sprayed gauze with phosphate buffer saline.....	45
Figure 3.2	Mechanical tester model Mach-1 V500CST.....	47
Figure 3.3	Detection of the contact between the cylinder impactor and the sample, at a force of 0.025 N	48
Figure 3.4	Schematic diagrams and mathematical definition of three rheological models. a) Maxwell model b) Generalized Maxwell Model c) Linear Standard Kelvin Model.....	50
Figure 3.5	Stress-time diagram of a preliminary test with MATLAB curve-fitting tool in three rheological models. a) Maxwell model, $R^2 = 0.878$ b) Generalized Maxwell Model, $R^2 = 0.991$ c) Linear Standard Kelvin Model, $R^2 = 0.550$	51
Figure 3.6	Geometry of the sample POR06-S02 in the CATIA software with 6.646 mm lateral axis, 6.266 mm antero-posterior axis, and 2.25mm thickness....	53
Figure 3.7	FEM interface, loading and boundary conditions.....	56
Figure 3.8	Curve fitting of both loading (a) and stress relaxation (b) behavior averaged from eight spinal cord samples under compression. Experimental data are displayed by solid line and fitted model by dash-lines.	58
Figure 3.9	Curve fitting of both loading and stress relaxation curves of the white matter measured under compression by Keaveny and Sparrey (2011). Experimental data are displayed by solid line and fitted model by dash-lines.	60

Figure 3.10	FEM of a circular cylinder of white matter used to mimic the experiment of Sparray and Keaveny (2011)61
Figure 4.1	Typical force-time response of all samples under unconfined axial compression65
Figure 4.2	Stress-strain response for porcine spinal cord specimens up to a strain of 0.466
Figure 4.3	Results of the relaxation response of all samples67
Figure 4.4	Average stress-time curve of all samples for the relaxation phase, as well as the average curve plus/minus one standard deviation, the experimental corridor and the curve for sample P06-S0268
Figure 4.5	Calculation time for the different meshes69
Figure 4.6	Loading and stress relaxation responses for different mesh sizes70
Figure 4.7	Experimental vs FE simulation stress-time data fit of the spinal cord white matter71
Figure 4.8	Loading and stress relaxation response of the complete spinal cord from five simulations with different multiplication factor for the gray matter properties, and the experimental results of the sample POR06-S02.....72

LIST OF ABBREVIATIONS

FEM	Finite element model
SCI	Spinal cord injury
TSCI	Traumatic spinal cord injury
IVD	Intervertebral disc
NP	Nucleus pulposus
AF	Annulus fibrosus
PNS	Peripheral nervous system
CSF	Cerebrospinal fluid
CNS	Central nervous system
CT	Computed tomography
MRI	Magnetic resonance imaging
QLV	Quasi-linear viscoelastic
FEM	Finite element model
NHP	Nonhuman primate
WM	White matter
GM	Grey matter
MPS	Maximum principal strain
AVE	Average
SD	Standard deviation
MIN	Minimum
MAX	Maximum
PBS	Phosphate buffered saline

LIST OF SYMBOLS

E	Elastic modulus
K	Bulk modulus
V	Poisson ratio
P	Pressure
τ_i	Relaxation time
Ha	Aggregate modulus
F	Force
A	Surface area
t	Time
σ	Stress
ε	Strain
ε°	Strain rate
V_0	Initial volume of substance
V_n	Diminished volume of material resulting from the applied pressure
G(t)	Relaxation tensor
$\sigma^e (\epsilon)$	Stress to an instantaneous strain within a uniaxial loading period
g_i	Relative moduli
m	Meter
mm	Millimeter
cm	Centimeter
m ²	Meter square
mm ²	Millimeter square
Pa	Pascal
MPa	Megapascal
KPa	Kilopascal
N	Newton
min	Minute
s	Second
mm/s	Millimeter per second

INTRODUCTION

Spinal cord injury (SCI) is a catastrophic incident that imposes a major burden on patients, their families and society. Damage to the spinal cord leads to neurological dysfunction that affects motor, sensory and autonomic control. Traumatic Spinal Cord Injury (TSCI) prevalence is estimated to range from 10 to 83 individuals per million worldwide (Blumer and Quine, 1995, Berg et al., 2010, Wyndaele, 2006). TSCI is due to adverse causes such as an accident in a motor vehicle, fall or sport-related injuries. SCI incidence and prevalence knowledge is important for the implementation of prevention-based approaches and health care planning (Noonan et al., 2012).

With a high number of human treatment trials, the field of spinal cord injury is of special importance. Unfortunately, no one has yet provided substantial improvement in neurological recovery or a significant increase in function, even though a lot of effort and resources have been invested. While SCI clinical trials have previously been reviewed, there is a need for a critical and systemic analysis of the methods of past and current studies to assess the shortcomings. In terms of population suffering injury, the causes of injury, and the degree and severity, human SCI is rather heterogeneous. On the other hand, this heterogeneity is disregarded with several SCI clinical trials and represent only a single injury models. Nevertheless, disregard for human SCI heterogeneity could be an important explanation for the inability to find clinically functional therapies (Tator, 2006).

Today, it is possible to analyze the injury mechanisms leading to SCI using computational models, including the effect of tissue heterogeneity. These models help to equate the spinal cord impact with damage to spinal cord tissue. However, the consistency of these models depends on the behavior of the spinal cord material. The onset, severity and distribution of tissue damage can be affected by subtle differences in mechanical variables associated with injury and intrinsic variations in the biomechanical properties of grey and white matter (Popovich et al., 2010). Awareness of spinal cord grey and white matter tissue properties and tolerances will connect the injury mechanisms with the pattern of tissue damage and eventually

to their neurological shortcomings. This can reduce the gap between pre-clinical studies and human researches (Maikos et al., 2008).

Computational models such as finite element methods are notably employed to increase our understanding of SCI biomechanics. However, their validity strongly depends on the underlying assumptions, which are made during model creation. Homogeneous characteristic is typically assumed for the constitutive model of spinal cord, meaning that the white and grey matter have the same material properties. Nevertheless, recent researches illustrate that heterogenic accounting is necessary to anticipate spinal cord injury. This has contributed to the need to establish the mechanical properties of the spinal cord white and grey matter (Yu, 2019).

Even if compressive loading is one of the main loading sustains daily by the spinal cord, very little experimental data is currently available on the viscoelastic mechanical properties of the spinal cord under compression, mainly due to the challenges in securing, preparing and testing spinal cord tissue samples. Moreover, the viscoelastic behavior of the spinal cord hasn't been implemented into finite element model of the spinal cord, thus limiting their ability to provide insight into its normal, pathophysiological and per/post-trauma behavior. Accordingly, my research attempts to improve knowledge of biomechanics of spinal cord when exposed to axial compression. Specifically, it focuses on measuring the viscoelastic behavior of the spinal cord white and grey matter under unconfined axial compression, and to provide a FEM that accounts for such behavior.

The first chapter of this master thesis presents a brief literature review that covers all the topics required to understand the work accomplished in this study. This chapter will be followed by the problematic and objectives (Chapter 2), the methodology (Chapter 3) used to meet the objectives and its associated results (Chapter 4). A discussion (Chapter 5) will then emphasizes the findings of this study and its limitations, followed by a conclusion.

CHAPTER 1

LITERATURE REVIEW

1.1 Anatomy of Human Spine and Spinal Cord

Spine is one of the most important part of the body that gives structure and support, and allows it to move freely and bend with flexibility. The spine is intended to protect the spinal cord, which is a column of nerves that connects the brain to the rest of the body, allowing control of body movements. Spinal cord white and grey matter have distinct characteristics. In order to understand the variations of the spinal cord components and how the model can be developed, the relevant anatomy and physiology of the spinal cord has to be understood.

1.1.1 The spinal Column

The spinal column, which is also known as the spine, the vertebral column or the backbone, protects the spinal cord, provides human body with structural stability, supports nervous system and enables mobility. The spinal column keeps the body straight, enables it to bend and twist easily, and provides a pathway for major nerves flowing from the brain to the toes. The complete spinal column is made up of 24 discrete bony vertebrae, plus 2 natural fused vertebral parts, the sacrum and the coccyx. The spine is divided into 3 distinct regions: the cervical, the thoracic and the lumbar spine. The cervical spine (neck) is composed of 7 vertebrae (C1-C7), the thoracic spine (mid back) has 12 vertebrae (T1-T12) while the lumbar spine (lower back) has 5 vertebrae (L1-L5). A standard vertebrae column produces a double-S curve that has shock-absorbing capacity with inward cervical, outward thoracic, following by an inward lumbar vertebral curve (Figure 1.1). Five sacral fused vertebrae, located between the lumbar spine and the hip bones, shapes the back of the pelvis. The coccyx is composed of 3-5 small bones that naturally bind together immediately below the sacrum. Although the coccyx is a very small bone, it plays a crucial role in supporting the weight of the body while sitting. Since the spinal cord ends before the last lumbar vertebrae, only cervical and thoracic

parts of the vertebral column are important in this study. Consequently, further information about the other spinal regions will not be addressed furthermore. In addition to the bones, spine relies on a variety of supporting structures such as intervertebral discs, facet joints, ligaments and muscles to provide skeletal support and guide the nerves (Highsmith, 2020).

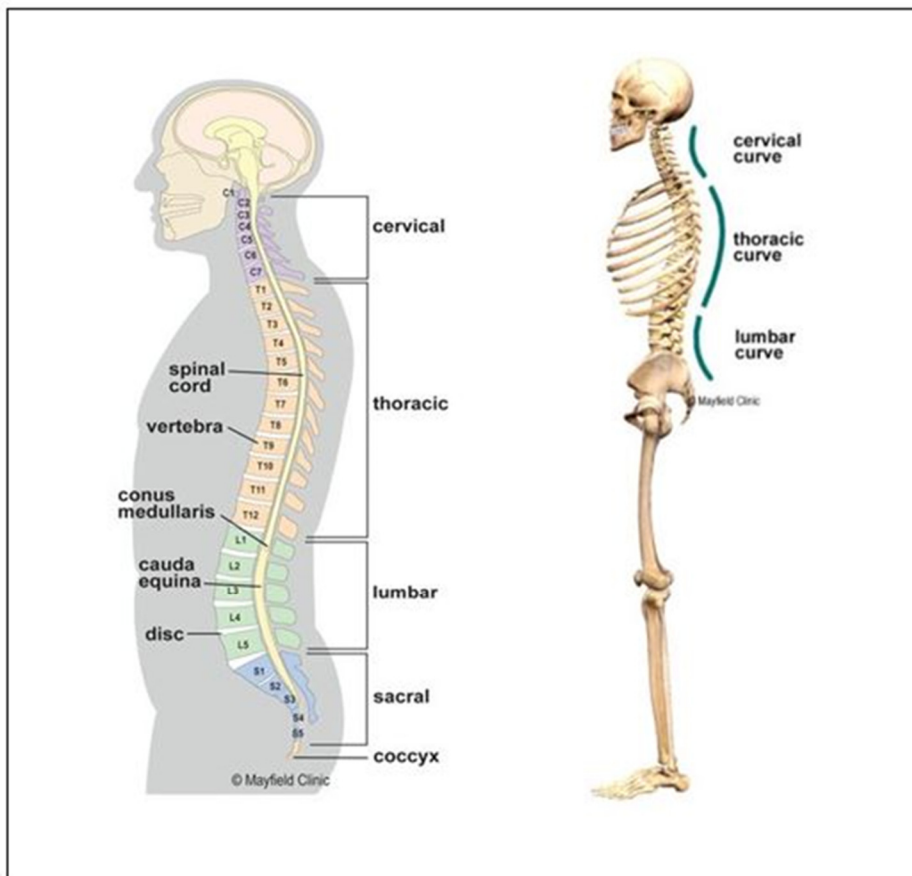


Figure 1.1 The different regions and natural curvature of the spinal column ("Anatomy of the Spine," 2018)

1.1.1.1 Vertebrae

The 24 independent vertebrae that form the spinal column are connected to each other by the intervening intervertebral discs and the spinal ligaments. Each vertebra has two key functional components: 1) the load-bearing vertebral body that forms the anterior part of each vertebra,

and 2) the vertebral arch that forms the lateral and posterior aspect of each vertebrae. Vertebral arch combines with the vertebral body to form an enclosed hole, the vertebral foramen. All the vertebral foramina line up to form the vertebral canal, which contains the spinal cord. There are several bony prominences on the vertebral arch: the spinous process, the transverse processes, the pedicles, the lamina and the articular processes (Figure 1.2), all acting as attachment sites for ligaments and muscles.

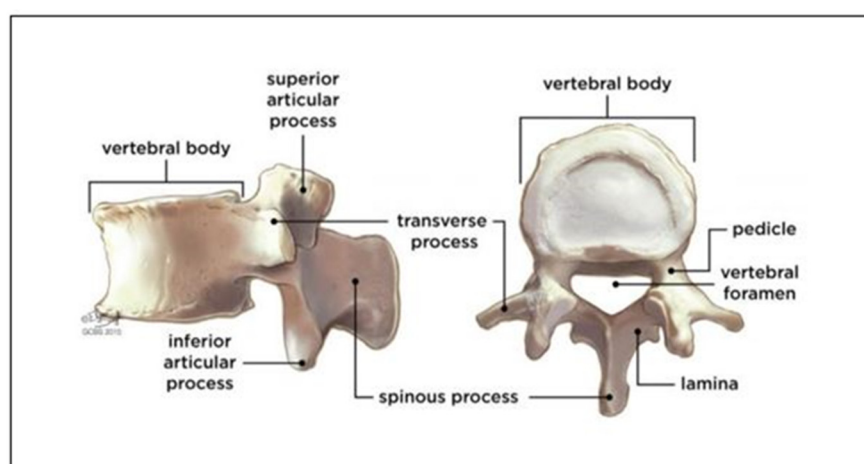


Figure 1.2 General bony structure of a typical vertebra
("Spine Anatomy," n.d.)

1.1.1.2 Intervertebral Discs

Intervertebral discs (IVD) cover a quarter of the length of the spinal column. It is the main joint in the spinal column, making it flexible without losing much strength. Intervertebral discs are fibrocartilaginous cushions that serve as a shock absorption device for the spine. The discs enable flexion, extension, lateral bending and torsion of the vertebral column. Although individual disc motion is very limited, significant movement is possible when many discs combine forces. The IVD is composed of a central nucleus pulposus (NP), a peripheral annulus fibrosus (AF) and two vertebral endplates that attach the discs to adjacent vertebrae (Bridwell, 2019). The NP is a gel-like structure in the middle of the intervertebral disc that is very durable and flexible Waxenbaum et al. (2020). The AF is made up of "lamellae" or concentric collagen

fiber layers. The fiber orientation of every layer of lamellae alternates, thus enabling successful resistance of multi-directional motions (Marchand & Ahmed, 1990). The upper and lower cartilaginous endplates protect the upper and lower portions of the disc and provides the key source of nutrition for the disc (Figure 1.3) ("Applied anatomy of the lumbar spine," n.d.)

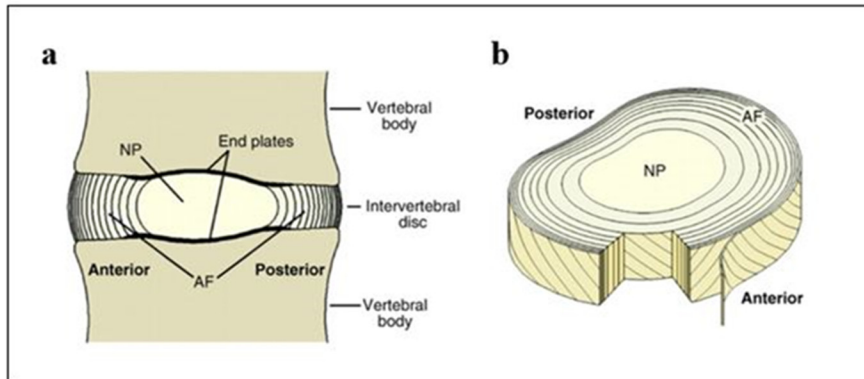


Figure 1.3 The intervertebral disc schematic representations. (A) Mid-sagittal cross-section and (B) 3D view displaying annulus fibrosus lamellar structure.
(Smith et al., 2011)

1.1.1.3 Ligaments

The spinal ligaments are connective tissues holding vertebrae together along the spine to stabilize it and protect the IVDs. Ligaments restrict the movement of the spinal column by avoiding excessive bending motions (Frank, 2004). These functions are performed by seven main ligaments as shown in Figure 1.4.

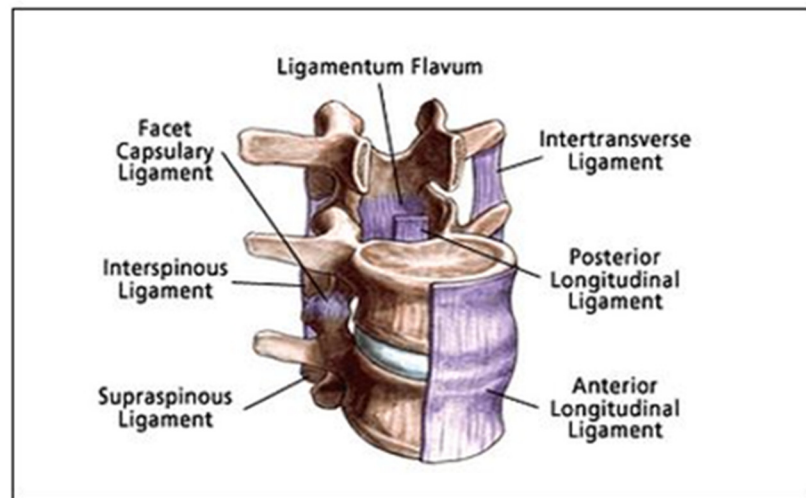


Figure 1.4 Seven spinal column ligaments
("Spinal Anatomy," n.d.)

1.1.2 Spinal Cord

The spinal cord functions as a medium for the information circulating between the brain and the peripheral nervous system (PNS). Together, the spinal cord and the brain forms the central nervous system (CNS). The spinal cord is a long, tubular bundle of nervous tissue that supports cells extending from the brain medulla oblongata to the lumbar region. It starts from the foramen magnum, the opening at the base of the skull, and extends to the gap between the first and second lumbar vertebrae, as shown in Figure 1.5.

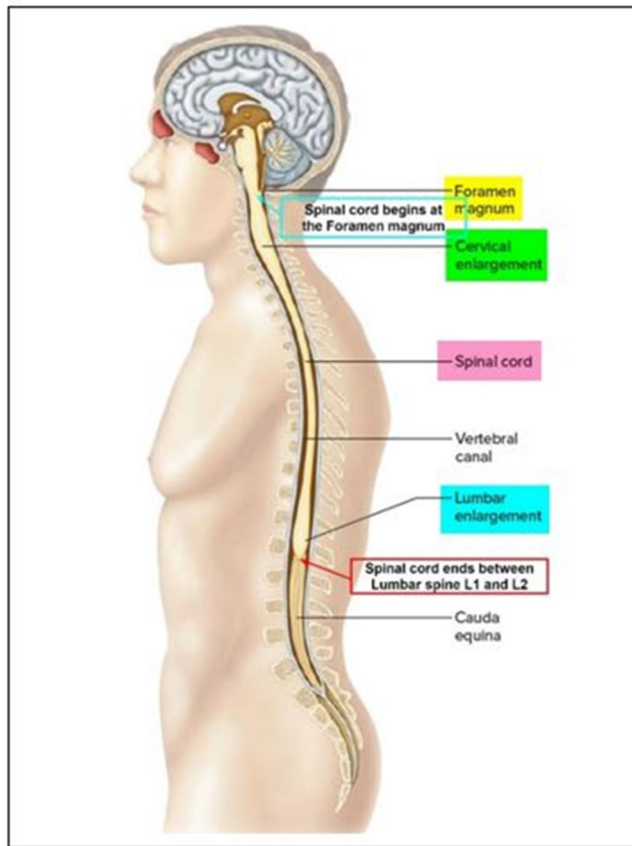


Figure 1.5 Spinal cord and its start and endpoint
("Spinal Cord," n.d.)

The length of the spinal cord ranges from 40 to 50 cm and is different between males and females. The approximate size of the men's spinal cord is 45 cm (18 in) while it is 43 cm (17 in) for women ("Anatomy of the Spinal Cord," n.d.). Spinal cord branches into 31 pairs of spinal nerves, with two consecutive rows of nerve roots appearing in each pair (left & right). The spinal cord is mainly composed of nervous tissues, the white and the grey matter, and divided into four regions: 8 pairs of cervical nerves, 12 pairs of thoracic nerves, 5 pairs of lumbar nerves, 5 pairs of sacral nerves, and 1 pair of coccygeal nerves (Cho, 2015). With the exception of C1, which has no sensory nerve root, each segment has a pair of sensory and motor roots that join to form a spinal nerve. With the exception of C8, each segment corresponds to a vertebra. Spinal nerves in the cervical region exit above their corresponding vertebrae, while starting with T1, they exit below their corresponding nerves (Cho, 2015).

Dorsal nerve fibers transmit sensory information to the brain while motor information is relayed away from the brain by ventral nerve fibers. These fibers contribute to the formation of peripheral nervous system and innervate dermatomes (skin receptors) for body sensation, myotomes (muscle fibers) for motions, and the autonomic nervous system that generates organ function (Figure 1.6) (Yu, 2019).

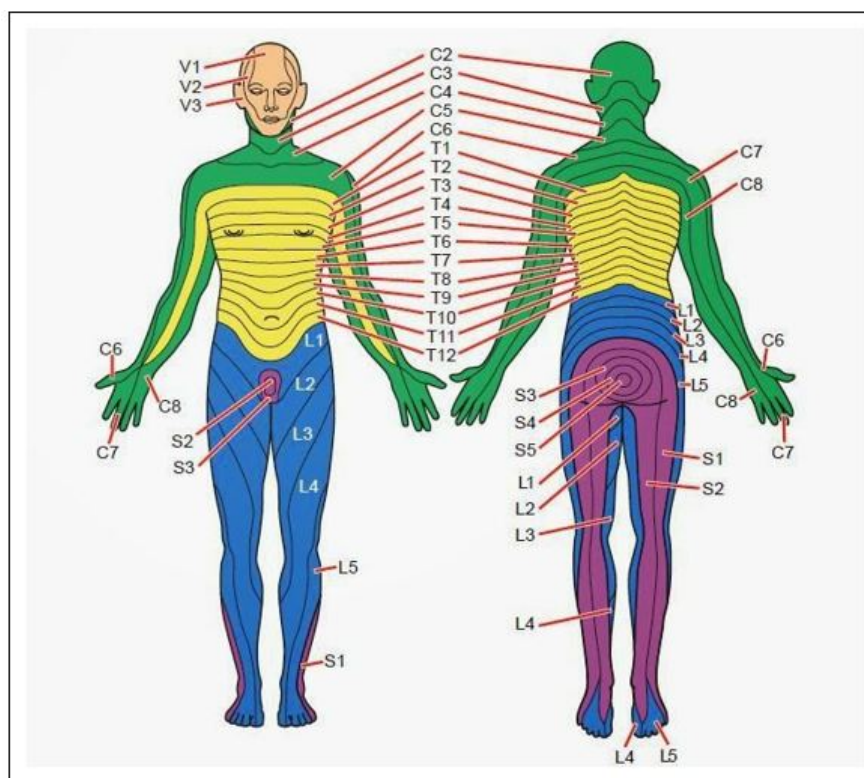


Figure 1.6 Dermatome pattern, Sensory Innervation of Spinal Nerves.
("Dermatomes and Myotomes: Upper & Lower Limb," n.d.)

Spinal cord is covered by three layers of tissue called meninges and split into three regions (Figure 1.7). The outer layer of the spinal cord tissue is the dura mater that forms a durable protective covering. The area between the dura mater and the bone around the vertebral wall is known as the epidural space that contains fat and small blood vessels. The middle layer, which is below the dura mater, is known as arachnoid mater. The pia mater is the deepest protective layer and is closely connected to the surface of the spinal cord. The area between the arachnoid and the pia mater is named the subarachnoid area, and contains the cerebrospinal

fluid (CSF). The spinal cord is connected to the dura mater by means of a series of lateral denticulate ligaments arising from the pial fold (Cho, 2015; "The Spinal Cord," n.d.). The anterior two-thirds of the spinal cord and posterior third are supplied by the anterior and posterior spinal arteries, respectively. They are fed by segmental radicular arteries, which branch off the vertebral arteries in the cervical region (Cho, 2015).

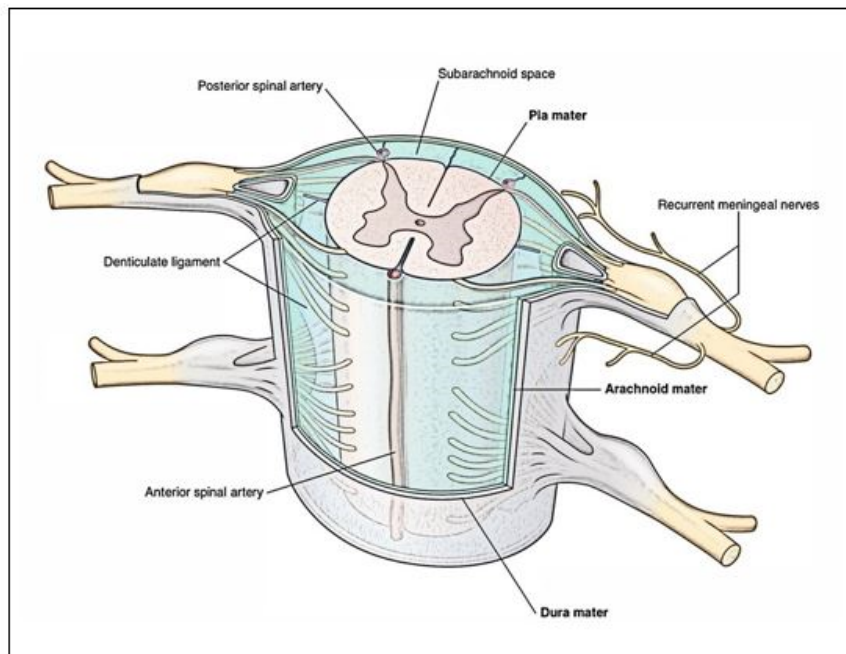


Figure 1.7 Spinal Cord three layers (pia matter, arachnoid matter and dura matter), which are known as the meninges, and anterior and posterior spinal arteries ("Spinal Menings," n.d.)

1.1.2.1 Spinal Cord White and Grey Matter

The cross section of a spinal cord shows the white matter in periphery, the grey matter, that exhibits an H or butterfly shape, and a small canal filled with CSF in its center (Figure 1.8). A single layer of cells known as the ependymal layer is surrounding the grey matter.

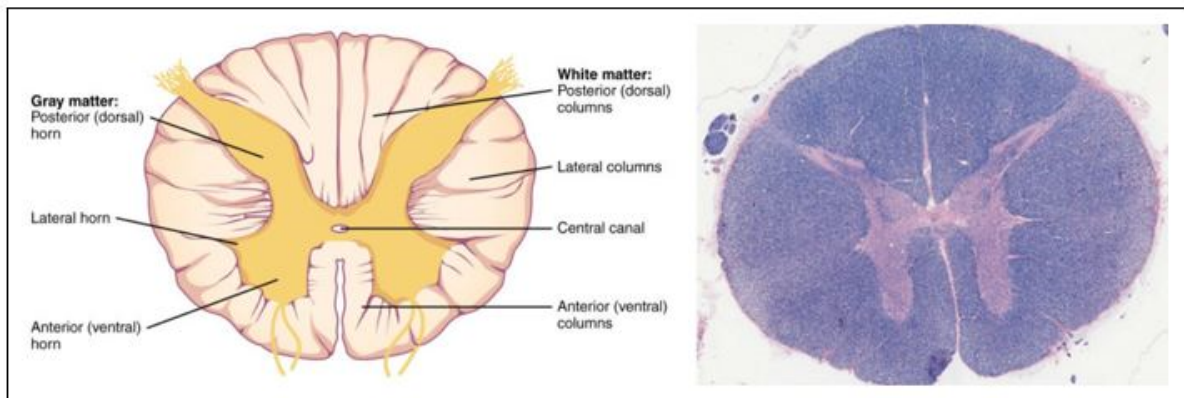


Figure 1.8 The cross-section of a thoracic spinal cord segment demonstrates the white matter anterior, posterior, and lateral columns, as well as the grey matter anterior, posterior, and lateral horns
 ("The Central Nervous System," n.d.)

The nerve cells inside the spinal cord are known as neurons, which are made of a cell body, dendrites and an axon. The white matter is composed of bundles of sensory (ascending) and motor (descending) myelinated axons and glial cells. The grey matter is made of cell bodies of motor and sensory neurons, neuroglia cells and unmyelinated axons. The shape and size of the grey matter differ depending on the level of the spinal cord. The ratio of grey and white is higher at the lower levels, particularly because in lower level of the spine, there are fewer ascending and descending nervous fibers. The cell body, also known as soma, is the spherical portion of the neuron that comprises the nucleus and produce the proteins required to maintain the functions of the cell. The cell body binds to dendrites that provide electrical signals to the neuron and the axon that transfers information to other neurons. Axons are covered by myelin, which is a lipid-rich (fatty) material, to insulate them and increases the rate of transmitting electrical impulses along the axon. At the end of the nervous system, there are axon terminals that link the adjacent neuron through the synapse, which enables a neuron to send an electrochemical signal to another neuron or to a target cell (Figure 1.9) (Cho, 2015; "The Spinal Cord," n.d.).

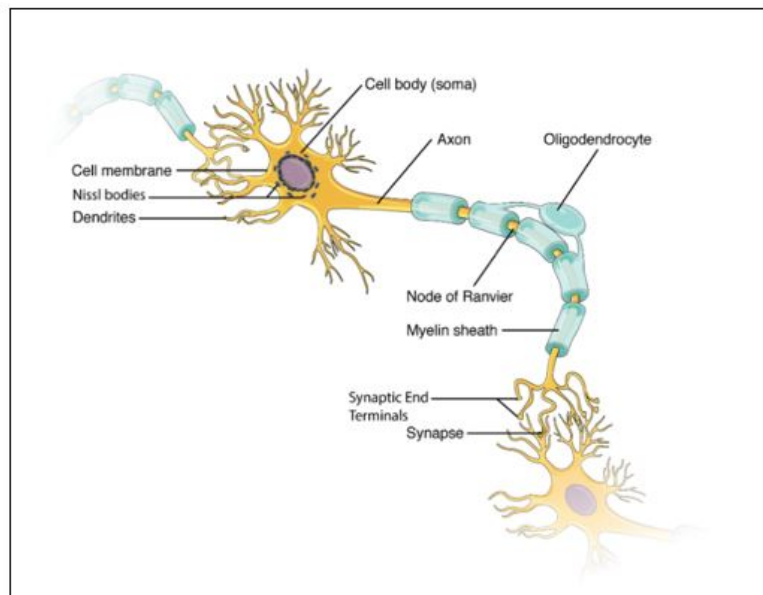


Figure 1.9 Human Neuron Anatomy. The direction of electrical impulses traveling is from the left side to the right side.
(Biga et al., n.d.)

Glial cells are non-neuronal cells in the central nervous system (CNS) and include oligodendrocytes, astrocytes, ependymal cells, and microglia that each have different functions to support neurons (Fields et al., 2014). The main function of the oligodendrocytes is to insulate a neuron from another and provide protection (Jessen & Mirsky, 1980). Astrocytes have numerous functions within the central nervous system. Their most important role is to supply neurons with nutrients and oxygen. Ependymal cells function are involved in the circulation of the CSF, which supplies nutrients to the neurons and remove harmful molecules. Microglia is responsible of the immune defense of the spinal cord, by destroying pathogens and eliminating dead neurons (Yu, 2019).

The grey matter is divided into four major columns: the dorsal horn, the intermediate column, the lateral horn and the ventral horn. The dorsal horn (also recognized as the posterior horn) comprises neurons that collect somatosensory information from the body, which are then transmitted to the brain through the ascending pathways. The posterior horn is close to the spine surface and receive sensory signals that allow continuous interaction among the body

and the environment. The ventral horn (also identified as the anterior horn) mainly contains motor neurons that leave the spinal cord to innervate skeletal muscles, thus allowing motion. The intermediate column and the lateral horn include neurons that innervate visceral and pelvic organs. The role of the lateral horn is to regulate the autonomic nervous system through the activation of the sympathetic nervous system. In accordance with its numerous functions, the grey matter has randomly oriented axons with multiple cell bodies scattered across the body (Mercadante. & Tadi., 2020; Yu, 2019).

The white matter covering the grey matter includes myelinated and unmyelinated nerve fibers. These fibers provide information up or down the cord (ascending or descending) as displayed in Figure 1.10. The spinothalamic tract is the most relevant ascending tract, a sensory path that transmits pain, temperature, and crude contact from the skin to the thalamus. External compression of the spinal cord can result in increased sensory loss (Ahuja et al., 2017). The corticospinal tract is the most noticeable descending tract. Vibration, proprioception and fine touch are transmitted via corticospinal tract. Axial muscle, body posture, balance and head motions are regulated by the medial descending motor systems. Traumatic spinal cord injury (TSCI), specifically above T5-level injuries, and defects of descending tracts of spinal cord is linked with serious and debilitating cardiovascular, gastrointestinal, bladder, and sexual dysfunction (Cho, 2015).

The white matter is split into three columns, the dorsal column (or posterior), the lateral column and the ventral column (or anterior). In the white matter, three general types of nerve fibers can be differentiated. Long ascending nerve fibers emanating from the column cells, long descending nerve fibers emerging from the cerebral cortex various brain nuclei and shorter nerve fibers connect different levels of the spinal cord. While ascending tracts are located in all columns, descending tracts are contained only in the lateral and anterior columns ("Anatomy of the Spinal Cord," n.d.).

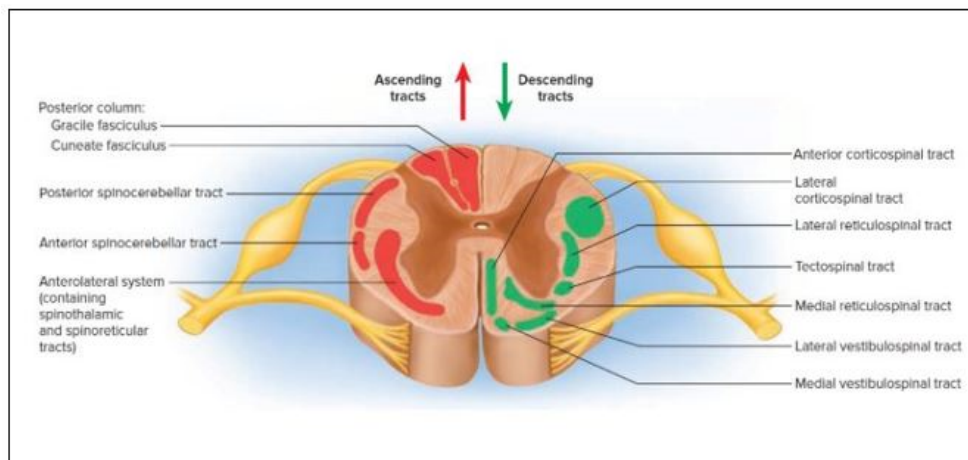


Figure 1.10 Human Spinal Cord Tracts
("Spinal Cord," n.d.)

1.2 Overview of Spinal Cord Injury

A spinal cord injury (SCI) is characterized by a spinal cord damage that causes permanent changes in strength, sensation and other functions of the body. It is categorized into traumatic and non-traumatic injuries. SCI generally results from the compression or transection of the cord. The most commonly identified injury mechanisms in clinical SCI are compression, contusion, laceration, transection, and traction of the spinal cord (Norenberg et al., 2004).

1.2.1 Pathology of Spinal Cord Injury

Pathophysiologically, traumatic SCI is classified into primary and secondary injuries and can be temporarily classified into acute, subacute, intermediate and chronic stages. The primary injury causes significant mechanical damage to neurons and cells of the central nervous system, generally by compression or shear of the spinal cord. These events rapidly initiate a prolonged sequence of secondary injury such as spinal cord edema, ischemia, free radical damage, electrolyte imbalance, excitotoxicity, inflammation and apoptosis (Ahuja et al., 2017; Norenberg et al., 2004), resulting in additional damage to the spinal cord. Secondary injury occurs minutes after the primary injury, causing incremental damage to the spinal cord around the lesion site for weeks or months (Alizadeh et al., 2019). The spinal cord swells for hours

after the injury. The swelling accelerates tissue degeneration, leads to further mechanical compression of the cord, spreads to several parts of the spinal cord and makes the injury worse (Ahuja et al., 2017). After spinal cord primary injury, vascular disruption and ischemia occur and lead to glial activation, oxidative stress and neuroinflammation. These severe changes cause axonal injury, cell death, matrix remodeling and glial scar's formation (Alizadeh et al., 2019). A summary of secondary injury processes is represented in Figure 1.11.

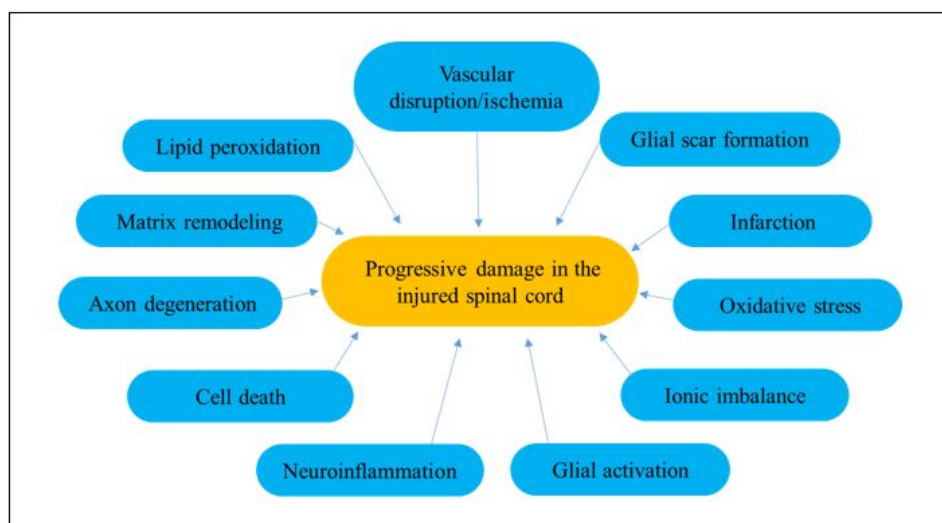


Figure 1.11 Summary of secondary injury processes following TSCI
(Alizadeh et al., 2019)

1.2.2 Epidemiology and Demographics

It has been estimated that the number of individuals with SCI in the United States is approximately 282,000, with around 17,000 new cases per year ("Spinal cord injury facts and figures at a glance," 2012). In North America, the incidence of traumatic SCI is 39 cases per 1 million people, which is greater than Australia (16 cases per 1 million people) or Western Europe (15 cases per 1 million people) (Cripps et al., 2010). The occurrence of non-traumatic SCI was measured to 1,227 cases per million individual in Canada and 364 cases per million in Australia (New et al., 2013). Traumatic SCI is more common among males (79.8 %) than in females (20.2%). The primary cause of the traumatic SCIs is motor vehicle accidents,

followed by falls and sports injuries (Chen et al., 2016). SCI leads to reduce mobility and function based on the severity and completeness of the injury. The average health care annual expenses as well as living and expected lifetime cost directly due to the SCI vary depending on the level of neurological dysfunction. For the first year, the range is approximately between 347,000 USD and 1,000,000 USD. In the following year, it is almost between 43,000 USD and 185,000 USD. Additionally, there are indirect costs of nearly 72,000 USD per year for losses income, retirement benefits and efficiency costs ("Spinal cord injury facts and figures at a glance," 2012).

The importance of prevention strategies of spinal cord injury is demonstrated by significant physical, psychological, and economic implications. Recognizing the emerging patterns in the demographic SCI is the key to design successful preventive measures for the individuals at risk of serious injury. With an average of 42%, car accidents appear to be the leading cause of SCI. Injuries resulting from falls stand in second place among adults, with an average of 20% (Chen et al., 2016). A summary of the causes of SCI is shown in Figure 1.12. The social and economic impact of TSCI affects not only the patient and their direct relatives, but also the community and society as a whole (Sekhon & Fehlings, 2001).

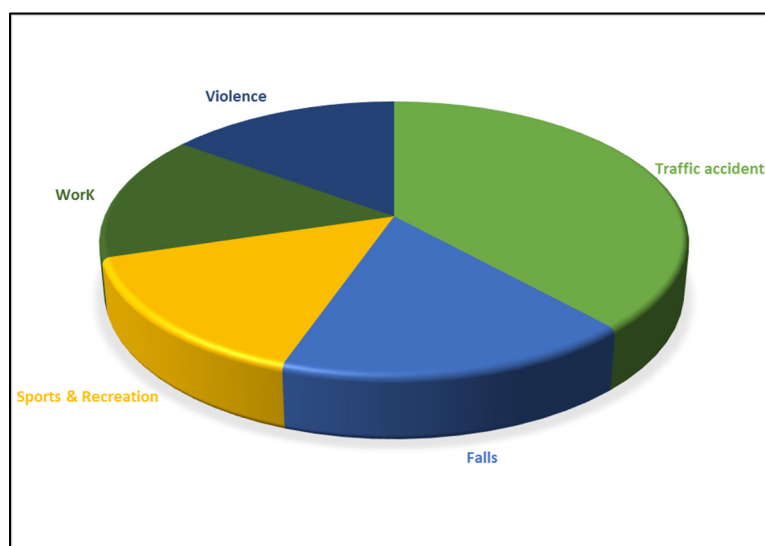


Figure 1.12 Etiology of Adult Spinal Cord Injury
(Sekhon & Fehlings, 2001)

Age, injury level and neurological grade are the most relevant premorbid criteria for recovery following severe SCI. The cervical region is the most prevalent site of severe SCI with approximately 55%, while the three other regions (thoracic, thoracolumbar, lumbosacral) share almost equally the remaining 45%, as illustrated in Figure 1.13 (Sekhon & Fehlings, 2001). Furthermore, there has been a small but statistically significant trend toward an increasing of cervical injuries percentage in recent years, ranging from 53.5% in the 1970s to 56.5% in 2000s (Jackson et al., 2004).

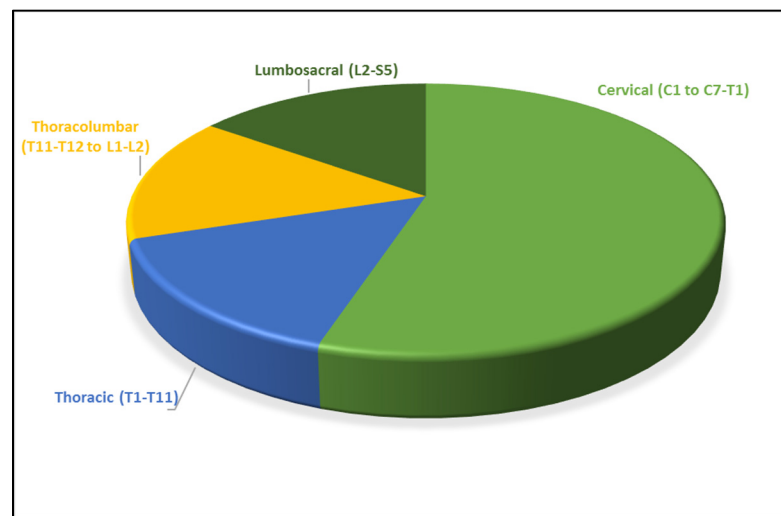


Figure 1.13 Level of Injury in Adult Spinal Cord Injury (Sekhon & Fehlings, 2001).

1.2.3 Spinal Cord Injury Diagnostic

In vivo spinal cord imaging is frequently used to diagnose neurological disorders in patients. X-ray, CT, and MRI are the most widely used radiology instrument to evaluate a spinal cord injury. X-rays are useful for identifying any bone fracture and dislocation accidents that have occurred with SCI (Ahuja et al., 2017). CT is more efficient in the evaluation of extent of the bone injuries in patients (Acheson et al., 1987). CT is less effective for assessing the integrity of soft tissues, including the spinal cord, the intervertebral discs, the ligaments and the nerve roots, but MRI is well adapted for evaluating these soft structures (Vaccaro et al., 2013). Quantitative MRI methods applied to the spinal cord are effective for estimating diagnosis and

tracking the treatment response in clinical research and in prospective studies (Abdel-Aziz & Ciccarelli, 2014). MRI can recognize the deformation of the spinal cord and determine the existence of edema and haemorrhage (Ahuja et al., 2017). It is also important to remove the compressive fragments and to verify the site and severity of the injury (Cho, 2015).

1.3 Experimental Modeling of Spinal Cord Injury

1.3.1 Animal models

Tissue biomechanics have been investigated using different types of model, each of which had advantages and disadvantages. Simulation approaches enable the analysis of parameters that are technically difficult for physical measurements, but need to be validated against experimental data; therefore, they are of limited use in different fields of research. Human volunteers enable to be investigated physiological responses (in vivo experiments); however, injurious level testing is impossible. Human cadavers present human anatomy. Damages can be inflicted and identified (in vitro experiments), but they are restricted by their lack of musculature and, commonly, by the advanced age of the tissue providers (Toen, 2013).

The most relevant animal model used experimentally to study spinal cord injuries is the rat model. The advantages of using rat models include their low cost and similarity to human pathophysiologically. On the other hand, there are disadvantages of using rat model including the differences in physiology and anatomy in comparison with human. The length and the diameter of the rat spinal cord is 90 mm and 3.5 mm respectively, which is significantly smaller than human's one (Yu, 2019). The discrepancy in anatomical size between rat and human spinal cord has prompted the use of larger animal specimens for spinal cord injury researches. According to Kwon et al., a survey from SCI community concluded that 64%-77% of researchers agreed that for pre-clinical studies, larger animal models are more appropriate and beneficial (Kwon et al., 2009). The advantages of using larger animals such as a porcine is that the cross-section diameter is closer to human. The diameter of the spinal cord in porcine is approximately 7 mm, while it is 8-9 mm in human. A prominent layer of cerebrospinal fluid

(CSF) surrounds the porcine spinal cord, as well as the human's one (Figure 1.14). This makes the porcine a more clinically applicable animal model for evaluating the biodistribution and impact of therapies applied, either intrathecally or extradurally (Lee et al., 2013). The cost of porcine model is the major disadvantages of using such model. It is considerably more expensive than rat models in terms of initial purchasing and consistent nursing (Lee et al., 2013).

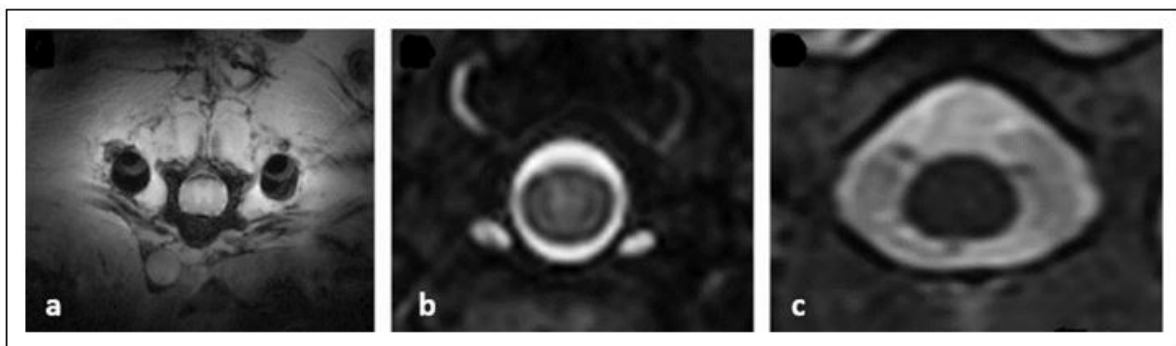


Figure 1.14 Magnetic resonance imaging (MRI) of a Sprague–Dawley rat (a), Yucatan miniature porcine (b), and human (c) at T10 level. A prominent layer of cerebrospinal fluid (CSF) surrounds the porcine spinal cord, as well as the human's one. The porcine spinal cord width is close to the human spinal cord.
(Lee et al., 2013)

It has been demonstrated that the extent of a spinal cord injury depends on many biomechanical factors such as the mechanism of injury, the impact velocity, the depth and the duration of the compression. The impacts of these parameters have been investigated using animal model surrogates, thus enhancing our understanding of the various levels of spinal cord tissue injury and their corresponding biological responses.

1.3.2 Spinal Cord Injury Mechanism

Health professionals can effectively repair structural damage to the spine; however, neural tissue damage cannot be repaired. Several clinical researches have identified the canal occlusion measured on radiographs or CT's after the injury. However, some evidence indicates

that there are patients with incomplete or total neurological dysfunction who do not exhibit severe post-injury occlusion. Initial mechanical deformation of the cord during spinal trauma is generally held to be the origin of the neurological injury. Accordingly, study results showed that post-insult recovery was better predicted by the extent of the cord deformation and the velocity of this deformation than by post-injury occlusion (Carter, 2002).

Real-world spinal cord injury mechanisms are hard to determine since many epidemiological studies lack this information. Clinical trials usually concentrate on the diagnosis of the resulting injuries rather than the particular loading condition that was present at the time of the injury. Fortunately, biomechanical studies were able to provide specific information on the loads causing a spinal cord injury throughout real-world incidents and provide additional data for epidemiological studies (Toen, 2013). Using SCI animal model, clinically important primary injuries were reproduced by five injury mechanisms: contusion, distraction, dislocation, transection, and compression (Cheriyana et al., 2014a; Choo et al., 2007; Choo et al., 2009; Clarke et al., 2008; Fiford et al., 2004).

The contusion model is the most commonly used for the development of SCI. In this model, a dropped weight or an electromagnetic impactor directly hits the spinal cord (Cheriyana et al., 2014b). Distraction models generate SCI with tensile stretching of the spinal cord using a force- or displacement-controlled electromagnetic actuator. To do so, a set of vertebrae is fixed while a set of vertebrae is caudally distracted. This methodology reproduces flexion-distraction injuries observed in vehicle accidents (Choo et al., 2009; Yu, 2019). Dislocation methods translate one vertebra over its adjacent vertebra, either dorsoventrally or mediolaterally to produce a SCI. As a result, the neighboring vertebrae are no longer properly aligned, causing a shear force on the spinal cord (Pintar et al., 1989). A normal spinal cord and three spinal cord injury mechanisms including contusion, dislocation and distraction are illustrated in Figure 1.15.

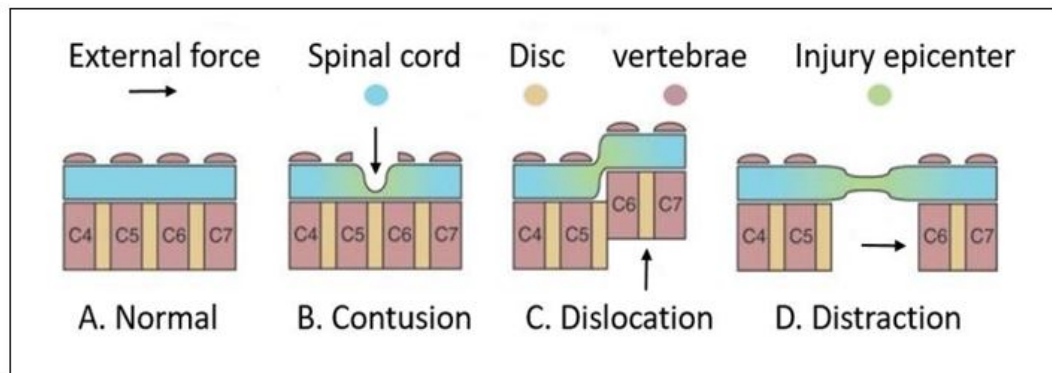


Figure 1.15 Schematic diagrams of a normal spinal cord and three spinal cord injury mechanisms
(Chen et al., 2015)

Transection models can be complete or partial. The complete model entirely separates the rostral and caudal parts of the spinal cord, while the partial model requires partial separation of the spinal cord. Complete transections are effective for the investigation of axonal regeneration and are easily accessible. While highly replicable, they are not highly functionally significant, as full transections are not frequently seen. Partial transections are valuable in evaluating the differences between healthy and impaired fibers (Carter, 2002).

Compression models require extended compression of the spinal cord; therefore, compression models differ from contusion models. In fact, some of these models are contusion-compression models with an acute impact and persistent cord compression. This process is found in SCI caused by vertebral dislocations and burst fractures. Clip and balloon compression are two methods utilized to mimic models of compression injury. For instance, a modified aneurysm clip has been used to produce a spinal cord injury. In the balloon compression method, a catheter with a small inflatable balloon is inserted into the subdural space and filled with air or saline to compress the spinal cord (Cheriyian et al., 2014b).

Each of these concepts of injury has demonstrated a distinct tissue damage pattern. Contusion models spared peripheral white matter, while dislocation damaged axons in the lateral white matter (Kohn, 1995). Models of distraction and dislocation displayed more disruption to white

matter than contusion models. The hemorrhage rate in the grey matter were similar between contusion and dislocation models, whilst distraction models showed almost none. Different damages were found between antero-posterior and lateral fracture dislocation models. Significantly, more hemorrhage was found with antero-posterior dislocation than with lateral dislocation. Dorsal and ventral white matter damages were observed rostrally and caudally in antero-posterior dislocation. Conversely, lateral dislocation caused left and right lateral injuries to the white matter. Both models witnessed damage to the tissue at center of the injury. These various results illustrate the significance of injury mechanisms in the experimental modelling of SCI (Fredø et al., 2012; Yu, 2019).

1.3.3 Effect of Depth, Velocity and Duration

Noyes et al. have demonstrated that increasing the depth of contusion increases the volume of the lesion (Noyes, 1987). Fiford et al. revealed that a dislocation with higher relative displacement of each vertebrae caused more axonal injury (Fiford et al., 2004). Sparrey et al. observed that a high dynamic impact considerably increases the hemorrhage volume in the spinal cord white matter, as opposed to lower dynamic impact. On the other hand, the velocity of injury does not influence the hemorrhage of the spinal cord grey matter (Sparrey et al., 2008). Researches that studied the influence of the depth and velocity in contusion and their interaction showed that the white matter is affected by the interaction of depth and velocity of the injury, while the grey matter is only affected by the injury depth (Lam et al., 2014; Yu, 2019). It has also been shown that sustained compression contributes to injury severity. In a contusion model, Sjøvold et al. applied 0%, 40% and 90% residual compression, which is the compression that remain in the material after the original cause has been removed, during 60 minutes. In 90% residual compression, 60-86% more neural nuclei damage has been found in the grey matter when compared to 40% residual compression. Therefore, according to Sjøvold et al., 2013, a high rate of residual compression of the spinal cord could potentially increase the extent of damage to the tissue, whilst a lower rate could have little or no effect (Sjøvold et al., 2013). A histological review of Dimar et al. revealed that increasing the extent and duration of spinal canal narrowing lead to severe damage to the spinal cord. Furthermore, it seems that

the longer spinal cord compression occurs following incomplete spinal cord injury, the weaker the neurological rehabilitation prognosis (Dimar et al., 1999).

1.4 Finite Element Modeling of the Spinal Cord

Finite element modeling of spinal cord injuries offers valuable step towards a better understanding of the spinal cord biomechanics. Ultimately, they can be used to improve the ways we prevent and treat these injuries (Maikos et al., 2008). In order to increase our understanding of computational modeling, the fundamentals of finite element modelling will be briefly described.

1.4.1 Finite Element Modeling

Finite element simulation is a computational engineering technique that, from a mechanical perspective, analyze the stresses and strains in a structure. Stress is defined as a force per unit area, whilst strain is described by the ratio of the length change to the initial length. In this approach, a continuous solid is divided into a number of elements attached to nodes. These elements are sufficiently small to reproduce the mechanical behavior of the material. The model calculates stresses and strains at every individual nodes. The stresses and strains of each elements of the material are then interpolated (Yu, 2019). Finite element analysis is a complementary tool to experiments since they provide information that are not available otherwise. This links the spinal cord impact with spinal cord injury, thus aligning tissue injury distributions with relevant pathologies (Maikos et al., 2008).

1.4.2 Constitutive Models

The computation of internal stresses and strains resulting from finite element modeling depends on the structure's material model. Linear and non-linear elastic, linear, non-linear and quasi-linear viscoelastic (QLV), as well as poroelastic models have been applied specifically to the nervous tissue (Cheng & Bilston, 2007; Jannesar et al., 2018; Maikos et al., 2008; Russell

et al., 2012). Each of these models explains how stresses and strains are linked. The most common model for engineering materials is the linear elastic model, which uses a linear relationship between stresses (σ) and strains (ε). This relationship is described by the elastic modulus (E) of the material, as shown in Equation (1.1).

$$\sigma = E\varepsilon \quad (1.1)$$

The bulk modulus (K) describes the material tolerance to compression, by relating the applied pressure to the change in volume, as shown in Equation (1.2).

$$P = -K \frac{(V_n - V_0)}{V_0} \quad (1.2)$$

where P is the pressure, V_0 is the initial volume of the material, and V_n is the diminished volume of the material resulting from the pressure applied.

Non-linear elasticity defines component that has a non-linear stress-strain relationship. Most biological soft tissues are non-linear elastic. They are also hyperelastic, which means that they can sustain high strain without failure. Non-linear hyperelastic behavior can be defined by a strain energy density function. Strain energy is the energy accumulated in a body following a deformation. The strain energy per unit volume is known as the strain energy density and is the area below the stress-strain curve up to the point of deformation.

Equation (1.3) shows an example of a non-linear model typically used to describe the mechanical behavior of several biological tissues including tendon, ligament and spinal cord (Bilston & Thibault, 1995; Clarke et al., 2009; Fiford & Bilston, 2005). Moreover, the hyperelastic Ogden model, which has been used to describe non-linearity response of the spinal cord components under compression, is presented in Equation 1.4.

$$\sigma = A(e^{B\epsilon} - 1) \quad (1.3)$$

where both A and B are material constants.

The form of the non-linear hyperelastic Ogden strain energy potential is shown below.

$$U = \sum_{i=1}^N \frac{2\mu_i}{\alpha_i^2} (\bar{\lambda}_1^{\alpha_i} - \bar{\lambda}_2^{\alpha_i} - \bar{\lambda}_3^{\alpha_i} - 3) + \sum_{i=1}^N \frac{1}{D_i} (J^{el} - 1)^{2i} \quad (1.4)$$

where $\bar{\lambda}_i$ are the deviatoric principal stretches $\bar{\lambda}_i = J^{-\frac{1}{3}}\lambda_i$, λ_i are the principal stretches, N is a material parameter; and μ_i , α_i and D_i are temperature-dependent material parameters.

The initial shear modulus and bulk modulus for the Ogden model are given by the following equations:

$$\mu_0 = \sum_{i=1}^N \mu_i \quad (1.5)$$

$$K_0 = \frac{2}{D_1} \quad (1.6)$$

where μ_0 and k_0 are initial shear and bulk modulus, respectively.

Viscoelastic material displays time-dependent behavior by showing both viscous (fluid) and elastic (solid) properties while enduring deformation. Viscous materials withstand shear flow and strain linearly where stress is applied. Elastic materials deform when stretched and quickly return to their original shape when the load is removed. Two loading procedures can be used to describe viscoelasticity: creep and stress relaxation. Creep refers to a procedure where continuous stress is applied, leading to an increase in strain during time. Stress relaxation, on the other hand, refers to the method where a strain is applied and hold to a specified value. The

strain applied corresponds to an increase in stress whereas the holding process causes a decrease in stress during time (Yu, 2019).

Several models represent viscoelastic materials. Linear viscoelastic models are adequate for small strain, where stress changes linearly with strain. For example, Boltzmann's formulation (Equation (1.7)) displays a unique relationship between the Cauchy stress tensor $\sigma(t)$ and the strain tensor function $\epsilon(t)$ (Geris, 2013).

$$\sigma(t) = \int_0^t G(t - \tau) \frac{d\epsilon(\tau)}{d\tau} d\tau \quad (1.7)$$

where $G(t)$ is a relaxation tensor function.

Due to their non-linear behavior, linear viscoelastic models are insufficient to fully characterize soft tissues. Therefore, non-linear viscoelasticity models are used in these situations. Quasi-linear viscoelastic (QLV) and fully non-linear viscoelastic models both describe non-linear viscoelasticity. To characterize viscoelastic behavior of soft tissues, quasi linear viscoelastic models have been frequently used in the literature (Jannesar et al., 2018; Jannesar et al., 2016). In these models, the time dependent and the elastic component of the mechanical behavior are defined separately (Yu, 2019), as shown in Equation (1.8).

$$\sigma(\epsilon, t) = \int_0^t G(t - \tau) \frac{\partial \sigma^e(\epsilon)}{\partial \epsilon} \frac{\partial \epsilon(\tau)}{\partial \tau} d\tau \quad (1.8)$$

where $\sigma^e(\epsilon)$ and $G(t)$ respectively represents the corresponding stress to an instantaneous strain within a uniaxial loading period and the reduced relaxation function. Equation (1.3) is commonly used to describe $\sigma^e(\epsilon)$, while a 3-term Prony series (Equation (1.9) with $n=3$) is commonly used to describe $G(t)$ (Jannesar et al., 2018; Yu, 2019).

$$G(t) = 1 - \sum_{i=1}^n g_i (1 - e^{-\frac{t}{\tau_i}}) \quad (1.9)$$

where, g_i represents the relative moduli, τ_i is the relaxation time of the term (i) in the Prony series and n displays the number of terms in the Prony series.

Poroelastic models represent the behavior of both solid and fluid phases of biphasic materials. In fact, the interaction between fluid flow and solids in porous medium is defined by poroelasticity (Eisenfeld et al., 1978). Porous materials, such as biological tissues, are solid materials with pores or voids filled with fluid. When an external load is applied to a porous material, the pores filled with fluid undergo a pressure change accompanied by fluid movement. The solid part shifts and elastically deforms (Malandrino & Moeendarbary, 2017). The solid part is elastic while the fluid part is presumed incompressible. Viscoelasticity is defined by the relationship between solid and fluid in both phases (Mow et al., 1980).

1.4.3 Finite Element Models of the Spinal Cord

Multiple constitutive models were integrated and validated using finite element models (FEM) in order to analyze spinal cord internal stress and strain distributions (Jannesar et al., 2018; Maikos et al., 2008).

Results from FEM entirely depend on their material characteristics, as can be observed in studies where finite element were used to simulate animal models of SCI. A weight-drop contusion experiment in rats was modeled by Maikos et al. (2008). Viscoelastic properties were extracted from brain tissue. Discrepancies between grey and white matter properties were neglected and the spinal cord was defined as an isotropic material (Maikos et al., 2008; Russell et al., 2012). Maximum principal strain showed a stronger correlation with grey matter tissue damage ($R^2 = 0.84$) than white matter tissue damage ($R^2 = 0.56$) (Maikos et al., 2008). Contusion and dislocation experiments of Choo et al., 2009 have been modeled by Russell et

al., 2012 with hyperviscoelastic Ogden and Prony material properties for the cord and dura presented by Maikos et al., 2008. Spinal cord hyperelastic properties were based on experiments performed on rat spinal cord by Fiford and Bilston (2005), combined with viscoelastic properties of brain tissue from Mendis et al., (1995). These material properties were then calibrated by Maikos et al., 2008 to fit their weight-drop experimental behavior. Properties for the dura mater were derived by mechanical testing of rat dura mater by Maikos et al., 2008.

and showed a significant correlation for both contusion ($R^2 = 0.86$) and dislocation ($R^2 = 0.52$). Maximum principal strain showed a stronger correlation with damage to grey matter ($R^2 = 0.93$) than white matter ($0.38 < R^2 < 0.96$) (Russell et al., 2012; Yu, 2019).

A recent study by Jannesar et al. has recognized the importance of using separate properties for spinal cord grey and white matter to improve the reliability of computational models. In their study, a FEM of a spinal cord was compared with the histological analysis of tissue damage sustained from a contusion experiment in nonhuman primates (Jannesar et al., 2016). Four finite element models with different combinations of material properties for both grey and white matter were used in four strain rate values $5s^{-1}$, $0.5s^{-1}$, $0.05s^{-1}$, and $0.005s^{-1}$ (Table 1.1).

Table 1.1 Combinations of material properties for the spinal cord grey and white matter in finite element simulations used by (Jannesar et al., 2016)

Model A	Different properties for white and grey matter and a distinct pia matter	Anisotropic white matter	Isotropic grey matter
Model B	Different properties for white and grey matter and a distinct pia matter	Isotropic white matter	Isotropic grey matter
Model C	Same properties for white and grey matter and a distinct pia matter	Isotropic white matter	Isotropic grey matter
Model D	Same properties for white matter, grey matter and pia mater	Isotropic white matter	Isotropic grey matter

The extent of the maximum principal strain (MPS) reported in model A differed through the spinal cord when compared to other models. Models A and D displayed similar proportional decreases in MPS away from the injury epicenter while model B revealed high strain on the contralateral side. Model C neglected tissue damage at the impactor level (Jannesar et al., 2016). The distribution of MPS in each model is presented in Figure 1.16 at the injury epicenter at maximum compression. **This research confirms the need for accurate quantification of the material properties of the spinal cord grey and white matter tissues.**

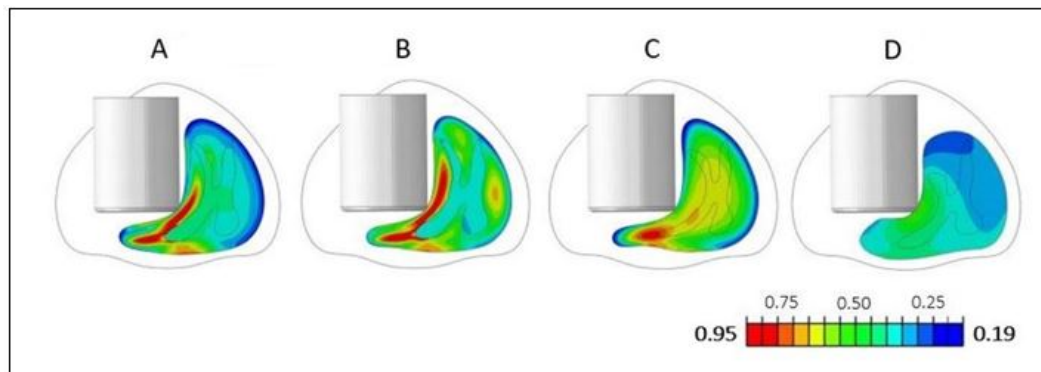


Figure 1.16 Maximum Principal Strain MPS distribution at non-human primate contusion impact in spinal cord white and grey matter at the injury epicenter. The Columns (A-D) stand for (A) model A, (B) model B, (C) model C, and (D) model D (Jannesar et al., 2016)

A more recent study presented by Fournely et al. revealed the effect of spinal cord material properties on strain distribution in 8 spinal cord anatomical regions (Fournely et al., 2020). Different data sets were used in this study to model white and grey matter properties, which are shown in Table 1.2. First model used experimental data from the study of Ichihara et al. (2001) on bovine spinal cord; second model used the model of mechanical behavior of rat spinal cord developed by Maikos et al. (2008), and the third model is used non-human primates material behavior from the recent work of Jannesar et al. (2016). Hyperelastic mechanical behavior of white and grey matter were modeled using first order Ogden laws, and Prony series modeled the viscoelastic behavior of the materials.

Table 1.2 Different material properties for the spinal cord grey and white matter in finite element simulations

Model 1	Distinct WM and GM (GM twice stiffer than WM)	Bovine	(Ichihara et al., 2001)
Model 2	Uniform WM and GM	Rat	(Maikos et al., 2008)
Model 3	Distinct WM and GM (WM stiffer than GM)	Non-human primates	(Jannesar et al., 2016)

According to the results obtained, strain distribution throughout the spinal cord was significantly affected by changing in material properties between white and grey matter. In addition, in the study of Yu et al. (2020), the effect of tissue type, direction, and the interaction between them on the mechanical properties of the spinal cord components (white and grey matter) were analyzed in compression. The analysis revealed a significant effect of tissue type and a weak effect of direction to the mechanical properties of the spinal cord. This shows that the spinal cord tissue exhibits heterogeneous and has isotropic mechanical properties in compression. This emphasized the need for comprehensive identification of the properties of the white and gray matter to develop models capable of predicting spinal cord injuries.

1.5 Mechanical Properties of Spinal Cord

Various studies have characterized the mechanical properties of spinal cord white and grey matter. These studies have demonstrated that the properties of the spinal cord tissues are susceptible to several experimental variables including strain rate, preconditioning, time post mortem, sample orientation, donor age, material composition, loading direction, loading type, loading time and spinal level (Bilston & Thibault, 1995; Chang et al., 1988; Clarke, 2011; Fiford & Bilston, 2005; Fradet et al., 2016; Karimi et al., 2017; Mazuchowski & Thibault, 2002; Oakland et al., 2006; Ramo et al., 2018; Shetye et al., 2014a; Sparrey & Keaveny, 2011). Prior to explaining spinal cord mechanical properties, different forms of loading will first be clarified.

1.5.1 Loading Type

Several methods can be used to investigate mechanical properties of soft tissues. Tensile testing, confined and unconfined compression testing, and indentation testing (localized compression) are some examples. First studies on mechanical properties of the spinal cord were tensile analysis. Both *in vivo* and *ex-vivo* tensile testing of spinal cord have been conducted in the literature. Tensile deformation is obtained by stretching the spinal cord in axial direction. *In vivo* analysis of the spinal cord of cats and puppies used multiple sets of rings positioned around the spinal cord (Chang et al., 1988; Hung & Chang, 1981) while in *ex-vivo* experiments, two ends of the spinal cord were tightened between two rigid clamps to apply a tensile loading (Bilston & Thibault, 1995; Fiford & Bilston, 2005; Haslach et al., 2014; Shetye et al., 2014a; Yu et al., 2020). Unconfined compression axially compresses spinal cord tissue between two parallel platens and enables the sample to laterally expand (Jannesar et al., 2018; Sparrey & Keaveny, 2011). In confined compression, the tissue is inserted into a container chamber with rigid walls to prevent lateral expansion (Cheng & Bilston, 2007; Haslach et al., 2014; Yu et al., 2020). A permeable filter is set underneath the specimen. Due to the biphasic aspect of the tissue, when the tissue is squeezed, the fluid flows through the filter causing the solid material to be deformed (Haslach et al., 2014).

The regional mechanical properties of the tissue can be determined with indentation method. Usually, a round indenter is used to compress the tissue to the required level. The distinction between this method and unconfined and confined compression is that the entire cross-section of the tissue is not covered by the indenter. This technique can be used to analyze spinal cord grey and white matter separately (Feng et al., 2013; Koser et al., 2015). The method is particularly challenging when characterizing the grey matter due to its small size in the spinal cord.

Another type of loading type used to analyze soft tissue mechanical properties is shear. To create shear, the specimen is inserted between two parallel rigid plates. The upper and lower plates then apply mediolateral deformation to the specimen. This method has been used to

investigate brain tissue properties, but has not been utilized to study spinal cord tissue (Budday et al., 2017).

Depending on the loading type, the tissue sample deforms in different ways, and enables to explore the sensitivity of the tissue structure to various forms of loading.

1.5.2 Mechanical properties of intact spinal cord

Precise sets of mechanical properties are required to develop FEM of the spinal cord and study both traumatic and non-traumatic injury mechanisms. The mechanical properties of the intact spinal cord have been investigated on different species in tension. Sample data and the main experimental parameters are presented in Table 1.3 and Figure 1.17, respectively (Clarke, 2011; Yu, 2019).

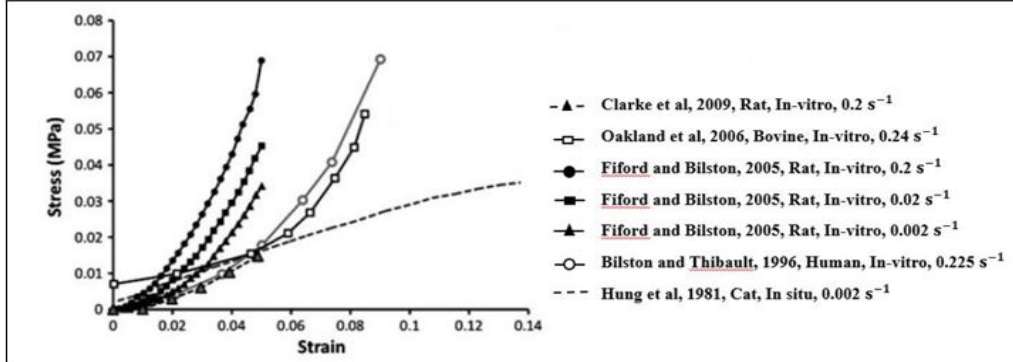


Figure 1.17 Stress-strain data of several studies on spinal cord mechanical properties in tensile testing (Clarke, 2011)

Table 1.3 Summary of main experimental parameters that have been used in the literature to investigate mechanical properties of the spinal cord in tensile testing. The empty cells display that the author did not provide the information.

(Bilston & Thibault, 1995; Clarke et al., 2009; Fiford & Bilston, 2005; Hung & Chang, 1981; Ramo et al., 2018; Shetye et al., 2014a; Yu, 2019)

References	Species	Loading type	Strain rate	Strain %	Environment	Intact spinal cord			
						Peak stress (KPa)	Elastic Modulus (KPa)	Equilibrium Stress (KPa)	Time Constant
Ramo et al., 2018	Porcine	Tension	$0.1(s^{-1})$	1-5	In vivo	30	-	12-22	100
Shetye et al., 2014	Porcine	Tension	$0.1(s^{-1})$	1-5	In vitro	70	-	18-35	100
Clarke et al., 2009	Neonatal Rat	Tension	$0.002-2(s^{-1})$	2-5	In vitro	5-15	-	2.5-8	83
Fiford et al., 2005	Rat	Tension	$0.002-0.02(s^{-1})$	2-5	In vitro	15-75	-	15-50	376
Bilston et al., 1995	Human	Tension	$0.068-0.21(s^{-1})$	10	In vitro	60-90	1020-1370	50-150	234
Hung et al., 1981	Cat and Dog	Tension	$0.021 mm/s$	2	In vivo	-	258, 265	-	-

Those studies showed that the spinal cord demonstrated a non-linear stress-strain response characterized by a strain-stiffening behavior. Hysteresis (difference in the loading and unloading curves) was found during the unloading of the spinal cord, implying that the spinal

cord had viscoelastic properties (Chang et al., 1988; Hung & Chang, 1981; Yu, 2019). Accordingly, other *ex vivo* and *in vivo* experiments indicate non-linear viscoelastic behavior (Bilston & Thibault, 1995; Clarke et al., 2009; Fiford & Bilston, 2005; Ramo et al., 2018; Shetye et al., 2014a). Some studies also reveal the effect of strain rate on material stiffness, whereas increasing the strain rate increases the stiffness (Clarke, 2011). Time dependent properties of the complete spinal cord demonstrated stress relaxation in all experiments. Equilibrium stress increases as the strain rate increases. Both strain and strain rate have an influence on equilibrium stress and stress relaxation (Clarke, 2011; Shetye et al., 2014a).

According to Ramo et al. (2018), who compared the viscoelastic behavior of *in vivo* and *ex vivo* porcine spinal cord specimens, significant increase in relaxation was revealed with applied strain. It has been also identified that the extent of relaxation and stiffness response of *ex vivo* samples are significantly greater than *in vivo* samples. By comparing stress relaxation response at different strain magnitude, the *ex vivo* samples experienced greater relaxation than *in vivo* samples. The relaxation component in the first few seconds (0.1 s, 1 s and 10 s) is more divergent in both *in vivo* and *ex vivo* samples, but *ex vivo* and *in vivo* experiments have identical relaxation response at $t=100$ s. Based on the comparison of short-term and long-term relaxation response of both *ex vivo* and *in vivo* samples, to model dynamic or injurious scenarios, *in vivo* viscoelastic material characterizations have to be included. The use of *ex vivo* data is more appropriate for quasi-static analysis of the spinal cord behavior (Ramo et al., 2018).

Spinal cord has been demonstrated to change with post-mortem time delay. The modulus appears to increase after death (Oakland et al., 2006). Oakland et al. conducted tensile testing of spinal cord during 3, 24, 48 and 72-hour post-mortem. They displayed that tangent modulus increased by increasing time post-mortem as a result of tissue breakdown and degeneration (Oakland et al., 2006). Human tissues in in-vitro studies come from a high average age group of tissue donors; therefore, because of changing in tissue compositions (ratio of gray to white matter), human spinal cord properties could have a relatively high modulus (Clarke, 2011). Mechanical behavior of the spinal cord are affected by the age of the living tissue at the time of the testing. Younger spinal cord is significantly softer in comparison to the adult spinal cord

(Oakland et al., 2006). According to the results from Karimi et al. human spinal cord is softer under the tensile load ($E=89\text{KPa}$) compared to that of the compressive one ($E= 40.12\text{KPa}$) (Karimi et al., 2017). In a study on human spinal cord, Mazuchowski et al. found the significant effect of pia mater to the stiffness of the spinal cord. In this research, they compared elastic modulus of spinal cord with and without pia mater. The results demonstrated that the elastic modulus of the spinal cord with attached pia mater is 10 times stiffer than the spinal cord without pia matter. This study highlights the important role of pia mater in spinal cord structure, as well as the necessity of further investigation of the spinal cord constituents' mechanical properties (Mazuchowski & Thibault, 2002).

1.5.3 Mechanical Properties of the Spinal Cord White and Grey Matter

Different studies have been conducted to characterize spinal cord white and grey matter mechanical properties. Results of two studies performed on mouse and bovine spinal cord demonstrate that grey matter is mechanically more rigid and stiffer than white matter (Ichihara et al., 2001; Koser et al., 2015). On the other hand, another study on rat spinal cord found the white matter to be stiffer than the grey matter (Sharkey, 2018). Comparison of white and grey matter by pipette aspiration method reveals that there is no significant difference in elastic modulus of white and grey matter. In this study, each specimen was fixed on a plate, a glass pipette was connected to a reservoir and a pressure transducer with silicon tubing filled with physiological saline. A micromanipulator was used to set the pipette perpendicular to the white and grey matter, and negative pressure was applied to the samples. The surfaces of the gray and white matter were aspirated using a 0.8-mm-inner-diameter glass pipette. (Ozawa et al., 2001). The main experimental parameters comparing the spinal cord white and grey matter are presented in Table 1.4.

Table 1.4 Summary of main experimental parameters that have been used in the literature to investigate mechanical properties of the spinal cord white and grey matter. The empty cells display that the author did not provide the information.

(Ichihara et al., 2003; Ichihara et al., 2001; Jannesar et al., 2018; Koser et al., 2015; Ozawa et al., 2001; Sparrey & Keaveny, 2011; Yu et al., 2020)

References		Justin Yu et al., 2020	Jannesar et al., 2018	Koser et al., 2015	Sparrey et al., 2011	Ichihara et al., 2003	Ozawa et al., 2001	Ichihara et al., 2001
Species		Porcine	Non-Human Primates	Mouse	Porcine	Cow	Rabbit	Cow
Loading type		Compression (Confined)	Compression (Unconfined)	Indentation	Compression (Unconfined)	Tension	Tension	Tension
Strain rate s^{-1}		0.001	0.3-77	0.02	0.005, 0.05, 0.5, 5	0.0003-0.03	1 cm H_2O/s	0.05
Strain		10%	45%	0.4-0.7%	40%	10-30%	5cm H_2O	5-40%
Time post-mortem		6 Hours	1 Hour	6 Hours	4 Hours	-	1 Hour	-
Peak stress (KPa)	WM	80	7-21	-	0.8-3.9	3-19	-	26
	GM	126	-	-	-	3-24	-	42
Equilibrium Stress (KPa)	WM	99	0.5	-	2	1-5	-	-
	GM	166	-	-	-	1-13	-	-
Elastic Modulus (KPa)	WM	75	-	0.067	-	30-64	3.2	94
	GM	124	-	0.127	-	64-112	3.3	166
Time Constant	WM	10.1	2	-	54	-	-	-
	GM	11.1	-	-	-	-	-	-

According to Ichihara et al. (2003), white and grey matter have different stress distribution, whereas stress distribution within the cord varied with strain rate, compression volume, and the compression location (Ichihara et al., 2003).

In a study on porcine spinal cord white matter by Sparrey and Keaveny (2011), a lower thoracic (T8–T12) spinal cord segment was harvested from a six-month-old Yorkshire porcine weighting 80 lb. The white matter of the spinal cord segment was cut into 1.5 mm thickness samples with a 3-mm-diameter biopsy punch. Samples were compressed with an aluminum plate up to 40% strain of the initial length, which was 0.6 mm. To reduce the friction between the samples and the impactor plate, artificial CSF drops were used. An unconfined compression was performed at a 0.05 s^{-1} strain rate up to 40% strain and the maximum compression was maintained for 60 seconds to observe the short-term relaxation response (Sparrey & Keaveny, 2011). The results of the compression showed that 1) spinal cord is less stiff in compression than tension, 2) compressive properties of the spinal cord is extremely sensitive to loading rate and preload, 3) with post-mortem time, significant variations in results are presented, even if the time is less than four hours (Sparrey & Keaveny, 2011).

Studies also showed that regardless of whether the tissue was in tension or compression, the spinal cord white and grey matter stress-strain relationship displays a strain-stiffening curve. Moreover, the strain rate was correlated directly with increased peak stress (Ichihara et al., 2003; Jannesar et al., 2018; Sparrey & Keaveny, 2011). When the maximum strain was sustained, the grey and white matter tissue displayed immediate relaxation. The behavior was defined as non-linear viscoelastic (Jannesar et al., 2018; Sparrey & Keaveny, 2011).

As reported by Ichihara et al (2003)., the grey matter is more rigid than white matter. The grey matter samples ruptured at lower strain than white matter, $48.6 \pm 8.0\%$ (mean \pm SD) and $126.1 \pm 53.0\%$ (mean \pm SD) respectively. In addition, both stretched and tensile strength extent were smaller in grey matter in comparison to the white matter. Tensile strength in grey matter is $43.4 \pm 3.2\text{ KPa}$ (mean \pm SD) and it is $61.3 \pm 4.2\text{ KPa}$ (mean \pm SD) in white matter. For the strain range between 5-35%, the tangent modulus was significantly larger in grey matter than white matter (Ichihara et al., 2001). According to a study on rat spinal cord at injurious strain by Sharkey et al. (2018), the spinal cord white matter is roughly twice stiffer than grey matter (Sharkey, 2018). This study agree with McCracken et al. and Kruse et al. who used magnetic resonance elastography of in-vivo human brain tissue. These studies revealed

that the shear modulus of the white matter is greater than the grey matter (Kruse et al., 2008; McCracken et al., 2005). The study of Sharkey et al. also agree with the ex-vivo indentation study of Buddy et al., which has been performed on bovine brain tissue. In this study, white matter was 1.4 times stiffer than grey matter (Budday et al., 2015). On the other hand, several studies disagree with Sharkey et al. namely Koser et al., and Ichihara et al., who have performed experiments on mouse and bovine in ex-vivo condition. They found that white matter is less stiff than grey matter by factors of approximately 1.3-2.6 and 1.9 for bovine and mouse, respectively (Ichihara et al., 2001; Koser et al., 2015). The most recent study on porcine spinal cord revealed that the spinal cord grey matter is stiffer than the white matter by a factor of 1.6-2 (Yu et al., 2020). In this study, the cervical (C5-C7) and thoracic (T5-T7 & T10–T14) regions of the spinal cord were harvested from Yorkshire and Yucatan porcines weighting 21.5-48 kg. The spinal cord white and grey matter were cut into 2.8 mm thickness samples with a 2-mm-diameter biopsy punch. The spinal cord samples were located in a confined compression apparatus and compressed with an indenter up to 10% strain of the total length. The spinal cord samples were examined in axial and transverse direction. The confined compression was performed at 0.001 s^{-1} strain rate up to 0.28 mm and the maximum compression was held for 120 seconds to observe the stress relaxation response (Yu et al., 2020).

Regarding to the variation in the animal models used, the strain magnitude, the in-vivo and ex-vivo conditions and the different methods that have been utilized to determine spinal cord material properties, inconsistent results are observed. Therefore, further investigation is required to define the mechanical properties of spinal cord white and grey matter, notably under axial compression.

CHAPTER 2

PROBLEMS AND OBJECTIVES

According to studies on the incidence and prevalence of traumatic spinal cord injuries (TSCI), numerous people suffers from TSCI, following vehicle accidents, falls or sport-related events. This increases the importance of better understanding the biomechanics of spinal cord, thus allowing to better identifying the risk of injury, provide treatment with timely improvements and prevent further damage. This chapter presents the problems to be solved, the objectives and the methodological approach used during this research project.

2.1 Problems

The literature review revealed important findings, but also problems to be solved regarding the biomechanics of the spinal cord:

- When a compression is applied to the spinal cord and maintained for a certain amount of time, the spinal cord relaxes over time, thus showing a viscoelastic behavior ;
- The mechanical properties of the spinal cord white and grey matter are not well defined. Although there are variety of researches addressing this topic, there is no consensus on whether white matter is stiffer than grey matter, as well as the extent of the stiffness;
- Studies performed on the mechanical properties of the white and grey matters have been performed using limited and insufficient relaxation time to fully investigate the material behavior of the spinal cord tissue;
- The excessive softness of the spinal cord makes it difficult to be extracted out of the spine without damage;
- The spinal cord experiences changes in its mechanical properties after extraction out of the spine, due to the time that spinal cord remains without blood and CSF supplies; this may cause inaccurate data when studying its long-term relaxation response;

- The spinal cord is very sensitive to testing conditions (environment, loading conditions, time and duration of the test, time post mortem, species being tested, etc.);
- Finite element models have been developed to reproduce experimental models of spinal cord injury and investigate stress and strain distributions within the spinal cord following impact. FEM enables to more deeply analyze the relations between the mechanical loading applied and the mechanical response of the SC ;
- Finite element models are capable to cover the range of spinal cord deformations (quasi-static to dynamic). Dynamic deformations usually cause spinal cord injuries. Therefore, it can provide insight into the effect of contusion depth in SCI ;
- FEM is useful to study the time dependent properties of the tissue. As spinal cord is a very sensitive tissue that loses its properties after extraction from the spinal column, it is crucial to use FE modeling to investigate spinal cord long-term relaxation behavior.
- Unfortunately, none of the existing models has integrated the long-term relaxation behavior of the spinal cord tissue. This is partly due to the fact that experiments on stress relaxation of the spinal cord are limited to short-time relaxation ;
- Accordingly, there is a need to better understand the long-term relaxation behavior of the spinal cord tissue. Understanding the mechanism of the spinal cord tissue and its injuries lead to analyze the biomechanics of the injury and to find a solution for appropriate and timely treatment.

2.2 Objectives

The main objective of this study is to characterize and model the long-term stress relaxation response of the spinal cord and its components under axial unconfined compression. It is divided into two sub-objectives:

- **SO1:** Perform axial unconfined compression on cadaveric porcine spinal cord to investigate the viscoelastic long-term relaxation response of the spinal cord;

- **SO2:** Develop and calibrate a finite element model of a porcine spinal cord to reproduce the behavior of the porcine spinal cord under axial unconfined compression, including long-term stress relaxation.

2.3 Methodological approach

The methodological approach describes the method used in this study to assess the defined problems and achieve the objectives presented in this chapter. To reach the first objective (SO1), unconfined axial compression is applied on porcine spinal cord *in vitro*. After reaching the maximum intended strain, the compression is maintained for a long enough period to measure long-term relaxation response. To fulfill the second objective (SO2), two finite element models were created. A finite element model was created to obtain the white matter material properties based on the experiment of Sparrey and Keaveny (2011), which performed experiments on porcine spinal cord white matter segments using an experimental protocol close to the current study. In addition, a complete spinal cord model was developed and calibrated (adjustment of the grey matter material properties) using the experimental results provided in this study. The entire defined methodological process intends to improve the knowledge on the biomechanics of the spinal cord. An overview of the methodological approach is presented in Figure 2.1.

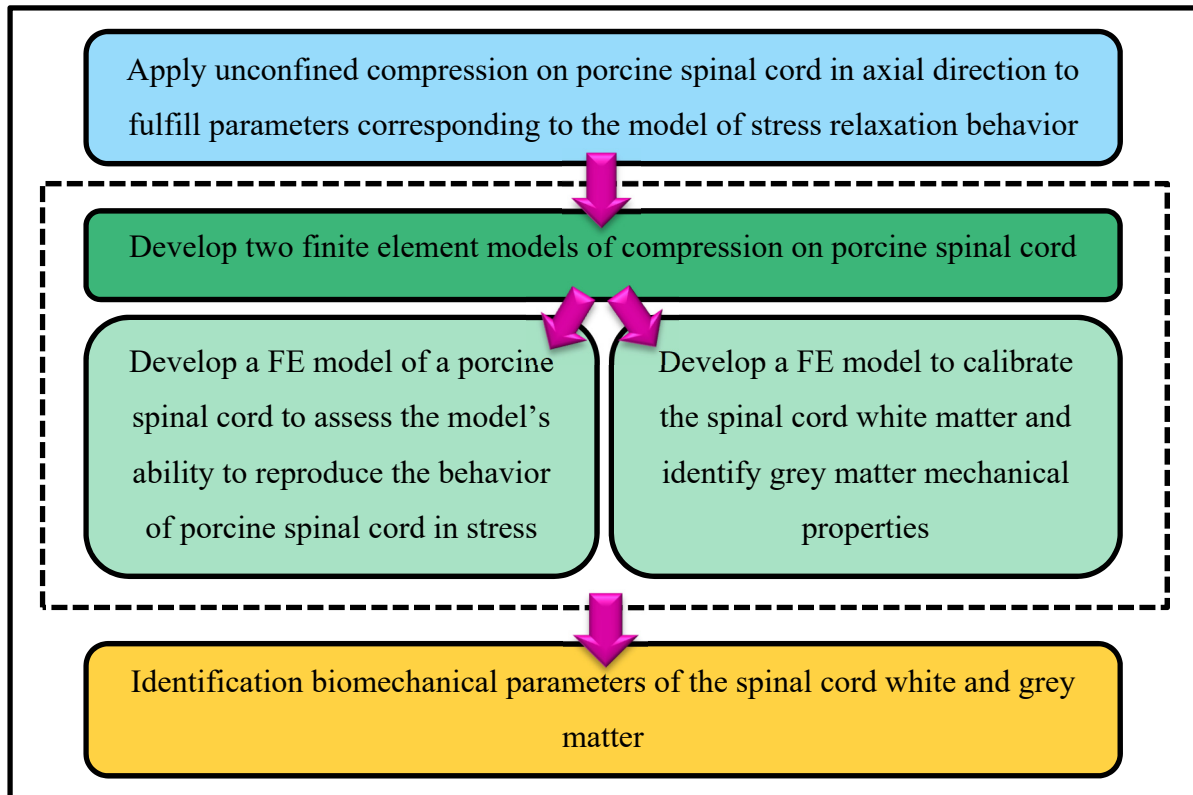


Figure 2.1 Methodological approach

CHAPTER 3

METHODOLOGY

This chapter describes the methodology used to meet the objectives. The steps leading to the experimental characterization of the spinal cord behavior in stress relaxation are first described, followed by the procedure for the implementation and calibration of the finite element model.

3.1 Experimental Characterization of the Loading and Stress Relaxation Behavior of Porcine Spinal Cord under Unconfined Axial Compression

Stress relaxation behavior of human spinal cord is poorly documented in the literature. Therefore, it was necessary to describe its behavior experimentally in order to develop and calibrate the finite element model. Due to the complexity of obtaining fresh human post-mortem spinal cord, a porcine model was used. The reasons for using a porcine model in my project were: 1) the cross-section diameter and injury mechanisms observed on porcine spinal cord are close to human; 2) fresh porcine spinal cord were available at CRCHUM (Centre de Recherche du CHUM), as one of their research group was sacrificing pigs following tests on lung transplantation, and 3) it was possible to limit tissue degeneration by performing mechanical tests in Sophie Lerouge's laboratory at CRCHUM.

For each lung transplantation surgery, three pigs were sacrificed: a donor, a recipient and a backup. In my project, two pigs were used: one receiver and one back-up. No differentiation in sample preparation was done to distinguish between the receiver and the backup since we had no evidence to believe that lung transplantation on the receiver affects the mechanical properties of the spinal cord.

To characterize the mechanical behavior of spinal cord, specimens of porcine spinal cord were placed in a mechanical apparatus with an impactor that compresses the samples to a specific strain. When the maximum strain is reached, the compression is maintained for a period of

time to characterize the stress relaxation behavior. The details of the experiment are described in the following sections.

3.1.1 Spinal Cord Preparation

Two spinal cords were harvested from the thoracic region (T4-T8) of two pigs weighting 58.2 and 65.3 kg. After sacrificing the animal, the spine was extracted with conventional dissection tools and a cast saw. The spinous process and the laminae were removed from the thoracic segments to extract the spinal cord. Fat layer on the spinal cord and all the nerve roots were also removed. The spinal cord was cut to a length of 15 mm using a #10-scalpel blade, as the spinal cord extracted was quite long. This was essentially to ease tissue's handling (Figure 3.1a). The dura-arachnoid mater complex (DAC) was then removed with a scalpel blade and the spinal cord was cut to produce samples of 2.25 mm nominal thickness (Figure 3.1b). The pia mater was conserved. As samples were tested in the axial direction of the spinal cord tissue, it was essential to cut parallel surfaces. If the surfaces are not parallel, a mixture of compression and bending motion will be applied. The cutting process was performed with a cross-section cutting cradle and two sharp razor blades. The cutting cradle had cutting guides, allowing parallel cuts. Four samples were taken from each spinal cord (thoracic level), for a total of eight samples. Each sample was laid in a petri-dish and each petri-dish was wrapped with a gauze, which was sprayed with phosphate buffer saline (PBS) to preserve samples hydration (Figure 3.1c). The preparation and mechanical tests had to be completed in less than six hours. This criterion was used to reduce the influence of the post-mortem time on the mechanical properties of the spinal cord tissue.

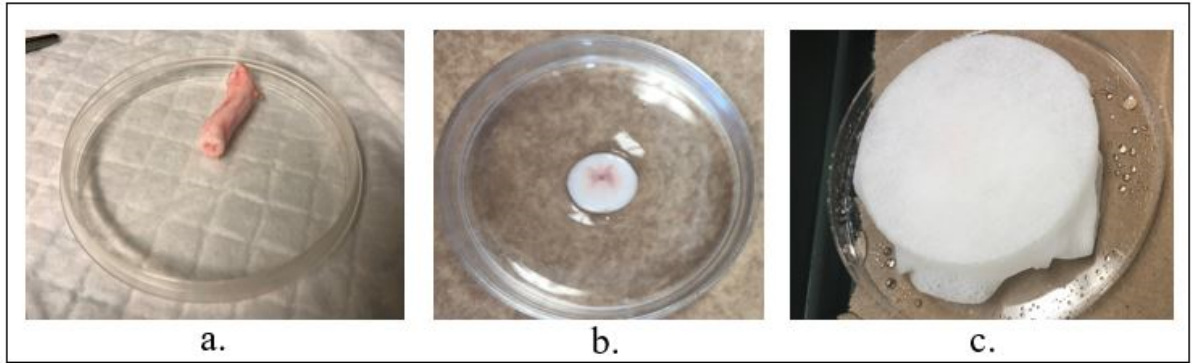


Figure 3.1 Spinal cord preparation. a) 15mm thoracic segment of a porcine spinal cord b) 2.25 mm thick spinal cord sample c) Spinal cord sample wrapped in a sprayed gauze with phosphate buffer saline

3.1.2 Spinal cord area

Engineering stress of a material is defined as the force per unit of initial area (Equation (3.1)).

$$\sigma = \frac{F}{A_i} \quad (3.1)$$

where σ is engineering stress, F is the force applied and A_i represents the initial cross-sectional area of each sample. To obtain the engineering stress, the cross-sectional area has to be measured. Since the cross-sectional area of the spinal cord is oval, the initial cross-sectional area of each sample was approximated by measuring three times the major and minor axis of the eight samples' cross-sections with a digital caliper. After averaging the 3 values of the major and minor axis, and dividing the average values by 2, the average initial cross-sectional area of each spinal cord samples was obtained using Equation 3.2:

$$A_i = \pi ab \quad (3.2)$$

where A_i represents the cross-sectional area of each sample, and a and b are the average values of the semi major and semi minor axis of the spinal cord samples, respectively. The measurements and the average values are presented in Table 3.1. Table 3.1, 2b and 2a present

minor and major axis of the spinal cord samples. Every axis of each spinal cord sample was measured three times. By calculating the average of the three values, the anterior-posterior and the lateral axis of the spinal cord samples were obtained. By using these averaged values and Equation 3.2, the average cross sectional area of the spinal cord samples was calculated.

Table 3.1 Antero-posterior and lateral axis of the cross-section of porcine spinal cord samples

Sample	Minor axis (Anterior-posterior)			Major axis (Lateral)			Area (mm ²)
	(2b) ₁ (mm)	(2b) ₂ (mm)	(2b) ₃ (mm)	(2a) ₁ (mm)	(2a) ₂ (mm)	(2a) ₃ (mm)	
POR05-S01	6.26	6.27	6.34	6.80	6.75	6.75	33.34
POR05-S02	6.21	6.19	6.16	6.69	6.72	6.63	32.44
POR05-S03	6.27	6.14	6.21	6.55	6.63	6.60	32.09
POR05-S04	6.22	6.14	6.27	6.58	6.56	6.62	32.11
POR06-S01	6.18	6.27	6.17	6.73	6.66	6.63	32.51
POR06-S02	6.26	6.31	6.23	6.60	6.64	6.70	32.69
POR06-S03	6.16	6.25	6.13	6.65	6.63	6.69	32.29
POR06-S04	6.32	6.37	6.34	6.79	6.69	6.64	33.36
Average							32.61
Standard Deviation							0.45

3.1.3 Unconfined Axial Compression Tests

This section presents the several methodological steps used to perform unconfined axial compression tests of the spinal cord samples under stress relaxation conditions.

3.1.3.1 Testing device

Compression tests have been performed in room temperature (37°C) with a uniaxial compression device (Mechanical Tester Model Mach-1 V500CST, Biomomentum, Canada) equipped with a 3.2 mm diameter rigid cylinder to compress the spinal cord. This device is the property of NRC (National Research Council) and is installed in the laboratory at CRCHUM. During the tests, the axial reaction force of the samples was measured with a 17 N load cell (FT 10625) with a precision of 0.85 mN. Force versus time data as well as cylinder displacement were recorded at a frequency of 1 Hz.

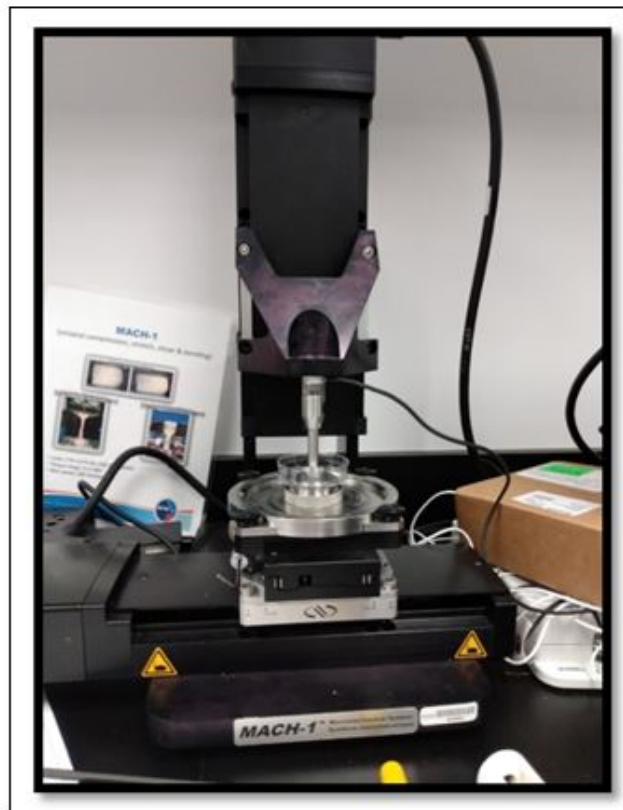


Figure 3.2 Mechanical tester model Mach-1 V500CST

3.1.3.2 Preconditioning

Before starting the compression procedure, the cylinder was positioned a few millimeters above the sample (0.7548 mm). Once the procedure was started, a vertical displacement towards the sample, at a displacement rate (speed) of 0.0225 mm/s, was applied to the cylinder until the load cell detected a force of 0.025 N (Figure 3.3). Reaching this force confirmed contact between the sample and the cylinder impactor (zero displacement).

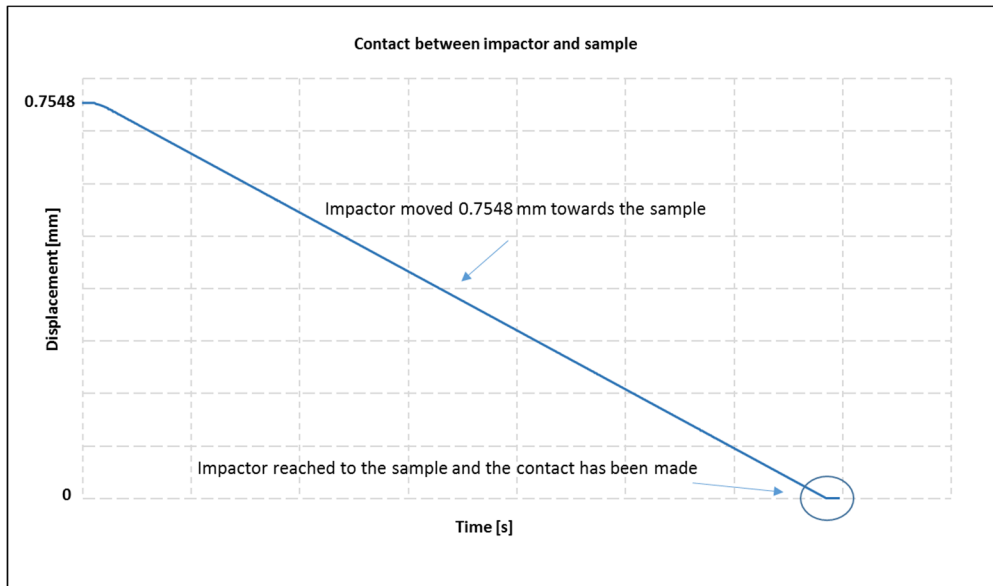


Figure 3.3 Detection of the contact between the cylinder impactor and the sample, at a force of 0.025 N

After reaching contact, a preconditioning of 10 cycles between 5 and 10% compression ramp was carried out for 10 seconds to prevent saturation of the spinal cord tissue (Ramo et al., 2018). The compression was applied at a speed of 0.0225 mm/s, which represents a strain rate of 0.01 s^{-1} . The relation between the speed of the impactor and the strain rate was calculated with Equation (3.3).

$$V = \varepsilon^{\circ} \times l \quad (3.3)$$

where V represents the speed of the impactor, $\dot{\epsilon}$ represents the strain rate and l is the length of the spinal cord sample.

3.1.4 Unconfined compression test

Following preconditioning, the spinal cord was compressed up to 40% of its height (Sparrey & Keaveny, 2011), for an imposed displacement of 0.9 mm, which is 40% of 2.25 mm sample height. This amplitude was chosen to prevent any damage to the spinal cord tissue, thus keeping the spinal cord intact for stress relaxation. The compression was applied using a ramp profile, at a speed of 0.0225 m/s (0.01 s^{-1}). When the full compression was reached, it was maintained for 1000 seconds to allow the sample to relax. After 1000 seconds, a backward ramp at a speed of 5 m/s was applied to move up the impactor at a height of 40 mm above the sample. Throughout the experiments, after locating the specimens on the platen of the mechanical apparatus, PBS was sprayed on the samples once every few minutes to avoid dehydration. The applied relaxation time was determined by fitting different rheological models on preliminary stress-time curves, as described in the next section.

3.1.5 Data analysis

For each specimen, force-time curves were extracted and converted into engineering stress-time curve by dividing the force by the initial area of the sample's cross-section (see Table 3.1). Force-displacement curves were also extracted, and converted into engineering stress-strain curves, up to an engineering strain of 0.4, by dividing the sample's force and elongation by their initial cross-sectional area (see Table 3.1) and initial length (2.25 mm), respectively. Data analysis was done on a HP ProDesk 600 GI TWR with Intel® Core™ i7-4770 CPU @ 3.40 GHz.

3.1.6 Finding relaxation time

To find the appropriate relaxation time to apply experimentally, three rheological models were fitted on a preliminary engineering stress-time relaxation curve using the curve-fitting tool of MATLAB R2018b software, which enables finding the rheological model that offers the best correlation index (R^2) with the experimental curves. The rheological models were the Maxwell model, the two-term generalized Maxwell model and the linear standard Kelvin model. The schematic diagrams and the mathematical definition of each model are shown in Figure 3.4. The stress-time curve of a preliminary test in MATLAB curve-fitting tool in three rheological models are presented in Figure 3.5. Once a good fit was found, the long-term relaxation time was extracted from the model parameters.

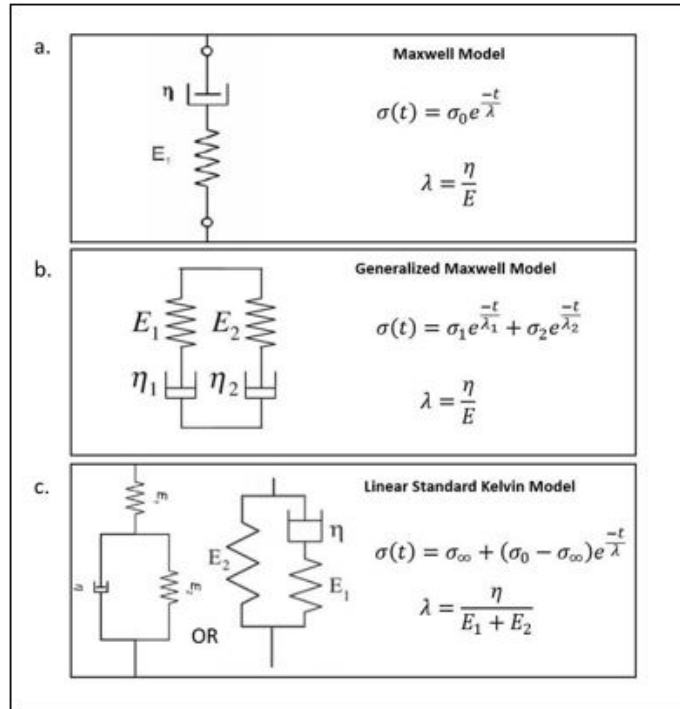


Figure 3.4 Schematic diagrams and mathematical definition of three rheological models. a) Maxwell model b) Generalized Maxwell Model c) Linear Standard Kelvin Model

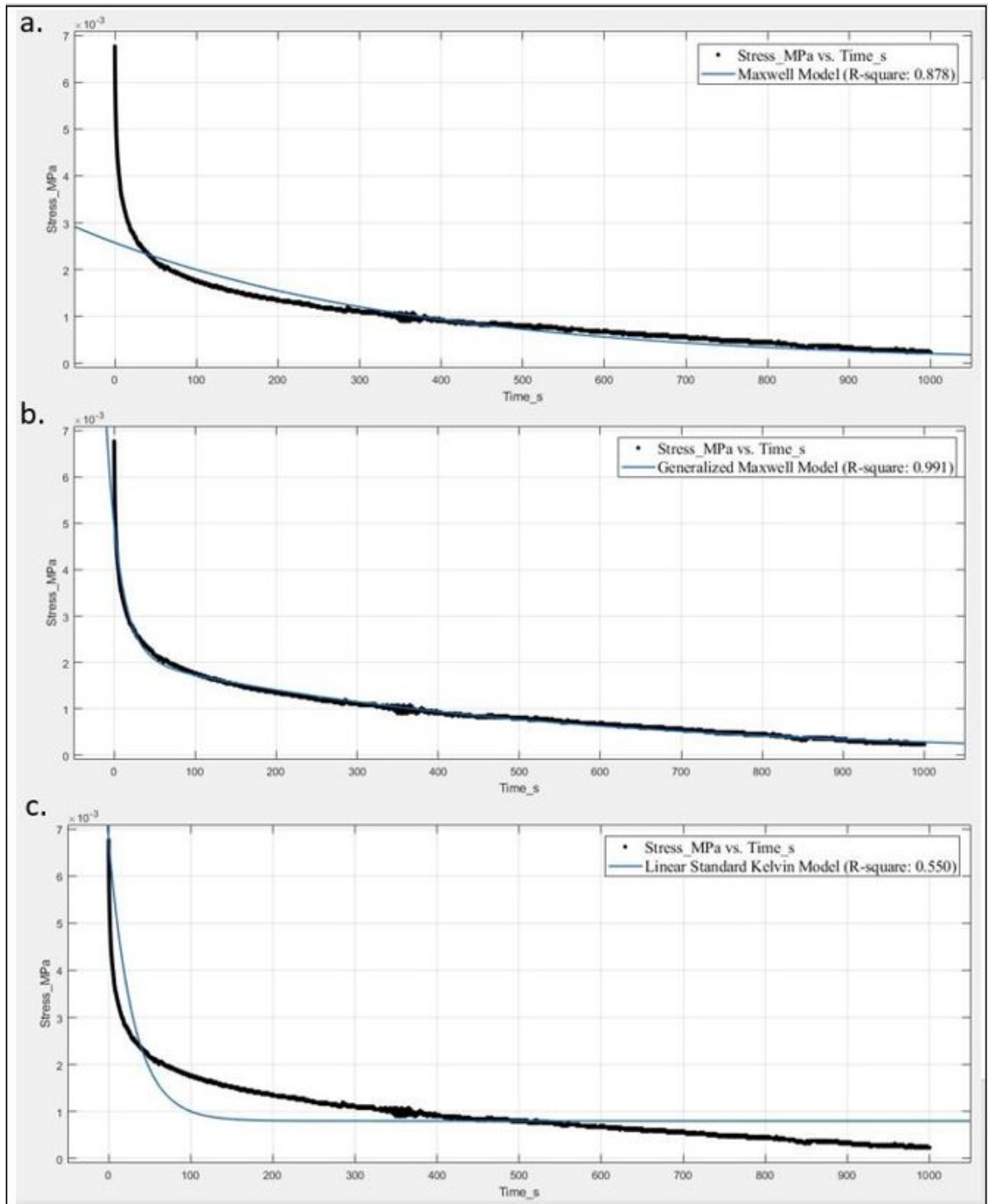


Figure 3.5 Stress-time diagram of a preliminary test with MATLAB curve-fitting tool in three rheological models. a) Maxwell model, $R^2 = 0.878$ b) Generalized Maxwell Model, $R^2 = 0.991$ c) Linear Standard Kelvin Model, $R^2 = 0.550$

The two-terms generalized Maxwell model, containing twice the simple Maxwell form in parallel, provided the best correspondence with the behavior measured experimentally ($R^2 = 0.991$, $RMSE=170.8$) . In MATLAB R2018b, the two-terms generalized Maxwell model is expressed by Equation (3.3):

$$y(x) = Ae^{Bx} + Ce^{Dx} \quad (3.3)$$

Hence, to find the long-term relaxation time, a correspondence between the coefficients A, B, C, D and the physical parameters of the generalized Maxwell model had to be found. This correspondence, described in Table 3.2, shows that long-term relaxation (λ_2) is obtained by dividing -1 by D. By applying this procedure to four preliminary curves, the best fit for long-term relaxation time was found to be 996 ± 62 seconds.

Table 3.2 Generalized Maxwell parameters and the correlated constants in MATLAB

MATLAB parameters	Generalized Maxwell parameters
A	σ_1
B	$\frac{-1}{\lambda_1}$
C	σ_2
D	$\frac{-1}{\lambda_2}$

To confirm complete relaxation of all samples, the relaxation time procedure (curve fitting in MATLAB software) was computed for all tested specimens, confirming that the eight spinal cord specimens were completely relaxed at the end of the experiments. The relaxation times of each specimen are provided in the Results chapter, section 4.1.

3.2 Finite element model of the spinal cord

This section describes the inverse finite element method (Sharkey, 2018) used to develop the finite element model (FEM) of the porcine spinal cord and to determine its viscoelastic material properties.

3.2.1 Spinal cord geometry

The cross-section geometry of the sample POR06-S02 was selected to create the geometry of the FEM because its cross-sectional area was very close to the average cross-sectional area measured from the eight samples (see Table 3.1), and it has a good general appearance (very clear definition of the grey matter) as opposed to other samples. The boundaries of the white and grey matter of the POR06-S02 were thus reproduced using caliper measurements in the CATIA V5-6R2018 CAD software (Dassault Systemes, Vélizy-Villacoublay, France) and a volume of 2.25 mm thickness was created (Figure 3.6). The pia mater that surrounds the spinal cord was not represented in the model since it offers no or little resistance to axial compression.

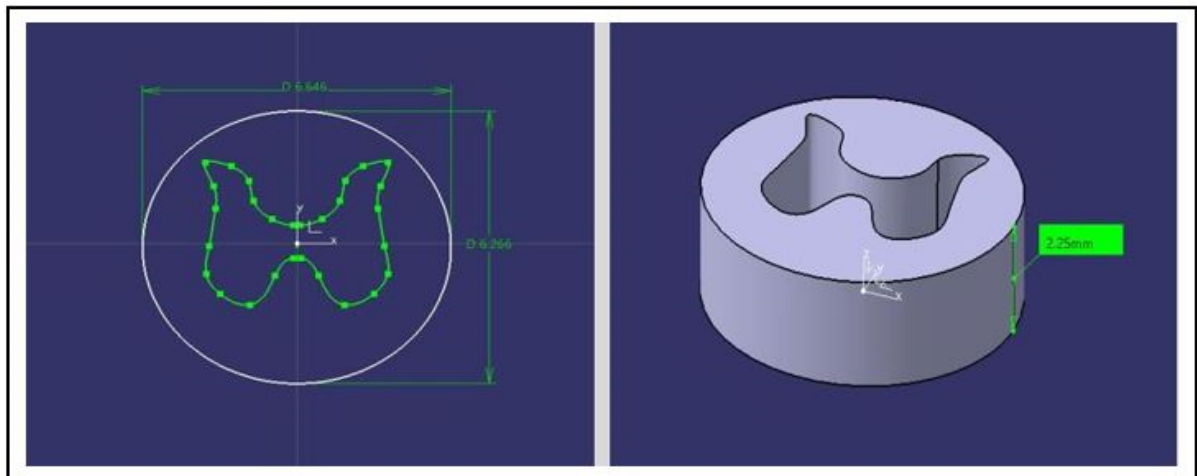



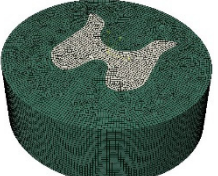



Figure 3.6 Geometry of the sample POR06-S02 in the CATIA software with 6.646 mm lateral axis, 6.266 mm antero-posterior axis, and 2.25mm thickness

3.2.2 Meshing of the FEM

The geometric model was then imported to Abaqus/CAE 2019 software (Dassault Systemes, Johnston, U.S) and 8-node brick-type elements were used to mesh both the white and grey matter volumes. Since mesh size affects the accuracy of the results and the calculation time, a convergence study was performed to find the best compromise between calculation time and results accuracy (Table 3.3). The sizes of the elements were refined among meshes. The mesh with the lowest calculation time and less than 5% variance of peak stress (by comparing one mesh to another) was kept. Material properties, loading and boundary conditions are described in the next subsections. The output used to establish convergence was the total stress lost over time during relaxation. Simulations were run on a HP ProDesk 600 GI TWR with Intel® Core™ i7-4770 CPU @ 3.40 GHz. Based on this study, a mesh size of 0.2 mm was selected, for a total of 13776 nodes and 11275 elements. Results of the convergence study are detailed in the Results chapter, section 4.2.

Table 3.3 Description of the five meshes compared in the convergence study

Mesh	Global seed size (mm)	Number of elements	Number of nodes
1 	0.3	3744	4977
2 	0.2	11275	13776
3 	0.15	25575	29856
4 	0.1	91954	101832
5 	0.08	168280	183135

3.2.3 Interface, loading and boundary conditions

The following interface, loading and boundary conditions were imposed to the FEM in order to mimic the experimental conditions (Figure 3.7):

- A tied interface was defined at the interface between the white and grey matter, so that no relative movement occurs between them;
- The nodes at the bottom surface of the spinal cord FEM were fixed in the axial (z) direction, but allowed to move freely in the xy directions to reproduce the plate beneath the sample during the experiments;
- To simulate the loading cylinder, an axial displacement (-z direction) of 0.9 mm (40% of the height of the spinal cord sample) was applied to the nodes located on the upper surface of the spinal cord FEM. The total displacement was applied at 0.0225 m/s (0.01 s^{-1}) and remained constant for 1000 seconds to let the spinal cord model relax ;
- Given that it is an unconfined compression, the upper surface and the periphery nodes on the outside surface of the spinal cord wall were free to move in x, y and z directions.

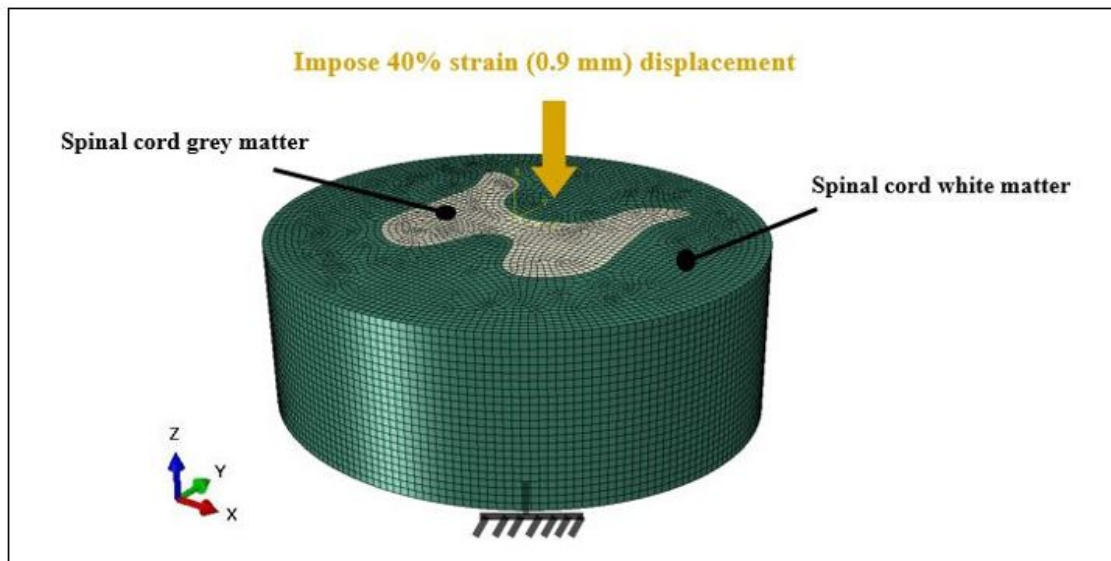


Figure 3.7 FEM interface, loading and boundary conditions

3.2.4 Material properties

To the knowledge of the author, and as disclosed in the literature review, long-term viscoelastic material properties of the white and grey matter for FEM applications are unknown. Accordingly, to perform the convergence study described in section 3.2.2, the white and grey matter were considered as a unique material defined by the average non-linear engineering stress-strain curves (hyperelastic behavior during the loading phase) and the average engineering stress-time curves (stress relaxation behavior) measured experimentally on the eight specimens, up to an engineering strain of 0.4. With the Abaqus/CAE 2019 software (Dassault Systèmes, Johnston, U.S), it was possible to directly insert those curves as material properties with 0.4238 value for Poisson ratio (Ichihara et al., 2001; Li & Dai, 2009; Maikos et al., 2008; Scifert et al., 2002), and find the best material models that fit each curve. A series of hyperelastic material models such as Arruda-Boyce, Mooney Rivlin, Neo Hooke, Ogden ($n=1-3$) and Polynomial models were evaluated for best fitting the compression test results. To evaluate the model, the experimental stress-strain data were imported to the ABAQUS software. The model fitting process showed that a first order Ogden hyperelastic model (Ogden & Hill, 1972) best captured the non-linear response of the complete spinal cord (Figure 3.8). As described in the section 3.1.6, the stress relaxation behavior of the experimental curve was best fitted with the generalized Maxwell model in the MATLAB software. This formulation was not used in the ABAQUS software because it was not available. Instead, a 3-term Prony series was used to capture the viscoelastic behavior of the spinal cord tissue, as proposed by Sparrey and Keaveny (2011). Material models and selected parameters are provided in Table 3.4.

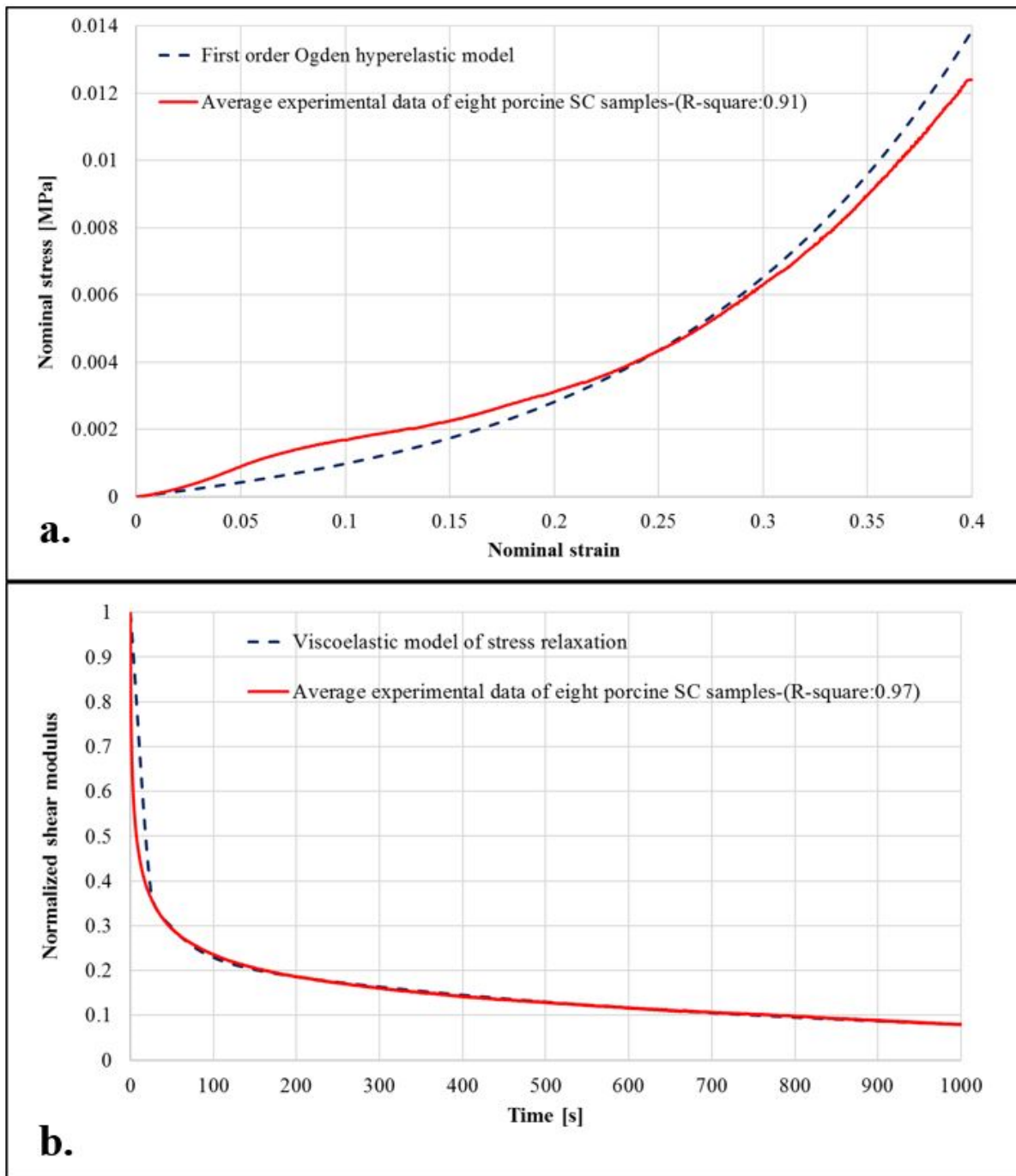


Figure 3.8 Curve fitting of both loading (**a**) and stress relaxation (**b**) behavior averaged from eight spinal cord samples under compression. Experimental data are displayed by solid line and fitted model by dash-lines.

Table 3.4 Material models and selected parameters for the complete spinal cord from the curve fitting process

Ogden Hyperelastic Model			Viscoelastic constitutive model with 3-term Prony series		
$\mu(I)$	$\alpha(I)$	$D(I)$	$G(I)$	$K(I)$	$\tau(I)$
2.625E ⁻³	11.029	198.780	0.489	0.000	2.083
			0.273	0.000	38.343
			0.201	0.000	652.98

Once the mesh size was found (the material properties previously proposed in Table 3.4 were only used for the convergence study), a procedure involving an inverse finite element method was used to determine the distinct material properties of the white and grey matter.

3.2.4.1 White matter material properties

As described in the literature review, the mechanical behavior of the white matter under unconfined compression (loading and relaxation) at different strain rates was characterized by Sparrey and Keaveny (2011). Hence, material properties of the white matter were obtained by fitting material models using Abaqus/CAE 2019 to the experimental loading and stress-relaxation curves of Sparrey and Keaveny (2011) measured at a strain rate of 0.05 s⁻¹ (which is the closest strain rate when compared to our loading condition of 0.01 s⁻¹). This model fitting process showed that a first order Ogden hyperelastic model along with a 3-term Prony series best captured the non-linear and viscoelastic response of the white matter (Figure 3.9). Material model and selected parameters are provided in Table 3.5.

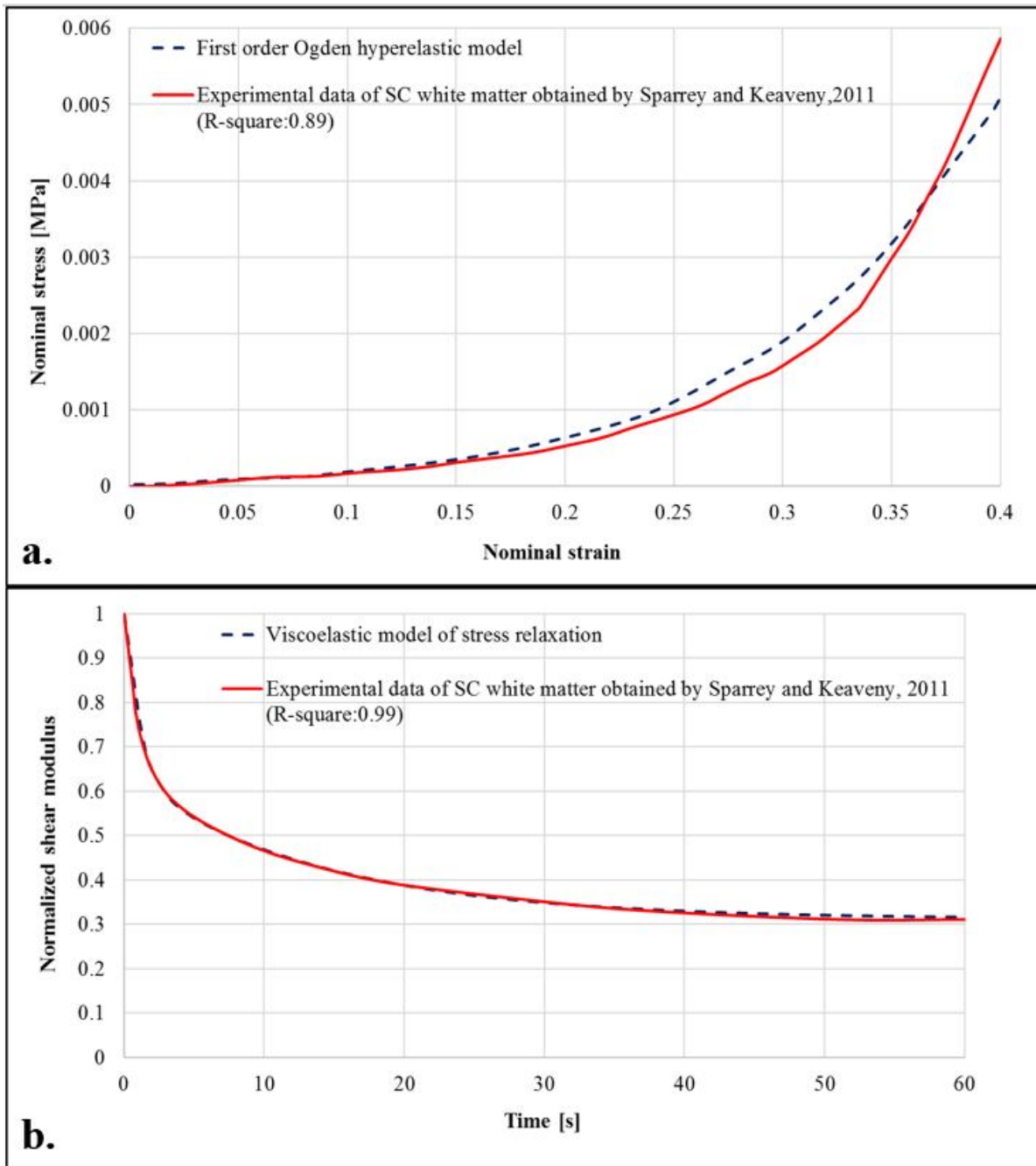


Figure 3.9 Curve fitting of both loading and stress relaxation curves of the white matter measured under compression by Keaveny and Sparrey (2011). Experimental data are displayed by solid line and fitted model by dash-lines.

Table 3.5 White matter material models and parameters from the curve fitting process

Viscoelastic model					
Ogden Hyperelastic Model Coefficients			3-term Prony Series Coefficients		
$\mu(I)$	$\alpha(I)$	$D(I)$	$G(I)$	$K(I)$	$\text{TAU}(I)$
3.947E^{-04}	14.268	0.000	0.368	0.000	1.097
			0.321	0.000	13.930
			0.296	0.000	55.847

To verify that the fitted models were well suited for our FE applications, the experiment of Sparrey and Keaveny (2011) was reproduced numerically. Accordingly, a finite element model of a 3 mm diameter and 1.5 mm length cylinder was created in Abaqus/CAE 2019 to mimic their white matter samples extracted with a biopsy punch (Figure 3.10a). The cylinder was meshed with 8-node hexahedral elements of 0.2 mm characteristic length. The model contains a total of 2385 nodes and 1920 elements. To simulate a compression up to 40% strain, at a strain rate of 0.05 s^{-1} , the top surface nodes were compressed by 0.6 mm at 0.075 mm/s in the -z direction while the bottom nodes were fixed (Figure 3.10b). All the other nodes were free to move in x, y and z directions. Once the full compression was reached, it was maintained for 60 seconds to allow the model to relax.

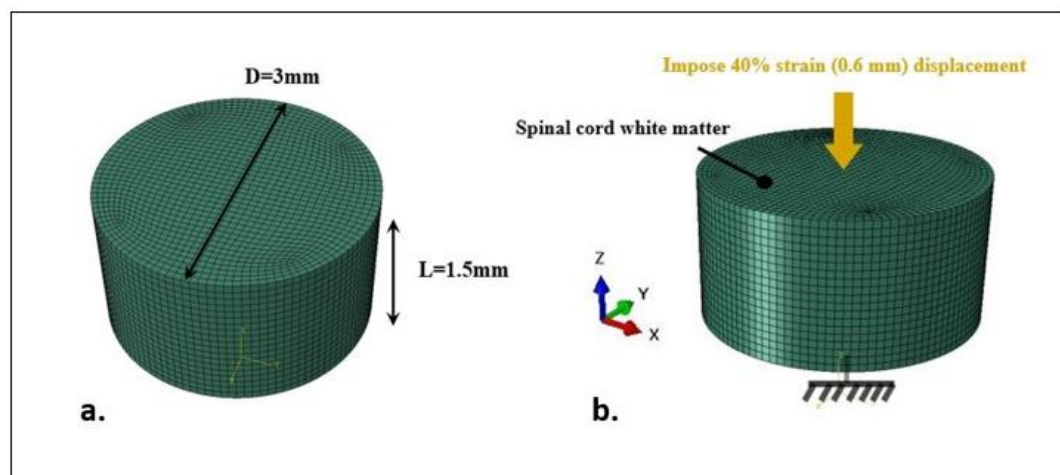


Figure 3.10 FEM of a circular cylinder of white matter used to mimic the experiment of Sparrey and Keaveny (2011)

Comparison of engineering stress showed a good agreement between the finite element model and the experimental curves provided by Sparrey and Keaveny (2011), meaning that no further calibration was needed for the white matter material properties. Results of the verification process are detailed in the Results chapter, section 4.2.

3.2.4.2 Grey matter material properties

With the white matter material properties in hand, it was now possible to obtain the grey matter material properties using an inverse finite element method based on our experimental results on the complete spinal cord. Hence, according to a recent study on porcine spinal cord white and grey matter by Yu et al. (2020) (see section 1.5.3), the spinal cord grey matter is 1.6 to 2 times stiffer than the white matter. Although there is no consensus on the extent of the stiffness of grey matter over white matter, the results of the study of Yu et al. (2020) was chosen as a first proposal. Based on this finding, multiplying the white matter stress-strain data from the study of Sparrey and Keaveny (2011) by 1.6 to 2 would provide the grey matter stress-strain curve. As a first approximation, the white matter relaxation (stress-time) data were not multiplied by any factor and the same data was used as a grey matter relaxation data. After obtaining the initial results, since the FE simulations equilibrium stresses were far from the experimental equilibrium stress, the multiplication factor was applied to relaxation (stress-time) data, as well.

Yu et al. (2020) noted that grey matter samples were contaminated with white matter tissue. This indicates that the stiffness of grey matter is greater than that of the white matter. Therefore, the multiplication factor should be greater than the proposed values of Yu et al. (2002), which was 1.6 to 2. Consequently, to find the proper multiplication factor, simulations on the complete spinal cord were run with the white matter material properties previously found from the study of Sparrey and Keaveny (2011) (Table 3.4), and with grey matter data obtained by applying the multiplication factor to the stress values of the stress-strain and stress-time data of the initial curves of Sparrey and Keaveny (2011). This multiplication factor was first fix to a value of 2, and gradually adjusted (calibrated) with an increment of 0.1 until the peak stress

of the simulated stress-time curve was within 5% of our experimental results curves (loading and stress-relaxation for sample POR06-S02) for the unconfined compression of the complete spinal cord. Afterward, it was possible to derive the material properties of the grey matter by using the same curve fitting process than the one used for the white matter in ABAQUS software. Results of the grey matter calibration and curve fitting process are provided in the Results chapter, section 4.4. This calibration process ensured that our FE model of the spinal cord was well suited for loading and stress relaxation under unconfined compression.

CHAPTER 4

RESULTS

In this chapter, the results obtained in the different steps of the project are presented. Firstly, experimental characterization of the stress relaxation behavior of porcine spinal cord under unconfined compression is presented. Secondly, the results of the mesh convergence analysis are depicted. Finally, results of the FE element calibration process through the definition of the white and grey matter material properties are presented.

4.1 Experimental characterization of the loading and stress relaxation behavior of the porcine spinal cord under unconfined axial compression

Under the imposed displacement, the eight samples present typical force-time curves, with distinct loading and relaxation phases, as illustrated in Figure 4.1.

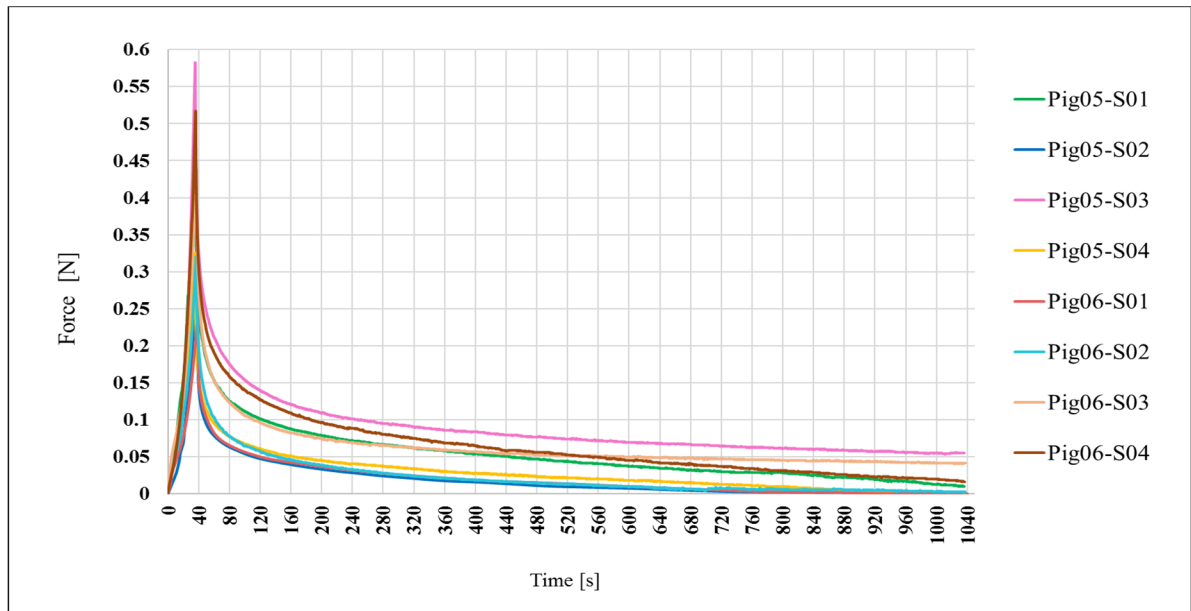


Figure 4.1 Typical force-time response of all samples under unconfined axial compression

The non-linear engineering stress-strain curves of each specimen during the loading phase are depicted in Figure 4.2. All curves show stress-stiffening of the spinal cord samples with increasing strain. The engineering stress ranges from 0.0067 to 0.0182 at an engineering strain of 0.4.

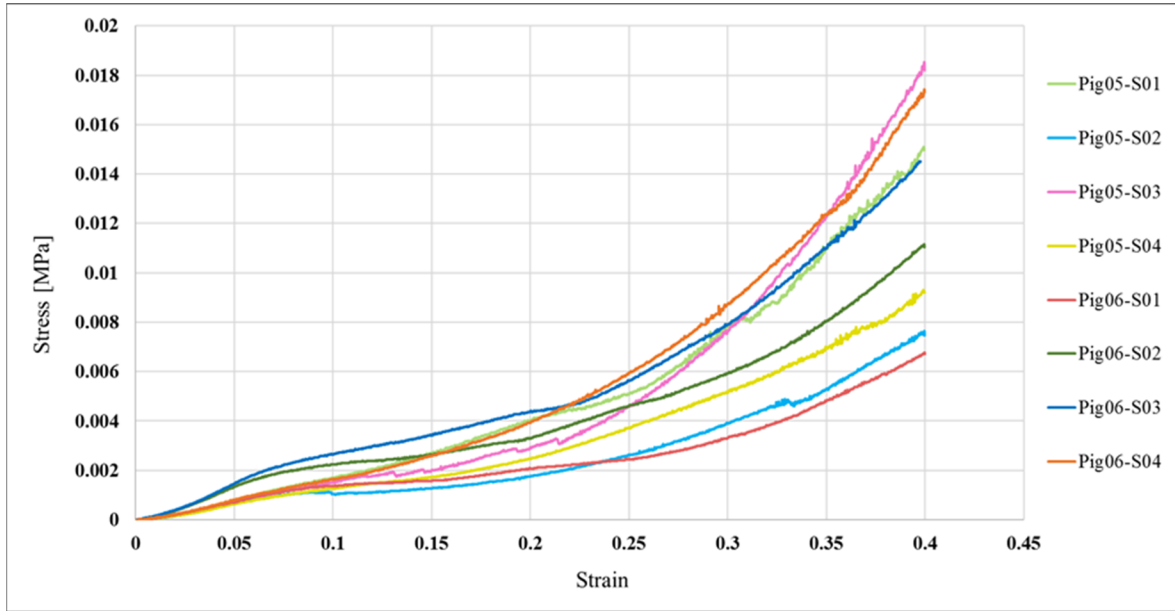


Figure 4.2 Stress-strain response for porcine spinal cord specimens up to a strain of 0.4

To further analyze the stress-relaxation phase, the engineering stress-time curve for this phase was plotted in Figure 4.3. After relaxation, the stress varies from 0.0002 to 0.0022 MPa between samples, with peak stress reduction varying from 87% to 97%. Table 4.1 displays the parameter D obtained by fitting a two-terms generalized Maxwell model on each relaxation stress-time curve, as well as the long-term relaxation time (λ_2) obtained by dividing -1 by D . All fitted curves (not shown) correlate strongly with the experimental curves ($R^2 > 0.98$). Looking at λ_2 in Table 4.1, all samples were relaxed after an average time of 931 ± 96 seconds.

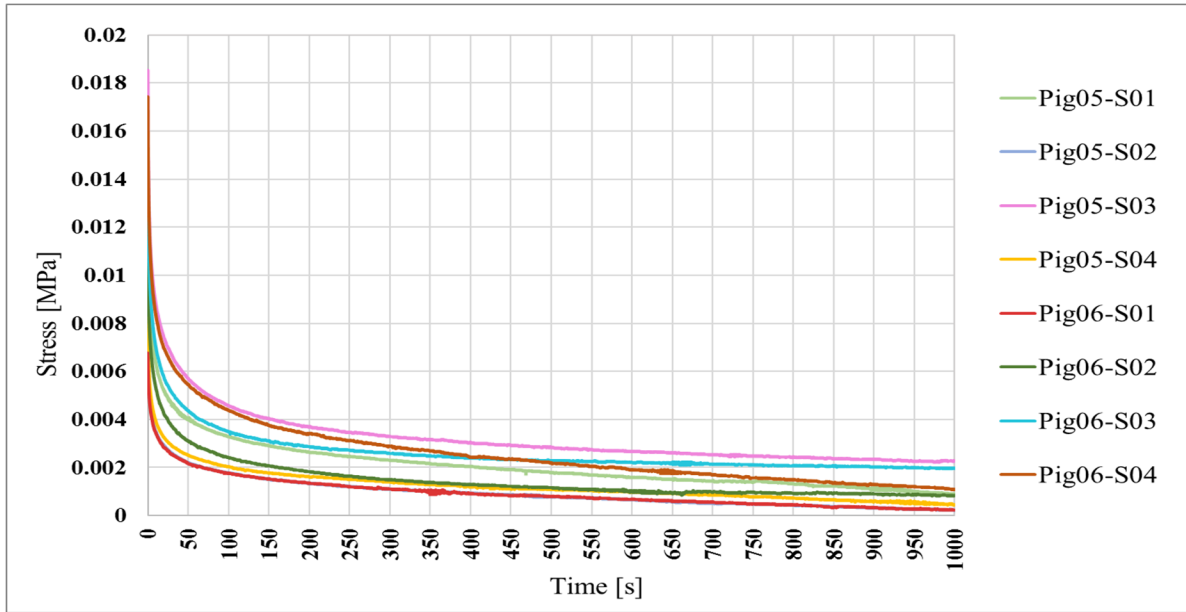


Figure 4.3 Results of the relaxation response of all samples

Table 4.1 Long-term relaxation time (parameter λ_2) obtained by curve fitting a two-terms generalized Maxwell model to the stress-time relaxation curves of each specimen

MATLAB parameters	D	$-\frac{1}{D}$
Generalized Maxwell equivalent	$\frac{-1}{\lambda_2} (s^{-1})$	$\lambda_2 (s)$
POR05-S01	-0.00115	867.30
POR05-S02	-0.00106	946.07
POR05-S03	-0.000920	1087.19
POR05-S04	-0.00118	846.74
POR06-S01	-0.00101	991.08
POR06-S02	-0.00118	851.06
POR06-S03	-0.000963	1038.75
POR06-S04	-0.00122	821.69
Average		931.21
Standard Deviation		93.06

Figure 4.4 illustrates the average engineering stress-time curve of all samples, as well as the average curve plus/minus one standard deviation and the experimental corridor, build from the minimum and maximum curves. The engineering stress-time curve for sample POR06-S02 is also displayed, as this sample was used for the creation and calibration of the complete spinal cord FEM due its closeness with the average sample size and results.

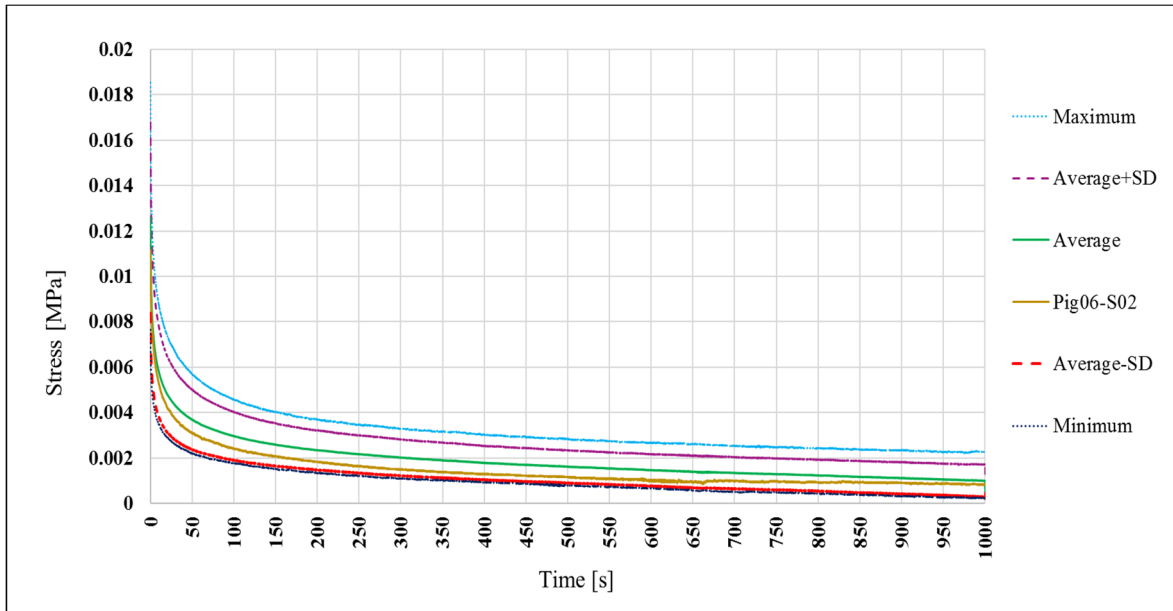


Figure 4.4 Average stress-time curve of all samples for the relaxation phase, as well as the average curve plus/minus one standard deviation, the experimental corridor and the curve for sample P06-S02

4.2 Mesh Convergence Analysis

As expected, increasing the number of nodes and elements of the complete spinal cord FEM increases the computational time (Figure 4.5). Mesh 5 had almost 45 times more elements than mesh 1, but a 98 times greater computational time.

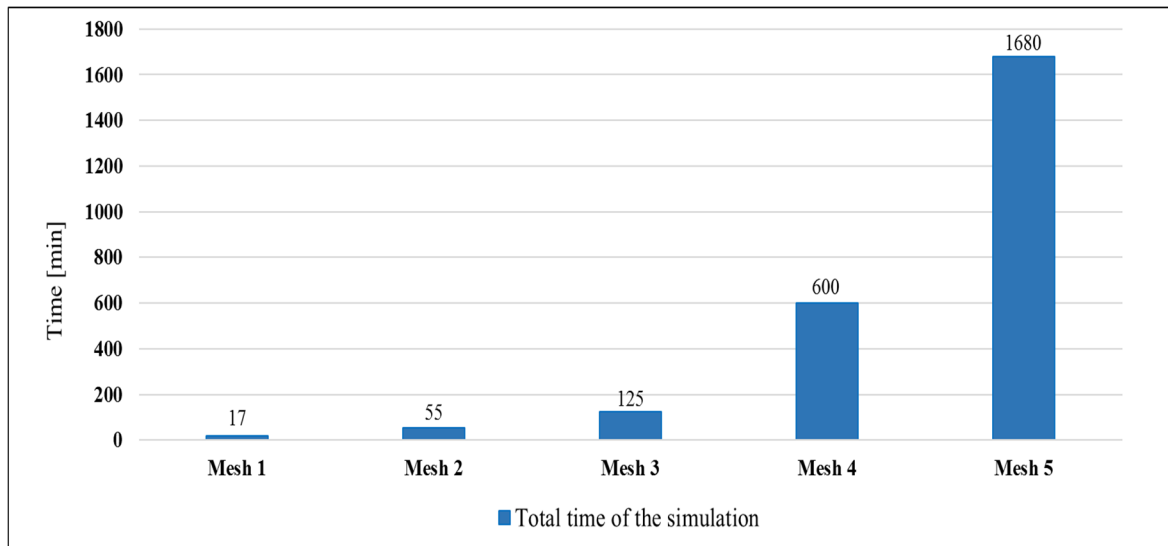


Figure 4.5 Calculation time for the different meshes

Loading and stress relaxation responses as a function of time for the different meshes are illustrated in Figure 4.6. Despite the significant difference in computational time between simulations with different mesh size, the difference in the stress relaxation response between simulations is always less than 5%. Table 4.2 presents total simulation time as well as the maximum stress value for each mesh size. Peak stress value increases by less than 1% between simulations, which further shows that all simulations provide acceptable precision with the same deformed shape. At the end, mesh 2 was selected due to its acceptable computation time, which was less than an hour, and mesh quality (mesh 1 have generated one warning due to element size).

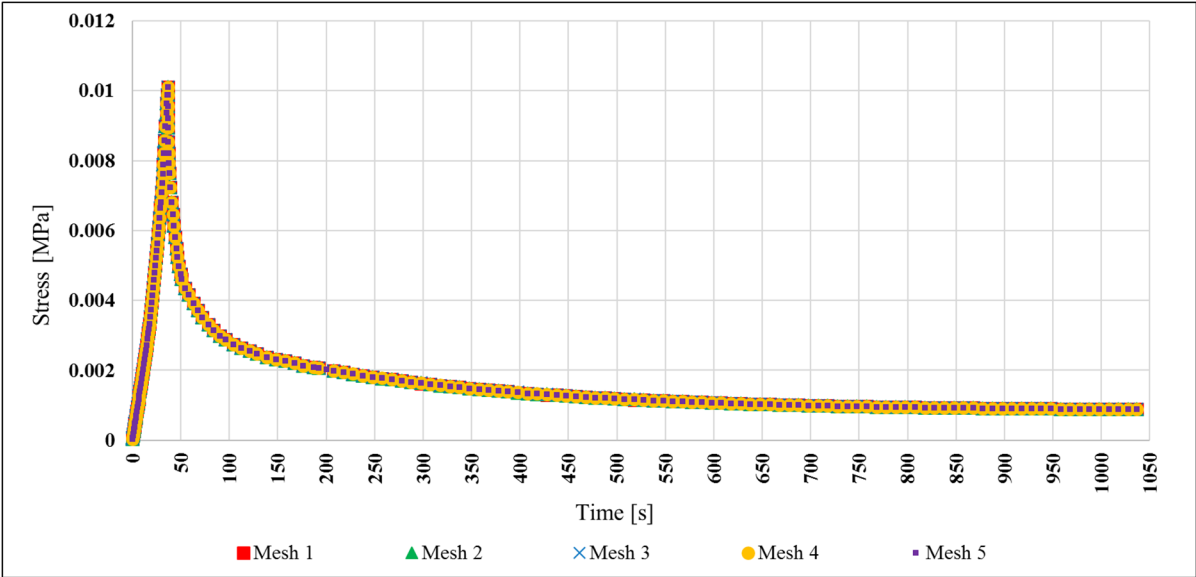


Figure 4.6 Loading and stress relaxation responses for different mesh sizes

Table 4.2 Total simulation time and peak stress values for the 5 different mesh size

Mesh (element size)	Total simulation time (min)	Peak stress (MPa)
1 (0.3 mm)	17	0.010134
2 (0.2 mm)	55	0.010141
3 (0.15 mm)	125	0.010143
4 (0.1 mm)	600	0.010146
5 (0.08 mm)	1680	0.010146
Average		0.010142

4.3 Verification of the white matter material properties

By inserting the material properties derived from the experiment of Sparrey and Keaveny (2011) in the cylindrical white matter FEM, the peak and equilibrium (after relaxation) stress in the model are respectively 6.5% and 10% higher than the stress obtained experimentally by Sparrey and Keaveny, 2011 under similar conditions (Table 4.3). There is also a good agreement between the simulated and the experimental stress-time curves for both loading ($R^2 = 0.99$) and relaxation phases ($R^2 = 0.99$), as shown in Table 4.3 and Figure 4.7.

Table 4.3 Peak and equilibrium stress in the white matter for the FE simulation and the experimental results, and R-square values between their stress-time curves

	Peak stress (MPa)		Equilibrium stress (MPa)		R-square	
Sparrey and Keaveny (2011)	Experiment	FE Simulation	Experiment	FE Simulation	Loading phase	Relaxation phase
	0.0060	0.0064	0.0018	0.0020	0.99	0.99

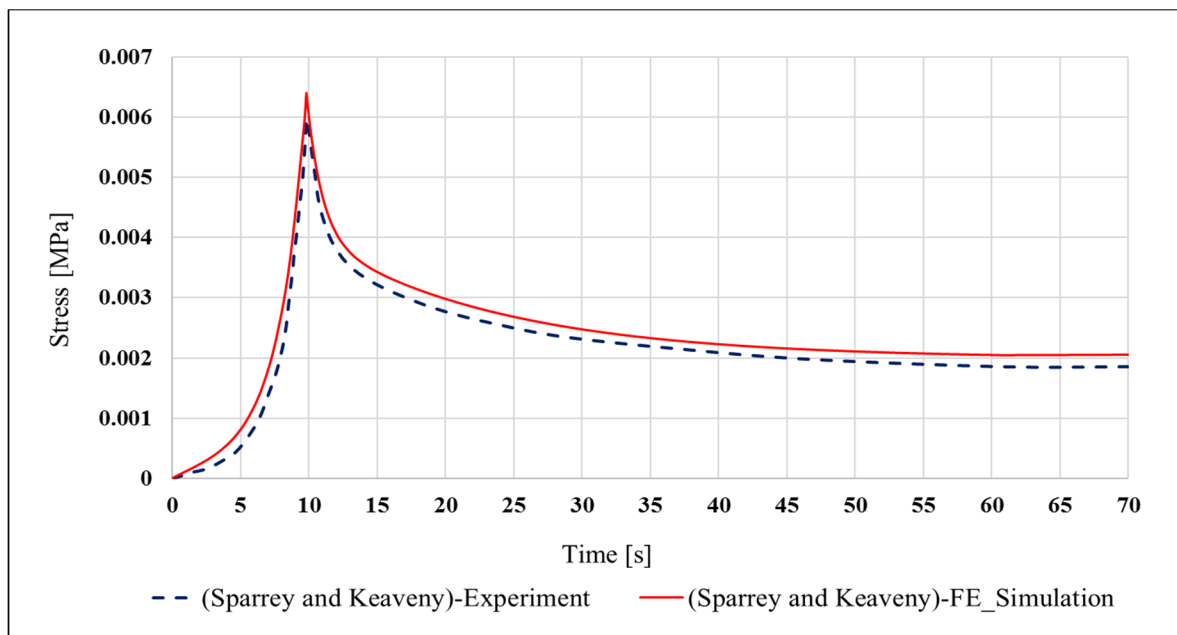


Figure 4.7 Experimental vs FE simulation stress-time data fit of the spinal cord white matter

4.4 Calibration of the grey matter material properties

To obtain the spinal cord grey matter properties, thirteen simulations were run, meaning that the multiplication factor was increased from 2 to 3.2 with an increment of 0.1. The peak stress of the simulation with a multiplication factor of 2 is 25.1% lower than the peak stress of sample POR06-S02, while it is less than 5% lower with a multiplication factor of 3.2. The reason that the multiplication factor of 3.2 is selected and no higher factor was examined is that the difference in peak stress of the simulation (with the multiplication factor of 3.2) and experimental results (POR06-S02) was within 5%. Moreover, the equilibrium stress of all the simulations with multiplication factor of 2 to 3.2 is within 5% of the equilibrium stress of sample POR06-S02. Figure 4.8 compares the stress-time curves for 5 of the 13 simulations with the curve of sample POR06-S02 (over 100 seconds). Table 4.4 detailed the peak stress, equilibrium stress and the R-square values between the simulations and sample POR06-S02, thus showing that the multiplication factor of 3.2 provides good results for the loading and relaxation phase of the curve. Table 4.5 represents the material properties related to the resulting curve with a multiplication factor of 3.2.

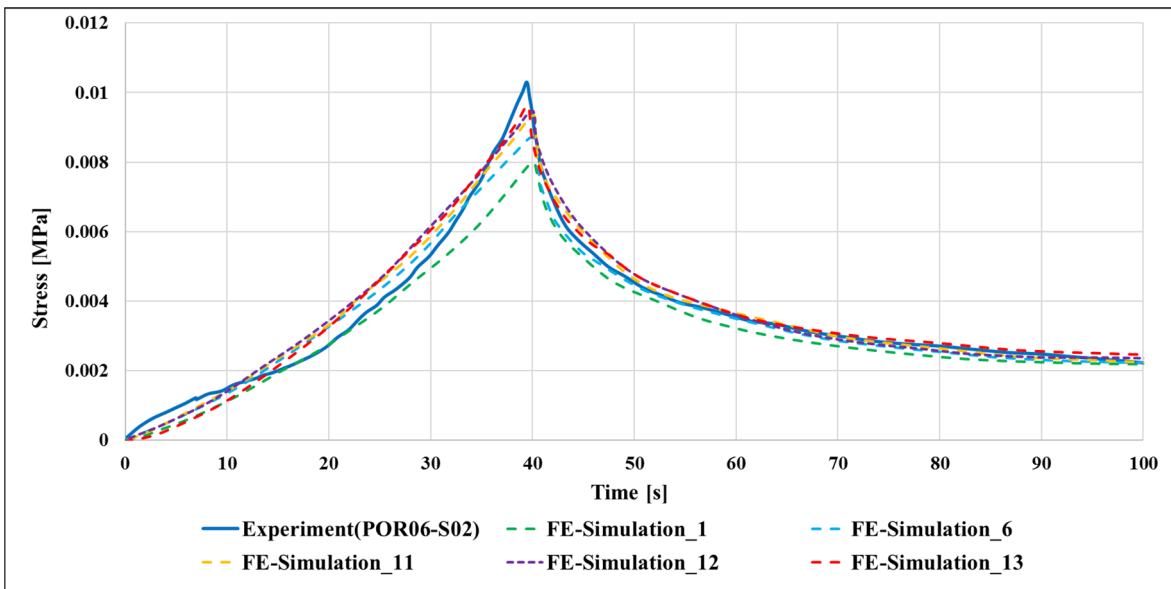


Figure 4.8 Loading and stress relaxation response of the complete spinal cord from five simulations with different multiplication factor for the gray matter properties, and the experimental results of the sample POR06-S02.

Table 4.4 Peak stress of the FEM, and the percentage of differences in peak stress level between the experiment on sample POR06-S02 and 5 of the 13 simulations, as well as the (R^2) value.

Simulation	Material properties		Simulation Peak stress (MPa)	Differences in peak stress between the experiment* and FE simulations (%)	Simulation Equilibrium stress (MPa)	Differences in equilibrium stress between the experiment** and FE simulations (%)	R-Square	
	White matter	Grey matter = white matter experimental data multiply by					Loading phase	Relaxation phase
1	Sparrey and Keaveny, 2011	2	0.0080	25.14	0.00218	1.68	0.97	0.99
6	Sparrey and Keaveny, 2011	2.5	0.0087	16.84	0.00223	0.5	0.98	0.99
11	Sparrey and Keaveny, 2011	3	0.0093	10.20	0.00224	1	0.97	0.99
12	Sparrey and Keaveny, 2011	3.1	0.0096	7.03	0.00231	4.34	0.98	0.98
13	Sparrey and Keaveny, 2011	3.2	0.0098	4.97	0.00232	4.77	0.98	0.98

* The experimental peak stress is 0.0103 MPa.

** The experimental equilibrium stress is 0.0022 MPa.

Table 4.5 White and grey matter material models and parameters from the curve fitting process

	Ogden Hyperelastic Model Coefficients			3-term Prony Series Coefficients		
	$\mu(I)$	$\alpha(I)$	$D(I)$	$G(I)$	$K(I)$	$TAU(I)$
White matter (Sparrey and Keaveny,2011)	3.947E ⁻⁰⁴	14.268	0.000	0.368	0.000	1.097
				0.321	0.000	13.930
				0.296	0.000	55.847
Grey matter (With multiplication factor of 3.2)	2.391E ⁻⁰³	10.613	0.000	0.148	0.000	0.600
				0.509	0.000	8.459
				0.341	0.000	27.772

CHAPTER 5

DISCUSSION

Compressive loading is one of the main loading sustains daily by the spinal cord. Very little experimental data is currently available on the viscoelastic mechanical properties of the spinal cord under compression, mainly due to the challenges in securing, preparing and testing spinal cord tissue samples. Accordingly, the viscoelastic behavior of the spinal cord hasn't been implemented into finite element model of the spinal cord, thus limiting their ability to provide insight into its normal, pathophysiological and per/post-trauma behavior. The strength of this study lies in the characterization of the long-term relaxation behavior of the spinal cord under unconfined compression and the development of a validated FEM that simulate its hyper-viscoelastic behavior. From the FEM, it was possible to derive the quasi-static material properties of the grey matter, which are particularly complex to obtain experimentally. This chapter further discusses these important findings, as well as the limitations of the work accomplished.

5.1 Stress-relaxation behavior of the spinal cord under unconfined axial compression

In this study, experimental results showed that the spinal cord displays a hyperelastic non-linear stress-strain response under unconfined quasi-static compression, and exhibits stress stiffening as the strain increases. This behavior is characteristic of the spinal cord white and grey matter, as observed by many authors (Ichihara et al., 2003; Ichihara et al., 2001; Jannesar et al., 2018; Sparrey & Keaveny, 2011).

The distinction between the white and grey matter material properties is a contentious issue. Results of this study illustrate that the grey matter is almost 3.2 times stiffer than the white matter, bringing additional proofs of the heterogeneity of the spinal cord. Current findings are consistent with many studies, who find out that the spinal cord grey matter was 1.6-2.3 times stiffer than the white matter using tensile tests on bovine cervical spinal cord (Ichihara et al.,

2001), indentation experiments on mouse (Koser et al., 2015), and confined compression on thoracic and cervical regions of porcine spinal cord (Yu et al., 2020). Our finding disagrees with a study on rat spinal cord that showed the shear modulus of the white matter was greater than grey matter (Sharkey, 2018). Sharkey, 2018 found white matter to be two times stiffer than grey matter, while quantifying the in-vivo mechanical properties of rat cervical spinal cord. Ozawa et al. (2001) also found no significant differences between the spinal cord components material properties excised from Japanese rabbits measured in situ by using a pipette aspiration method (Ozawa et al., 2001). This finding was most probably due to the low strain used in their experiments.

The difference between the spinal cord white and grey matter material properties can be explained by their respective cellular components. Histologically, it has been observed that grey matter has larger density of cell bodies in comparison to white matter. In addition, grey matter owns neural cell bodies while white matter does not (Yu, 2019). Grey matter contains relatively few myelinated axons while white matter is composed chiefly of long-range myelinated axons. According to Koser et al. (2015), an increase in the number of cells is directly linked to an increase stiffness. These findings support the difference we found in the compressive material properties of the white and grey matter, whereas the grey matter was substantially stiffer than the white matter.

According to the literature, spinal cord material properties are strain rate dependent. Strain rate has effect on material modulus, which by increasing the strain rate material stiffness increases (Clarke, 2011; Sparrey & Keaveny, 2011). In the current study, the strain rate used is 0.01/s, which is lower than that used in the study of Sparrey and Keaveny (2011) (strain rate 0.05/s). Moreover, due to the differences in the simulation process and the use of different softwares, the material parameters and laws provided by Sparrey and Keaveny (2011), are not used in this study. Therefore, to obtain white matter material properties, the experimental curve with 0.05/s strain rate and 60 seconds relaxation time was reproduced from the study of Sparrey and Keaveny (2011) to enable to extract the stress-time data.

During the current study's experiments, which have been performed in in-vitro condition, non-linear viscoelastic behavior has been observed in the spinal cord tissue. This is the characteristic of the tissue in both in-vitro and in-vivo conditions (Bilston & Thibault, 1995; Clarke et al., 2009; Fiford & Bilston, 2005; Ramo et al., 2018; Shetye et al., 2014b).

In this study, only an axial compression was applied to the spinal cord. Although some studies found that there is no differences in the mechanical properties of the grey matter tissue in different directions (Koser et al., 2015; Ozawa et al., 2001; Yu et al., 2020), there is also significant evidence that suggest that the spinal cord components are anisotropic and asymmetric (Ozawa et al., 2001; Yu et al., 2020). Hence, the material properties provided in this study should be only used to investigate the behavior of the spinal cord under axial compression.

By showing immediate stress relaxation under a constant strain, the viscoelastic behavior of the spinal cord samples was consistent with other studies (Clarke, 2011; Shetye et al., 2014a; Sparrey & Keaveny, 2011; Yu et al., 2020). The near zero equilibrium stress reached (average of 0.00046 MPa) was consistent with the study of Yu et al., 2020. Equilibrium stress is lower in current study than in the study of Yu et al (2020), who measured equilibrium stress of 0.006 and 0.009 MPa on the white and grey matter, respectively. This was expected since Yu et al. (2020) tested the spinal cord components under confined compression, a condition where the fluid is trapped within the spinal cord during compression, thus creating higher stresses within the material. Moreover, according to many authors (Clarke, 2011; Ramo et al., 2018; Shetye et al., 2014b; Sparrey & Keaveny, 2011), the equilibrium stress of the spinal cord components depends on both the compressive strain and strain rate. This further reemphasize the effect of the experimental setup and loading conditions when testing the spinal cord.

In this study, it has been measured that spinal cord fully relaxes after almost 931 seconds, which provides new information about the long-term stress relaxation of the spinal cord. In the study of Sparrey and Keaveny (2011), relaxation time of the white matter was only 60 seconds. Moreover, in the study of Yu et al. (2020), relaxation time of the grey matter and white matter

were only measured for 100 and 40 seconds, respectively, assuming that the grey matter had longer relaxation time, mostly due to different tissue permeability. In a study of Kaczmarek et al. on brain tissue, white matter assumed to be more permeable than grey matter (Kaczmarek et al., 1997). In addition, in a study on cartilage, it was demonstrated that increase permeability leads to faster relaxation up to equilibrium, whereas decreased resistance to fluid flow enhances fluid redistribution inside the tissue (Lai et al., 1981). The spinal cord is composed of solid and fluid phase. It in fact is a porous biphasic formation. By compressing the spinal cord, the interstitial fluid flow spreads into the porous permeable solid matrix. As the compression continues, the pores fill with fluid and permeability decreases. Thereupon, for tissue compression, higher stress is required (Cheng & Bilston, 2007; Haslach et al., 2014; Lai et al., 1981). Throughout the relaxation phase, the compaction of solid matrix is retained, and gradually, fluid redistribution inside the tissue occurs to reach to an equilibrium stress (Mow et al., 1980).

The reported peak stress level for the average of all specimens was 0.012 MPa, which is significantly higher than the peak stress obtained by Jannesar et al., 2016 that measured 0.001 MPa peak stress for the spinal cord white matter of non-human primate specimens with 1.5 mm height, using 40% strain and 0.05/s strain rate in unconfined compression (Jannesar et al., 2016). In the study of Sparrey and Keaveny (2011) on porcine spinal cord white matter specimens with 1.5 mm height, the peak stress level was reported approximately 0.006 MPa for the strain rate of 0.05/s. This study used 40% strain in unconfined compression. Due to the differences in peak stress values in these two studies, which are lower than the peak stress measured in the current approach, the absence of grey matter in the study of Jannesar et al. (2016) and Sparrey and Keaveny (2011) is the most notable factor in this difference. In addition, the differences in the type of the samples (non-human primates versus porcine) can be mentioned to explain the difference between the peak stresses of the two studies.

To limit the effect of post-mortem time on the behavior of the spinal cord, all specimens were tested within 6 hours after euthanasia, from spinal cord extraction to testing. This was consistent with other stress-relaxation studies performed on spinal cord (Yu et al., 2020) and

brain components (Garo et al., 2007; Yu et al., 2020). On the other hand, this time limit is inconsistent with other studies (Chang et al., 1988; Hung & Chang, 1981; Oakland et al., 2006; Ramo et al., 2018), who saw significant increases in tissue stiffness in less than 6 hours. According to the results of Chang et al. (1998), even with in situ hydration and temperature for the samples, time post mortem affects the elastic modulus and extent of relaxation in tissues. For instance, despite the same hydration condition, (Hung & Chang, 1981) observed a 22% increase in the elastic modulus of their spinal cord samples one-hour after sacrifice.

5.2 Finite element modeling of the spinal cord

Using an inverse finite element method, distinct mechanical properties were found for the white and grey matter under quasi-static compression, for both loading and stress-relaxation phases. The most common assumption for computational modeling often includes a homogenous spinal cord, which displays the same material properties for the white and grey matter. Significant differences in the white and grey matter stiffness must be highlighted as it would create inhomogeneous stress in the cross-section of the spinal cord under pure axial compression (Yu, 2019). The finite element analysis of Nishida et al. (2016), who modeled the spinal cord with stiffer grey matter than white matter, supports this discrepancy between the spinal cord components (Nishida et al., 2016). Moreover, in a finite element analysis on the rat spinal cord, Maikos et al., 2008 used a grey matter that was 20% stiffer than white matter. They demonstrate that the grey matter witnessed a higher stress than the white matter. In addition, it was shown that by increasing the stiffness of the grey matter, strain decreases (Maikos et al., 2008). Jannesar et al. (2016) compared the strain amount of the spinal cord white and grey matter at the injury epicenter. They showed that white matter experienced more strain than grey matter within the cross section of the spinal cord (Jannesar et al., 2016).

After calibration of the grey matter material properties, the FEM of the spinal cord was in good agreement with the experimental results obtained in similar conditions for both loading and stress relaxation phases. The peak stress level in the FEM was about 4.97% lower than that obtained experimentally. Equilibrium stress in the model was about 4.77% higher than

experiment. Accordingly, the use of a non-linear first order Ogden hyperelastic combined with 3-term Prony series to reproduce the behavior of the grey and white matter was proved to be appropriate. Similar formulations were used by Sparrey and Keaveany (2011) to represent the viscoelastic response of the white matter, but with different parameters since their exact formulations in MATLAB software were not available in the ABAQUS software.

5.3 Limitations

There are limitations in this study, including experimental and computational limits, which will be briefly explained here:

- The complexity of the spinal cord tissue is experimentally challenging. Due to the excessive softness of the spinal cord tissue, cutting the specimens to the desired length of 2.25 mm was very difficult and caused the loss of some specimens. Therefore, the number of samples obtained for the experiments was reduced. More pigs would have been required, but only a small number were available for the experiments ;
- Cutting samples with parallel surfaces is important to avoid bending in addition to compression. Even if the cutting process was performed with a cross-section cutting cradle and two sharp laser blades, and that the parallel surfaces were visually confirmed, it is possible that the measured behavior contained some bending. The more uniform and parallel are the cutting surfaces, better is the contact with the upper and lower mechanical device platens and better is the distribution of force ;
- Although the friction between the samples and the top and bottom platens were reduced by lubricating the surfaces, the assumption of frictionless contact between the spinal cord samples and platens is another limitation of the study ;
- All experiments have been performed in in-vitro condition. As different mechanical properties were observed between *in vitro* and *ex vivo* samples, experiments should be performed under *ex vivo* condition, thus providing more accurate results ;
- The stress relaxation behavior of the spinal cord was characterized for a complete spinal cord segment. Since the spinal cord is made up of two components, the white and grey

matter, characterization of the behavior of each component separately could provide different results, especially for the grey matter material properties, which were here obtain using a computational method ;

- In this study, the spinal cord stress-strain and stress-time behavior was defined under a compressive loading. Considering that the spinal cord is an anisotropic and strain rate dependent material, future works should involve an extensive characterization of the spinal cord hyper-viscoelastic properties in other loading directions, at other strain rate. Moreover, the use of an unconfined test might not be perfectly representative of the real in vivo conditions, as the spinal cord is surrounded by the cerebrospinal fluid, the meninges and the spinal canal ;
- The use of porcine specimens to evaluate the spinal cord behavior to study the biomechanics of the spinal cord is generally accepted in the scientific community due to its similarity with the anatomy of the human spinal cord. However, to draw final conclusions, human cadavers have to be tested ;
- The geometry of the model was obtained using a specimen close to the average dimensions of all specimens, and unlike the spinal cord, the model lacks the pia matter; therefore, the model represents an estimation of the behavior of a spinal cord. Given that the size of the spinal cord increases as it descends within the spinal column, adapting the geometry of the model to the level at which specimen is located and add pia matter to the model would be an improvement in this study ;
- In the current study, tissue were compressed using a strain rate of 0.01/sec, which does not cover the range of velocity observed in spinal cord injury. Experimental models of SCI have utilized velocity of more than 3 mm/s to identify the effect of velocity (Sparrey et al., 2008). However, the model developed in this study can be adapted to predict the spinal cord mechanical behavior at faster strain rate.

CONCLUSION

In this study, the characterization of the long-term relaxation behavior of the spinal cord under unconfined axial compression and the development of a FEM that accurately reproduces such behavior was achieved. From the FEM, it was possible to derive the quasi-static material properties of the grey matter, which are particularly complex to obtain experimentally. The proposed objectives of this research project have been met in the following ways:

- **Objective 1:** An experimental approach has been developed to investigate the mechanical behavior of the spinal cord in axial unconfined compression. Specimens collected from porcine spinal cord were located in a mechanical apparatus and a quasi-static compression was applied and maintained for 1000 seconds after reaching a strain of 0.4, thus allowing investigation of the long-term relaxation response of the spinal cord.
- **Objective 2:** A finite element model of the spinal cord, including the white and grey matter components and incorporating first order Ogden hyperelastic material models combined with 3-terms Prony series to represent both materials, was developed. The model was calibrated using the experiments of objective 1 and a very good agreement between the simulation and the experiments was achieved. The model showed that the grey and white matter have similar behavior, but different material properties, the grey matter being stiffer than the white matter.

Through the work carried out, it has been shown that the isotropic viscoelastic laws of the ABAQUS software can be used to represent the stress relaxation behavior of the spinal cord tissue. Current study concluded that the heterogeneity of the spinal cord has to be considered, while using computational modeling to study the biomechanics of spinal cord injury. In order to properly model the correlation between the impact of the spinal cord and the result of tissue damage, the material properties of the spinal cord have to be thoroughly studied. By

understanding the spinal cord material properties and conditions of the normal and damaged tissue, the most effective therapy for spinal cord injury can be identified.

BIBLIOGRAPHY

- Abdel-Aziz, K., & Ciccarelli, O. (2014). Chapter 1.1 - Rationale for Quantitative MRI of the Human Spinal Cord and Clinical Applications. In J. Cohen-Adad & C. A. M. Wheeler-Kingshott (Eds.), *Quantitative MRI of the Spinal Cord* (pp. 3-21). San Diego: Academic Press.
- Acheson, M. B., Livingston, R. R., Richardson, M. L., & Stimac, G. K. (1987). High-resolution CT scanning in the evaluation of cervical spine fractures: comparison with plain film examinations. *American Journal of Roentgenology*, 148(6), 1179-1185.
doi:10.2214/ajr.148.6.1179
- Ahuja, C. S., Wilson, J. R., Nori, S., Kotter, M. R. N., Druschel, C., Curt, A., & Fehlings, M. G. (2017). Traumatic spinal cord injury. (2056-676X (Electronic)).
- Alizadeh, A., Dyck, S. M., & Karimi-Abdolrezaee, S. (2019). Traumatic Spinal Cord Injury: An Overview of Pathophysiology, Models and Acute Injury Mechanisms. *Frontiers in neurology*, 10, 282-282. doi:10.3389/fneur.2019.00282
- Anatomy of the Spinal Cord. (n.d.). Retrieved from
<https://nba.uth.tmc.edu/neuroscience/m/s2/chapter03.html#>
- Anatomy of the Spine. (2018). Retrieved from <https://mayfieldclinic.com/pe-anat spine.htm>
- Applied anatomy of the lumbar spine. (n.d.). Retrieved from
<https://musculoskeletalkey.com/applied-anatomy-of-the-lumbar-spine/>
- Biga, Sierra Dawson, Amy Harwell, Robin Hopkins, Joel Kaufmann, Mike LeMaster, . . . Runyeon, J. (n.d.). *Anatomy & Physiology*.
- Bilston, L. E., & Thibault, L. E. (1995). The mechanical properties of the human cervical spinal cord In Vitro. *Annals of Biomedical Engineering*, 24(1), 67-74.
doi:10.1007/BF02770996
- Bridwell, M. (2019). Intervertebral Discs. Retrieved from
<https://www.spineuniverse.com/anatomy/intervertebral-discs>
- Budday, S., Nay, R., de Rooij, R., Steinmann, P., Wyrobek, T., Ovaert, T. C., & Kuhl, E. (2015). Mechanical properties of gray and white matter brain tissue by indentation. (1878-0180 (Electronic)).

- Budday, S., Sommer, G., Birkel, C., Langkammer, C., Haybaeck, J., Kohnert, J., . . . Holzapfel, G. A. (2017). Mechanical characterization of human brain tissue. *Acta Biomaterialia*, 48, 319-340. doi:<https://doi.org/10.1016/j.actbio.2016.10.036>
- Carter, J. W. (2002). *Compressive cervical spine injury: the effect of injury mechanism on structural injury pattern and neurologic injury potential*. University of Washington, The Central Nervous System. (n.d.). Retrieved from <https://courses.lumenlearning.com/ap1/chapter/the-central-nervous-system/>
- Chang, G.-L., Hung, T.-K., & Feng, W. W. (1988). An In-Vivo Measurement and Analysis of Viscoelastic Properties of the Spinal Cord of Cats. *Journal of Biomechanical Engineering*, 110(2), 115-122. doi:10.1115/1.3108415
- Chen, He, Y., & DeVivo, M. J. (2016). Changing Demographics and Injury Profile of New Traumatic Spinal Cord Injuries in the United States, 1972-2014. (1532-821X (Electronic)).
- Chen, Liu, J., Assinck, P., Bhatnagar, T., Streijger, F., Zhu, Q., . . . Oxland, T. (2015). Differential Histopathology and Behavioral Outcomes Eight Weeks After Rat Spinal Cord Injury by Contusion, Dislocation, and Distraction Mechanisms. *Journal of Neurotrauma*, 33. doi:10.1089/neu.2015.4218
- Cheng, S., & Bilston, L. E. (2007). Unconfined compression of white matter. (0021-9290 (Print)).
- Cheriyian, Ryan, D., Weinreb, J. H., Cheriyian, J., Paul, J. C., Lafage, V., . . . Errico, T. J. (2014a). Spinal cord injury models: a review. *Spinal Cord*, 52(8), 588-595. doi:10.1038/sc.2014.91
- Cheriyian, Ryan, D. J., Weinreb, J. H., Cheriyian, J., Paul, J. C., Lafage, V., . . . Errico, T. J. (2014b). Spinal cord injury models: a review. *Spinal Cord*, 52(8), 588-595. doi:10.1038/sc.2014.91
- Cho, T. A. (2015). Spinal Cord Functional Anatomy. *CONTINUUM: Lifelong Learning in Neurology*, 21(1).
- Choo, Liu J Fau - Lam, C. K., Lam Ck Fau - Dvorak, M., Dvorak M Fau - Tetzlaff, W., Tetzlaff W Fau - Oxland, T. R., & Oxland, T. R. (2007). Contusion, dislocation, and distraction: primary hemorrhage and membrane permeability in distinct mechanisms of spinal cord injury. (1547-5654 (Print)).
- Choo, Liu, J., Liu, Z., Dvorak, M., Tetzlaff, W., & Oxland, T. R. (2009). Modeling spinal cord contusion, dislocation, and distraction: Characterization of vertebral clamps, injury severities, and node of Ranvier deformations. *Journal of Neuroscience Methods*, 181(1), 6-17. doi:<https://doi.org/10.1016/j.jneumeth.2009.04.007>

- Clarke. (2011). Spinal Cord Mechanical Properties. In L. E. Bilston (Ed.), *Neural Tissue Biomechanics* (pp. 25-40). Berlin, Heidelberg: Springer Berlin Heidelberg.
- Clarke, Cheng, S., & Bilston, L. E. (2009). The mechanical properties of neonatal rat spinal cord in vitro, and comparisons with adult. *Journal of Biomechanics*, 42(10), 1397-1402. doi:<https://doi.org/10.1016/j.jbiomech.2009.04.008>
- Clarke, Choo, A. M., Liu, J., Lam, C. K., Bilston, L. E., Tetzlaff, W., & Oxland, T. R. (2008). Anterior Fracture-Dislocation Is More Severe than Lateral: A Biomechanical and Neuropathological Comparison in Rat Thoracolumbar Spine. *Journal of Neurotrauma*, 25(4), 371-383. doi:10.1089/neu.2007.0421
- Cripps, R. A., Lee Bb Fau - Wing, P., Wing P Fau - Weerts, E., Weerts E Fau - Mackay, J., Mackay J Fau - Brown, D., & Brown, D. (2010). A global map for traumatic spinal cord injury epidemiology: towards a living data repository for injury prevention. (1476-5624 (Electronic)).
- Dermatomes and Myotomes: Upper & Lower Limb. (n.d.). Retrieved from <https://www.howtorelief.com/dermatomes-myotomes-upper-lower-limb/>
- Dimar, J. R., II, Glassman, S. D., Raque, G. H., Zhang, Y. P., & Shields, C. B. (1999). The Influence of Spinal Canal Narrowing and Timing of Decompression on Neurologic Recovery After Spinal Cord Contusion in a Rat Model. *Spine*, 24(16).
- Eisenfeld, J., Mow, V. C., & Lipshitz, H. (1978). Mathematical analysis of stress relaxation in articular cartilage during compression. *Mathematical Biosciences*, 39(1), 97-112. doi:[https://doi.org/10.1016/0025-5564\(78\)90029-9](https://doi.org/10.1016/0025-5564(78)90029-9)
- Feng, Y., Okamoto, R. J., Namani, R., Genin, G. M., & Bayly, P. V. (2013). Measurements of mechanical anisotropy in brain tissue and implications for transversely isotropic material models of white matter. *Journal of the Mechanical Behavior of Biomedical Materials*, 23, 117-132. doi:<https://doi.org/10.1016/j.jmbbm.2013.04.007>
- Fields, Araque, A., Johansen-Berg, H., Lim, S.-S., Lynch, G., Nave, K.-A., . . . Wake, H. (2014). Glial biology in learning and cognition. *The Neuroscientist : a review journal bringing neurobiology, neurology and psychiatry*, 20(5), 426-431. doi:10.1177/1073858413504465
- Fiford, & Bilston, L. E. (2005). The mechanical properties of rat spinal cord in vitro. *Journal of Biomechanics*, 38(7), 1509-1515. doi:<https://doi.org/10.1016/j.jbiomech.2004.07.009>
- Fiford, Bilston, L. E., Waite, P., & Lu, J. (2004). A Vertebral Dislocation Model of Spinal Cord Injury in Rats. *Journal of Neurotrauma*, 21(4), 451-458. doi:10.1089/089771504323004593

- Fournely, M., Petit, Y., Wagnac, E., Evin, M., & Arnoux, P.-J. (2020). Effect of experimental, morphological and mechanical factors on the murine spinal cord subjected to transverse contusion: A finite element study. *PLOS ONE*, 15(5), e0232975. doi:10.1371/journal.pone.0232975
- Fradet, L., Cliche, F., Petit, Y., Mac-Thiong, J. M., & Arnoux, P. J. (2016). Strain rate dependent behavior of the porcine spinal cord under transverse dynamic compression. (2041-3033 (Electronic)).
- Frank, C. B. (2004). Ligament structure, physiology and function. *Journal of Musculoskeletal and Neuronal Interactions*, 4(2), 199.
- Fredø, H. L., Rizvi Sa Fau - Lied, B., Lied B Fau - Rønning, P., Rønning P Fau - Helseth, E., & Helseth, E. (2012). The epidemiology of traumatic cervical spine fractures: a prospective population study from Norway. (1757-7241 (Electronic)).
- Garo, A., Hrapko M Fau - van Dommelen, J. A. W., van Dommelen Ja Fau - Peters, G. W. M., & Peters, G. W. (2007). Towards a reliable characterisation of the mechanical behaviour of brain tissue: The effects of post-mortem time and sample preparation. (0006-355X (Print)).
- Geris, L. (2013). *Computational modeling in tissue engineering*. In Studies in mechanobiology, tissue engineering and biomaterials, 1868-2006 ; v. 10. Retrieved from <http://public.eblib.com/choice/publicfullrecord.aspx?p=1082573> doi:10.1007/978-3-642-32563-2
- Haslach, H. W., Leahy, L. N., Riley, P., Gullapalli, R., Xu, S., & Hsieh, A. H. (2014). Solid–extracellular fluid interaction and damage in the mechanical response of rat brain tissue under confined compression. *Journal of the Mechanical Behavior of Biomedical Materials*, 29, 138-150. doi:<https://doi.org/10.1016/j.jmbbm.2013.08.027>
- Highsmith. (2020). Spinal Anatomy Center. Retrieved from <https://www.spineuniverse.com/anatomy>
- Hung, T.-K., & Chang, G.-L. (1981). Biomechanical and Neurological Response of the Spinal Cord of a Puppy to Uniaxial Tension. *Journal of Biomechanical Engineering*, 103(1), 43-47. doi:10.1115/1.3138244
- Ichihara, Taguchi T Fau - Sakuramoto, I., Sakuramoto I Fau - Kawano, S., Kawano S Fau - Kawai, S., & Kawai, S. (2003). Mechanism of the spinal cord injury and the cervical spondylotic myelopathy: new approach based on the mechanical features of the spinal cord white and gray matter. (0022-3085 (Print)).

- Ichihara, Taguchi, T., Shimada, Y., Sakuramoto, I., Kawano, S., & Kawai, S. (2001). Gray Matter of the Bovine Cervical Spinal Cord is Mechanically More Rigid and Fragile than the White Matter. *Journal of Neurotrauma*, 18(3), 361-367. doi:10.1089/08977150151071053
- Jackson, A. B., Dijkers, M., DeVivo, M. J., & Poczatek, R. B. (2004). A demographic profile of new traumatic spinal cord injuries: Change and stability over 30 years. *Archives of Physical Medicine and Rehabilitation*, 85(11), 1740-1748. doi:<https://doi.org/10.1016/j.apmr.2004.04.035>
- Jannesar, Allen, M., Mills, S., Gibbons, A., Bresnahan, J. C., Salegio, E. A., & Sparrey, C. J. (2018). Compressive mechanical characterization of non-human primate spinal cord white matter. (1878-7568 (Electronic)).
- Jannesar, Nadler, B., & Sparrey, C. J. (2016). The Transverse Isotropy of Spinal Cord White Matter Under Dynamic Load. *Journal of Biomechanical Engineering*, 138(9). doi:10.1115/1.4034171
- Jessen, K. R., & Mirsky, R. (1980). Glial cells in the enteric nervous system contain glial fibrillary acidic protein. *Nature*, 286(5774), 736-737. doi:10.1038/286736a0
- Kaczmarek, M., Subramaniam, R. P., & Neff, S. R. (1997). The hydromechanics of hydrocephalus: Steady-state solutions for cylindrical geometry. *Bulletin of Mathematical Biology*, 59(2), 295-323. doi:[https://doi.org/10.1016/S0092-8240\(96\)00073-0](https://doi.org/10.1016/S0092-8240(96)00073-0)
- Karimi, A., Shojaei, A., & Tehrani, P. (2017). Mechanical properties of the human spinal cord under the compressive loading. (1873-6300 (Electronic)).
- Kohn, D. H. (1995). Acoustic emission and nondestructive evaluation of biomaterials and tissues. (0278-940X (Print)).
- Koser, D. E., Moeendarbary, E., Hanne, J., Kuerten, S., & Franze, K. (2015). CNS cell distribution and axon orientation determine local spinal cord mechanical properties. *Biophysical journal*, 108(9), 2137-2147. doi:10.1016/j.bpj.2015.03.039
- Kruse, S. A., Rose Gh Fau - Glaser, K. J., Glaser Kj Fau - Manduca, A., Manduca A Fau - Felmlee, J. P., Felmlee Jp Fau - Jack, C. R., Jr., Jack Cr Jr Fau - Ehman, R. L., & Ehman, R. L. (2008). Magnetic resonance elastography of the brain. (1053-8119 (Print)).
- Kwon, B. K., Hillyer, J., & Tetzlaff, W. (2009). Translational Research in Spinal Cord Injury: A Survey of Opinion from the SCI Community. *Journal of Neurotrauma*, 27(1), 21-33. doi:10.1089/neu.2009.1048

- Lai, W. M., Mow, V. C., & Roth, V. (1981). Effects of Nonlinear Strain-Dependent Permeability and Rate of Compression on the Stress Behavior of Articular Cartilage. *Journal of Biomechanical Engineering*, 103(2), 61-66. doi:10.1115/1.3138261
- Lam, C. J., Assinck, P., Liu, J., Tetzlaff, W., & Oxland, T. R. (2014). Impact Depth and the Interaction with Impact Speed Affect the Severity of Contusion Spinal Cord Injury in Rats. *Journal of Neurotrauma*, 31(24), 1985-1997. doi:10.1089/neu.2014.3392
- Lee, J. H. T., Jones, C. F., Okon, E. B., Anderson, L., Tigchelaar, S., Kooner, P., . . . Kwon, B. K. (2013). A Novel Porcine Model of Traumatic Thoracic Spinal Cord Injury. *Journal of Neurotrauma*, 30(3), 142-159. doi:10.1089/neu.2012.2386
- Li, X. F., & Dai, L. Y. (2009). Three-dimensional finite element model of the cervical spinal cord: preliminary results of injury mechanism analysis. (1528-1159 (Electronic)).
- Maikos, Qian, Metaxas, & Shreiber. (2008). Finite Element Analysis of Spinal Cord Injury in the Rat. *Journal of Neurotrauma*, 25, 795-816. doi:10.1089/neu.2007.0423
- Malandrino, A., & Moeendarbary, E. (2017). Poroelasticity of Living Tissues. In.
- Marchand, F., & Ahmed, A. M. (1990). Investigation of the laminate structure of lumbar disc annulus fibrosus. (0362-2436 (Print)).
- Mazuchowski, E., & Thibault, L. (2002). *BIOMECHANICAL PROPERTIES OF THE HUMAN SPINAL CORD AND PIA MATER*.
- McCracken, P. J., Manduca, A., Felmlee, J., & Ehman, R. L. (2005). Mechanical transient-based magnetic resonance elastography. *Magnetic Resonance in Medicine*, 53(3), 628-639. doi:<https://doi.org/10.1002/mrm.20388>
- Mercadante., & Tadi. (2020). Neuroanatomy, Gray Matter. Retrieved from <https://www.ncbi.nlm.nih.gov/books/NBK553239/>
- Mow, V. C., Kuei, S. C., Lai, W. M., & Armstrong, C. G. (1980). Biphasic Creep and Stress Relaxation of Articular Cartilage in Compression: Theory and Experiments. *Journal of Biomechanical Engineering*, 102(1), 73-84. doi:10.1115/1.3138202
- New, P. W., Farry, A., Baxter, D., & Noonan, V. K. (2013). Prevalence of non-traumatic spinal cord injury in Victoria, Australia. *Spinal Cord*, 51(2), 99-102. doi:10.1038/sc.2012.61
- Nishida, N., Kanchiku, T., Imajo, Y., Suzuki, H., Yoshida, Y., Kato, Y., . . . Taguchi, T. (2016). Stress analysis of the cervical spinal cord: Impact of the morphology of spinal cord segments on stress. *The journal of spinal cord medicine*, 39(3), 327-334. doi:10.1179/2045772315Y.0000000012

- Noonan, V. K., Fingas M Fau - Farry, A., Farry A Fau - Baxter, D., Baxter D Fau - Singh, A., Singh A Fau - Fehlings, M. G., Fehlings Mg Fau - Dvorak, M. F., & Dvorak, M. F. (2012). Incidence and prevalence of spinal cord injury in Canada: a national perspective. (1423-0208 (Electronic)).
- Norenberg, M. D., Smith J Fau - Marcillo, A., & Marcillo, A. (2004). The pathology of human spinal cord injury: defining the problems. (0897-7151 (Print)).
- Noyes, D. H. (1987). Correlation between parameters of spinal cord impact and resultant injury. (0014-4886 (Print)).
- Oakland, R. J., Hall Rm Fau - Wilcox, R. K., Wilcox Rk Fau - Barton, D. C., & Barton, D. C. (2006). The biomechanical response of spinal cord tissue to uniaxial loading. (0954-4119 (Print)).
- Ogden, R. W., & Hill, R. (1972). Large deformation isotropic elasticity – on the correlation of theory and experiment for incompressible rubberlike solids. *Proceedings of the Royal Society of London. A. Mathematical and Physical Sciences*, 326(1567), 565-584. doi:10.1098/rspa.1972.0026
- Ozawa, H., Matsumoto T Fau - Ohashi, T., Ohashi T Fau - Sato, M., Sato M Fau - Kokubun, S., & Kokubun, S. (2001). Comparison of spinal cord gray matter and white matter softness: measurement by pipette aspiration method. (0022-3085 (Print)).
- Pintar, F. A., Yoganandan, N., Sances, A., Reinartz, J., Harris, G., & Larson, S. J. (1989). Kinematic and Anatomical Analysis of the Human Cervical Spinal Column Under Axial Loading. *SAE Transactions*, 98, 1766-1789.
- Popovich, P. G., Fau., L. S., Gensel, J. C., Fau, G. J., Tovar, C. A., & Tovar, C. A. (2010). Independent evaluation of the effects of glibenclamide on reducing progressive hemorrhagic necrosis after cervical spinal cord injury. (1090-2430 (Electronic)).
- Ramo, N. L., Shetye, S. S., Streijger, F., Lee, J. H. T., Troyer, K. L., Kwon, B. K., . . . Puttlitz, C. M. (2018). Comparison of in vivo and ex vivo viscoelastic behavior of the spinal cord. (1878-7568 (Electronic)).
- Russell, C. M., Choo Am Fau - Tetzlaff, W., Tetzlaff W Fau - Chung, T.-E., Chung Te Fau - Oxland, T. R., & Oxland, T. R. (2012). Maximum principal strain correlates with spinal cord tissue damage in contusion and dislocation injuries in the rat cervical spine. (1557-9042 (Electronic)).
- Scifert, J., Totoribe K Fau - Goel, V., Goel V Fau - Huntzinger, J., & Huntzinger, J. (2002). Spinal cord mechanics during flexion and extension of the cervical spine: a finite element study. (1533-3159 (Print)).

- Sekhon, L. H., & Fehlings, M. G. (2001). Epidemiology, demographics, and pathophysiology of acute spinal cord injury. (0362-2436 (Print)).
- Sharkey. (2018). *An inverse finite element approach to modeling the rat cervical spinal cord : for use in determining the mechanical properties of the grey and white matter*. (Text), Retrieved from <https://open.library.ubc.ca/collections/24/items/1.0363918>
- Shetye, Troyer, K. L., Streijger, F., Lee, J. H., Kwon, B. K., Crompton, P. A., & Puttlitz, C. M. (2014a). Nonlinear viscoelastic characterization of the porcine spinal cord. (1878-7568 (Electronic)).
- Shetye, Troyer, K. L., Streijger, F., Lee, J. H. T., Kwon, B. K., Crompton, P. A., & Puttlitz, C. M. (2014b). Nonlinear viscoelastic characterization of the porcine spinal cord. *Acta Biomaterialia*, 10(2), 792-797.
- Sjovold, S. G., Mattucci, S. F. E., Choo, A. M., Liu, J., Dvorak, M. F., Kwon, B. K., . . . Oxland, T. R. (2013). Histological Effects of Residual Compression Sustained for 60 Minutes at Different Depths in a Novel Rat Spinal Cord Injury Contusion Model. *Journal of Neurotrauma*, 30(15), 1374-1384. doi:10.1089/neu.2013.2906
- Smith, L. J., Nerurkar, N. L., Choi, K.-S., Harfe, B. D., & Elliott, D. M. (2011). Degeneration and regeneration of the intervertebral disc: lessons from development. *Disease Models & Mechanisms*, 4(1), 31. doi:10.1242/dmm.006403
- Sparrey, Choo, A. M., Liu, J., Tetzlaff, W., & Oxland, T. R. (2008). The Distribution of Tissue Damage in the Spinal Cord Is Influenced by the Contusion Velocity. *Spine*, 33(22).
- Sparrey, & Keaveny, T. M. (2011). Compression behavior of porcine spinal cord white matter. (1873-2380 (Electronic)).
- Spinal Anatomy. (n.d.). Retrieved from <https://www.igeaneuro.com/spinal-anatomy/>
- The Spinal Cord. (n.d.). Retrieved from <https://courses.lumenlearning.com/boundless-ap/chapter/the-spinal-cord/>
- Spinal Cord. (n.d.). Retrieved from <https://healthjade.net/spinal-cord/>
- Spinal cord injury facts and figures at a glance. (2012). *The journal of spinal cord medicine*, 35(4), 197-198. doi:10.1179/1079026812Z.000000000063
- Spinal Meninges. (n.d.). Retrieved from <https://www.earthslab.com/anatomy/spinal-meninges/>
- Spine Anatomy. (n.d.). Retrieved from <https://www.goodmancampbell.com/conditions/spine/spine-anatomy/>

- Tator, C. H. (2006). Review of treatment trials in human spinal cord injury: issues, difficulties, and recommendations. (1524-4040 (Electronic)).
- Toen, C. Y. V. (2013). *Biomechanics of cervical spine and spinal cord injury under combined axial compression and lateral bending loading*. University of British Columbia,
- Vaccaro, A. R., Oner, C., Kepler, C. K., Dvorak, M., Schnake, K., Bellabarba, C., . . . Trauma Knowledge, F. (2013). AOSpine Thoracolumbar Spine Injury Classification System: Fracture Description, Neurological Status, and Key Modifiers. *Spine*, 38(23).
- Waxenbaum, Reddy, & Futterman. (2020, 2020 Aug 10). Anatomy, Back, Intervertebral Discs. Retrieved from <https://www.ncbi.nlm.nih.gov/books/NBK470583/>
- Yu. (2019). *Mechanical properties of spinal cord grey matter and white matter in confined compression*. (Text), Retrieved from <https://open.library.ubc.ca/collections/24/items/1.0387327>
- Yu, Manouchehri, N., Yamamoto, S., Kwon, B. K., & Oxland, T. R. (2020). Mechanical properties of spinal cord grey matter and white matter in confined compression. *Journal of the Mechanical Behavior of Biomedical Materials*, 112, 104044. doi:<https://doi.org/10.1016/j.jmbbm.2020.104044>